**TECHNISCHE UNIVERSITÄT CHEMNITZ**

# TiNbO$_x$ microscaffolds for studying early bone cell-material interactions in the microscale

Von der Fakultät für Naturwissenschaften der
Technischen Universität Chemnitz

genehmigte

## Dissertation

zur Erlangung des akademischen Grades
doctor rerum naturalium
(Dr. rer. nat.)

vorgelegt von

### Dipl. Biophysiker Raffael Herzer

geboren am 14.05.1988 in Kaiserslautern

## Bibliographic Information

# Abstract

Titanium alloys are frequently used in the medical field as bone implant materials due to their excellent biocompatibility and corrosion resistance. Yet, their elastic modulus is usually significantly higher than the one of bone, which can lead to a reduction of bone tissue at the implant site. The current research is therefore focused on the development of highly porous implants, which promise a low elastic modulus close to that of bone, an enhanced bone ingrowth and an improved vascularization. However, the appropriate pore size for an optimal osseointegration still remains unclear. To that end, a transparent tubular microsystem is developed to mimic such a porous microenvironment in order to study single bone cell behavior and early bone formation processes. The system is fabricated out of an implant material (β-stabilized Ti-45Nb (wt%)). It is demonstrated that the bulk material composition, which is consisting of a high Nb content, can be closely transferred to transparent thin films by using reactive sputtering. These films then self-assemble into tubular microscaffolds (TS) with a diameter range between 10-42 μm. Biological studies are subsequently performed to investigate the response (e.g. cell adhesion, migration, osteogenic differentiation) of human Mesenchymal Stem Cells (MSC) to the TS. It is shown that cells form fewer, more diffuse focal adhesion points inside the TS compared to a planar surface and the spatial confinement causes a switch in between amoeboid and mesenchymal migration modes. In addition, it is demonstrated that cells can survive inside the TS for at least 12 days during osteogenic differentiation and partly mineralize the TS interior. The observed mineralization process is furthermore linked to the formation of hydroxyapatite crystals inside dead cells bodies, which leads to a crystallization over time. All in all, the TS platform offers an easy way to identify key factors of bone cell-implant interactions that can be used to improve the biocompatibility of the bone-implant interface in the future.

Keywords: tubular microscaffold, strain-engineering, bone cells, mineralization, single cell analysis, implant material, material characterization, optical microscopy, osteogenic differentiation

The research of this thesis was conducted at the Institute for Integrative Nanosciences (IIN) at the Leibniz Institute for Solid State and Materials Research (IFW) Dresden in between 02/2017 and 02/2021. Part of the results depicted in this thesis have been published in the following peer-reviewed journal and reuse of figures is in accordance with the author rights granted in the Copyright Transfer Agreements (License Number: 5090201201398).

R. Herzer, A. Gebert, U. Hempel, F. Hebenstreit, S. Oswald, C. Damm, O. G. Schmidt, M. Medina-Sánchez: Rolled-Up Metal Oxide Microscaffolds to Study Early Bone Formation at Single Cell Resolution. *Small* **2021**, *17*, 2005527.

# Table of Contents

# 1 Introduction

Materials that are introduced into the human body as prostheses or medical devices undergo biochemical responses when implanted into living tissue.[1] In the worst case scenario, these responses include rejection reactions such as inflammation or fibrosis, which can result in repeated surgical operations.[1] In order to improve the materials' biocompatibility, scientists and engineers are tailoring different properties by changing the surface topography, chemical composition and/or by adding specific surface coatings.[2,3] Subsequently, the material host-response has to be studied by analyzing, for instance, the cell viability, the proliferation and the enzymatic activity in order to evaluate the effects of the aforementioned material modifications onto the implant integration.[4] In order to facilitate an analysis of these cell-material interactions in the microscale, this thesis aims at developing an *in vitro* platform that mimics the three-dimensional environment of single cells provided by modern porous metallic implants. In that respect, tubular microstructures can serve as a 3D microenvironment for studying living cells over long periods of time, which simplifies the observation of single cell-material interactions and the visualization of early bone formation. This introduction provides an overview over the challenges faced inside the bone implant field and presents various sophisticated new technologies that might help to improve our understanding of cell-implant processes towards personalized implant designs and functionality.

## 1.1 Implant materials

Grafting bone replacements has a long history in humankind. Already in ancient times surgery was conducted on humans suffering from trauma by using pure metals (iron, gold), natural materials (wood) and xenografts (animal bones) as replacement materials in order to treat the injury site.[5] With the beginning of the modern age between the 17th and 19th century, both advancements in the art of orthopedic surgery and a better understanding of bone structure and regeneration capabilities has led to more complex operation procedures.[5] Xenografts and autologous bone grafts, for instance, were used for the first time in skull surgeries, which allowed the complete regeneration of the bone defect by an improved bone-implant integration.[5] In the last decades, an increasing number of fabrication techniques and available implant materials provoked a switch towards highly biocompatible materials for structural implants,

which can be tuned to fit the particular body location and possess properties close to those of human bone.[6] While nowadays a large bone replacement market for biomaterials already exists, further technical innovations in the bone material biocompatibility are mandatory to counter the rising demand for sophisticated implants, which is caused by, for instance, the increasing number of elderly people in the world population and bone-related diseases.[7,8] Traditionally, metals are used as implant materials in order to replace or regenerate structural components on the human body due to their high mechanical strength and loading stiffness compared to ceramics or polymers.[9] Particularly, titanium and its alloys are frequently utilized materials in the field of trauma and orthopedic surgery, since they possess a comparable low Young's modulus, a superior biocompatibility and an excellent corrosion resistance.[10] However, the release of toxic metallic ions and/or particles through corrosion and wear processes can lead to safety problems and might reduce their long-term stability.[11] The high stiffness of metals compared to natural bone can also lead to a reduction of bone formation at the implant position, which can cause a loosening of the implant.[12,13] In order to improve current implants, several challenges have to be faced to enhance the material biocompatibility, osteoconductivity and osseointegration. Regarding the bulk implant properties, major objectives are the reduction of the elastic modulus and the fabrication of implants out of non-toxic materials. Furthermore, a modification of the implant surface is desired, as thereby an enhancement of the bone-implant integration can be induced. Apart from material optimizations, understanding biological elements such as the Extracellular Matrix (ECM), cytokines and growth factors is crucial, since these natural environmental cues influence the bone cells, which are responsible for the bone growth inside the body.[3] Designing and fabricating of complex *in vitro* systems for detailed cell analyses is consequently a highly important task, as these platforms facilitate the study of these essential factors and thereby help to improve the implant composition and structure. The following sections provide an overview over strategies, which are currently applied in order to tackle the above-mentioned challenges.

## 1.2 Porous implants and complex *in vitro* systems

One key challenge in bone implant development is the reduction of the disparity of the Young's modulus in between bulk implants and bone structures. Since structural implant are frequently fabricated out of metals such as stainless steel, Co-Cr-Mo and Ti alloys, these implants normally possess a Young's modulus in between 100-200 GPa, which is considerable higher than that of

natural bone (10-30 GPa).[14,15] Consequently, these bulk implants partially absorb the exterior stress and thereby reduce the physiologic loading of the bone, which can lead to a reduction of the bone formation.[12,13] In order to solve this issue, advanced implant engineering techniques were developed that permit the fabrication of porous bulk implants, which offer an elegant way to lower the implant elastic modulus.[16] By introducing pores, which can possess either small (below 50 µm) or large diameters (several 100 µm), void spaces are created inside the bulk scaffold.[16] Depending on the particular material composition of the bulk scaffold and the selected porosity, a strong reduction of the Young's modulus can be achieved.[16] For instance, recently developed porous TiNb scaffolds possess an elastic modulus close to that of cortical bone and improve the bone cell-implant interactions due to a high Nb content in their oxide layer.[17] Pores further improve the osseointegration and implant stabilization by bone tissue ingrowth, facilitation of body fluid transport and blood vessel formation, which is a necessity for lamellar bone development and provide cells with additional geometric cues.[18,19] However, while the positive effects of pores can't be denied, data gaps still exist regarding the exact effects of porous implant structures on bone cells and the optimal pore size.

In that regard, the interaction of bone cells with porous scaffold can be, for instance, analyzed by observing the tissue ingrowth after the insertion of an implant into the body. However, while reliable data is produced with clinical trial studies, human studies are time-consuming and are bound by strict regulations which limit available patient numbers.[20] In contrast to that, animal studies offer higher rates of experiments, yet don't reflect human body reactions perfectly, which leads to unreliable data that cannot be directly transferred to human physiology, and are ethical controversial.[21,22] Moreover, *in vivo* studies often require the extraction of the implanted material in order to estimate how changes in implant design, surface modifications as well as physical, chemical and biological treatments affect the cell response. An analysis of cell behavior in porous bulk implants is also limited by superimposed effects of pore size dimension, geometrical features and material properties, which all influence bone ingrowth and osteogenic differentiation in an *in vivo* application.[23] Consequently, new sophisticated *in vitro* systems are required that provide cells with realistic *in vivo* cues while facilitating the characterization of bone cell interactions with, for instance, curved surfaces, which exist inside the constricted environment of porous implants. Recently, highly complex 3D *in vitro* lab-on-a-chip systems were developed, which try to closely mimic complex 3D environment faced by implants in the human body.[24] They offer a convenient way to study bone cell behavior such as cell proliferation, adhesion and migration *in vitro* while providing cells with additional geometric cues.[24] These 3D platforms can be used to expose cells to natural occurring environmental

effects such as electric fields, pressure gradients, mechanical stress and biological cues as well as allowing a fast generation of reliable data for implant optimization by utilizing human cells in these studies.[24] Tubular microscaffolds (TS), for instance, are strain-engineered 3D microplatforms which were used to study the effects of confinement onto cell behavior (e.g. viability, morphology, migration).[25,26] It was demonstrated, that these TS can be used to live monitor cells and provide cells with geometrical cues that provoke a morphology change towards an *in vivo* cell shape, which is caused by a high level of confinement (a detailed description is provided in **Section 2.6.4**).[25,26] Thus, the utilization of 3D *in vitro* systems could lead to a profound comprehension of cell-implant surface interactions and bone cell regulation mechanisms, which is nowadays considered as a key factor for improving implant materials.

## 1.3 Objectives and structure of this thesis

As above-mentioned, the development and improvement of structural bone implants is a challenging task involving the selection of a suitable material composition, an adequate structural geometry and suitable surface modifications, which help to enhance the osseointegration of the respective implant. Deciphering how environmental factors such as spatial cues, the surface topography and the material composition influence the bone formation process is essential in order to acquire improved bone cell-implant interactions. Especially the investigation of bone tissue ingrowth into porous scaffolds is of high interest, since pores were shown to support bone formation processes.[16] The main aim of this thesis is therefore the development of a highly biocompatible transparent microplatform, which is fabricated out an implant material, mimics pores of bulk implants, provides cells with adequate chemical cues and facilitates the observation of single cell responses in a spatially restricted environment. To accomplish this objective, we explore the possibility to utilize strain-engineering in order to fabricate the required microstructures out of a suitable implant material (Ti-45Nb-oxide (wt%)) (**Figure 1.1**). A fabrication process is therefore established, which allows the formation of a high amount of tubular microscaffold arrays on each sample and a mass fabrication of these samples. These are mandatory conditions for performing a suitable number of cell experiments and biological analysis techniques (e.g. protein assays, DNA analysis) in order to decipher how material and topographical effects influence a cell layer during osteogenic differentiation. The microplatform is then used to acquire new insights about how a confined environment affects the behavior and properties (e.g. adhesion mechanism, migration, morphology) of single human
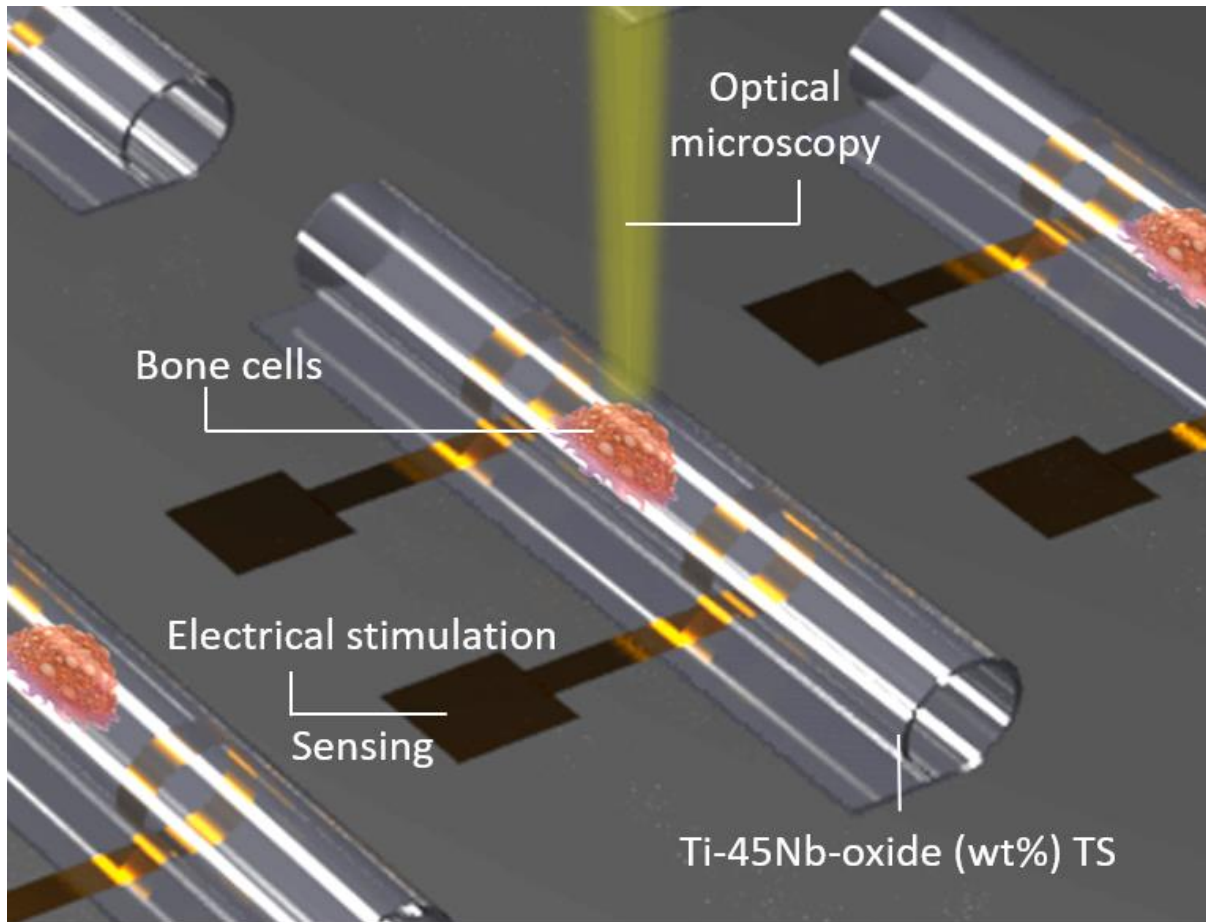
**Figure 1. 1:** Schematic of the Ti-45Nb (wt%) oxide tubular microscaffold (TS) platform for single bone cell observation and stimulation.

bone cells. Moreover, a long-term analysis is performed to unravel, if individual bone cells can induce a bone mineralization process inside the small micropores provided by the tubular microscaffolds during osteogenic differentiation. In order to acquire reliable data, the cell experiments are conducted with human Mesenchymal Stem Cells (MSC). All in all, the results from the here presented study serve to provide new insights about bone cells processes occurring in spatial restricted environments. They therefore contribute to improve the composition and geometrical design of structural implants for an enhanced osseointegration.

Based on the logical order of the above-mentioned objectives, the thesis outline is structured as follows:

The first part provides a state-of-the-art and an overview of the physiological function and structure of bone (**Section 2.1**), which is followed by a short summary of cells, cell properties and factors that are involved in the bone regeneration processes (**Section 2.2-3**). Subsequently, a basic introduction to structural implant materials (**Section 2.4**) and implant surface modifications (**Section 2.5**) is given. Afterwards, 3D microsystems are described, which are frequently used in the biomedical field in order to analyze and influence bone cells *in vitro*

(**Section 2.6**). In addition, the last part provides information about typical effects of confinement and curvature on cells (**Section 2.7**).

This is followed by the materials and method section (**Section 3**), in which firstly the tubular microscaffold fabrication parameters and surface characterization techniques are described, which are performed to characterize the deposited thin strain layers. Subsequently an overview over the biological analytical methods and tools is given, which are utilized to conduct bone cell experiments.

**Section 4** discusses the results of this thesis and is separated into 3 major parts: Microscaffold fabrication, material characterization and cell experiments. In the first part (**Section 4.1**), the deposition methods, devices and lithography steps are described, which are used to fabricate tubular microscaffolds (TS) out of the implant material as well as glass TS. Furthermore, two different fabrication approaches are presented, with which are utilized to deposited the required strain layer for the TS production. In addition, oxidation processes are introduced, which allow the formation of transparent TS. Afterwards, the material and surface characterization methods are described, which are performed on the deposited thin layers (**Section 4.2**). Subsequently, the outcome of the initial biological experiments conducted with human MSC and TS (**Section 4.3**) are described, which involve studies on the cell proliferation, adhesion and migration. This is followed by a detailed analysis of how the material and topography characteristics affects cells during osteogenic differentiation (**Section 4.4**) as well as an analysis of mineralization processes inside the TS (**Section 4.5**).

Furthermore, a discussion part is included in all of the particular sections, which compares the here presented results to recent findings from the literature. Finally, the highlights of this thesis are summarized and possible future applications are discussed (**Section 5**).

# 2 Fundamentals

As illustrated in the introduction, this doctoral thesis utilized an interdisciplinary approach combining the fields of implant material research, microscale scaffold fabrication and biological cell analysis to investigate the influence of environmental factors on bone stem cells. The following chapter provides an overview of these three major topics, in which the basic principles of each field and their intersection points are described. The first part of the fundamentals provides information about the bone structure, physiological bone functions, biomineralization and the interrelations between cell types involved in the bone remodeling process. This is followed by the second part giving an overview over common bone implant materials, the main challenges for enhancing bulk implants and surface treatment methods, which can be utilized to improve the bone-implant-interface. Finally, a state-of-the-art about recently developed *in vitro* platforms can be found in the last section, which allow cell monitoring while mimicking natural *in vivo* conditions. In addition, important topological factors such as confinement and curvature are described, which appear in *in vivo* conditions and strongly affect cell behavior.

## 2.1 Bone structure and functions

### 2.1.1 Physiological functions

Bone is a highly complex hierarchical system, which fulfills several important functions inside the human body. It is the main supporting structure of the body, protects important organs such as the brain and the heart and permits body movement by providing several attachment points for the muscle system.[27,28] The skeleton is involved in the blood cell genesis and acts as a large storage system for minerals such as calcium (99% of body calcium) and phosphorous (88%), which maintain the body homeostasis.[29–32] In addition, recent studies demonstrated that bone functions as an endocrine organ and can influence other organs as well as several body functions like the insulin formation by mediators such as e.g. osteocalcin that is released during bone resorption.[31,32]

## 2.1.2 Bone structure

Bone consists of a broad spectrum of interlinked nano- to macro-sized structures, which collectively form bone compartments that provide various mechanical and metabolic properties (**Figure 2.1**). The nano-sized basic units consist of a 3D framework of mineralized collagen fibers. These fibers possess diameters in the range of 100 nm, form 1-3 μm wide fiber bundles over time and provide channel-like gap regions, which function as attachment points for calcium phosphates from the environment.[33–36] These components are further organized into lamellae, which are micrometer-sized structures in the range of 2-9 μm consisting of ordered patterns of mineralized collagen fibers, disordered mineralized matrix components with abundant non-collagenous organic material and unorganized single collagen fibrils.[35] Subsequently, osteons, a frequent cylindrical shaped bone unit in the range of 200-250 μm diameter, are formed by 3-8 concentric layers of lamellae around a central Haversian channel (30-40 μm diameter), which contains nerve fibers and blood vessels for nutrition supply.[34,37] These super-structures are interstratified with small cavities, so-called lacunae, housing a network of interlinked osteocytes, which can sense the mechanical stress in their environment and thereby regulate the bone formation.[38,39] Finally, the macro-sized bone structures can be divided into cortical bone (a highly dense structure), trabecular bone (a network of porous structures) and the bone marrow cavity, in which the blood stem cells reside and differentiate.[29,40]
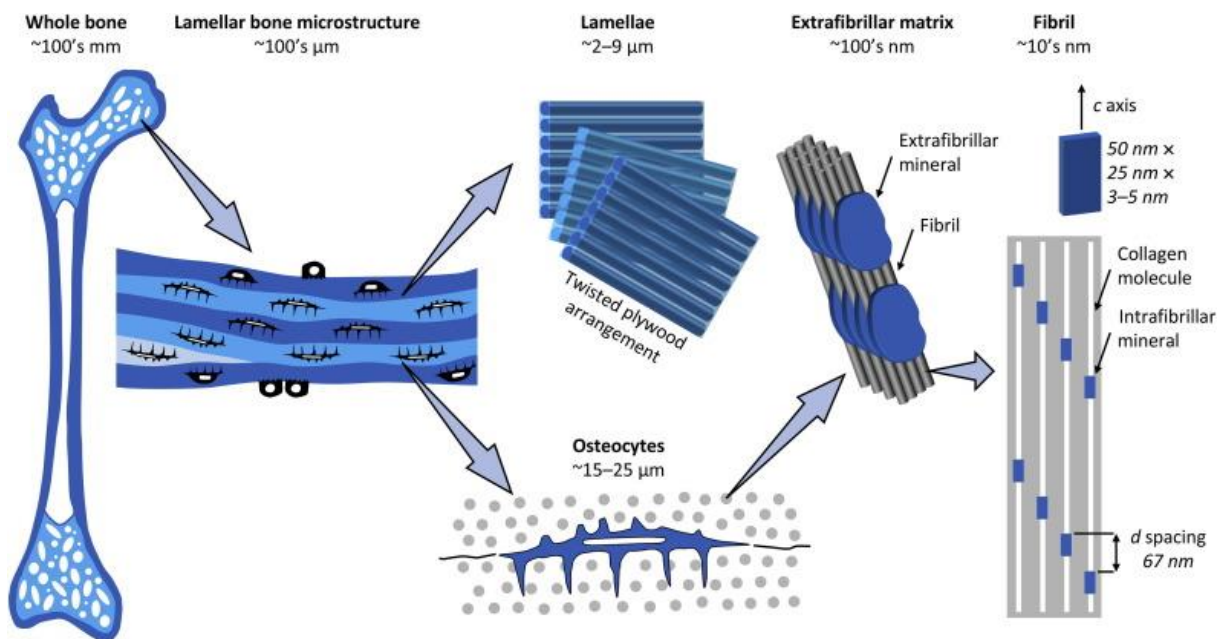


**Figure 2. 1**: Bone structure from the macro-scale down to the nano-scale (left to right). Figure from reference.[33]

## 2.2 Bone cell interactions and bone remodeling

### 2.2.1 Mesenchymal stem cell characteristics and applications

The formation of bone structures is conducted by osteoblasts, which differentiate from Mesenchymal Stem Cells (MSC).[41] MSC are a heterogeneous group of multipotent cells, which were originally found in the bone marrow. Nowadays, they can be isolated from several tissues like skeletal muscle, adipose tissue, pancreas and are a prominent candidate for cell-based therapies in the medical field.[42,43] While their *in vitro* morphology is commonly described as fibroblast-like with spindle-shaped cell bodies, other subtypes were also encountered depicting a larger, flat or a smaller, round phenotype.[44] Thus, a broad spectrum of cell sizes from few µm to more than 40 µm was encountered, which leads to average cells diameters in between 12.6 µm to 30.4 µm.[45,46] These differences in morphology and cell size might be related to age dependent effects, as larger cells were encountered in higher passage numbers *in vitro*.[47,48]
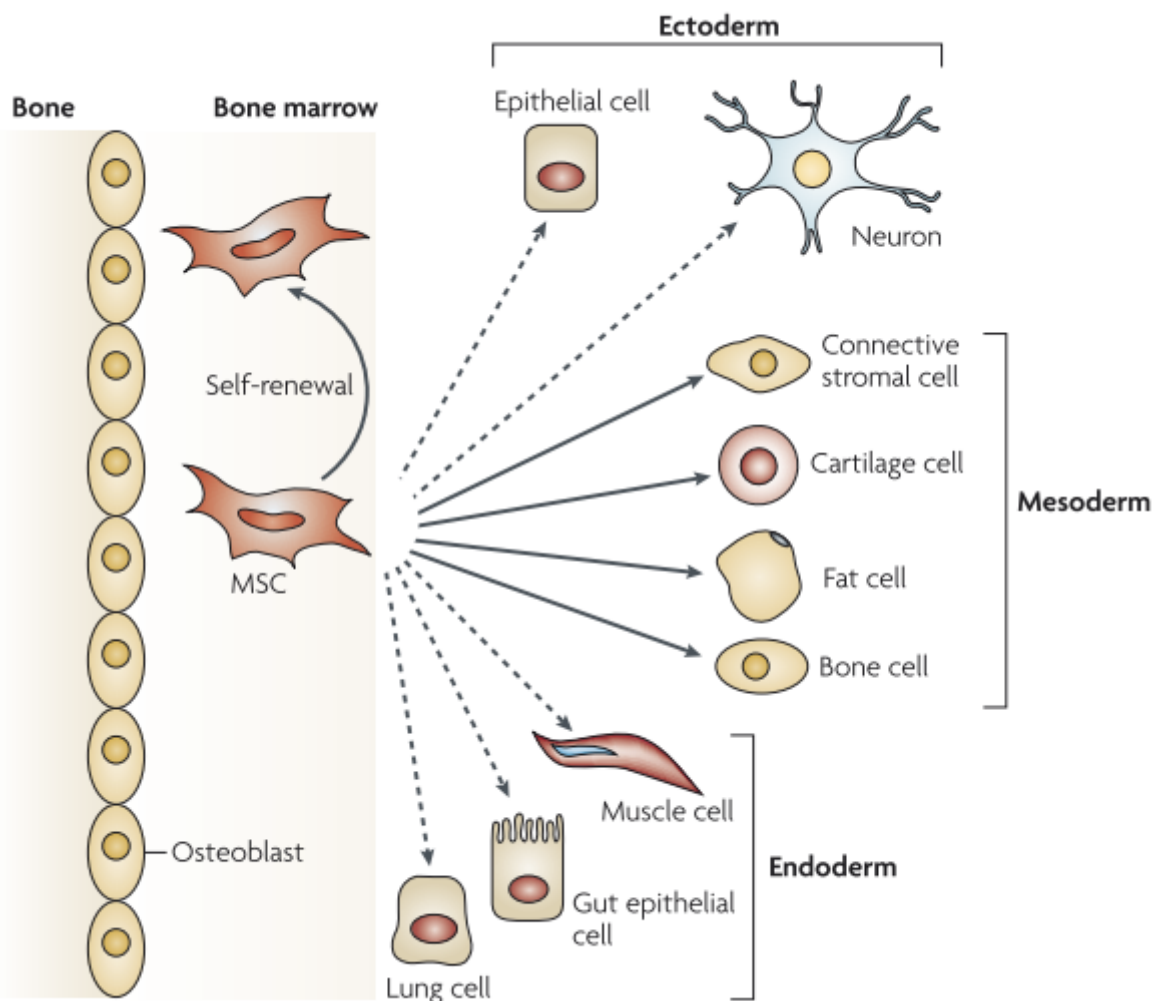


**Figure 2. 2:** Differentiation potential of MSC cells. Taken from reference.[49]

Moreover, MSC are pluripotent cells and can differentiate into various cell types (**Figure 2.2**). They are commonly characterized by inducing a differentiation into osteoblasts, adipocytes and chondrocytes as well as by verifying their cell adherence to plastic.[50,51] Recent studies demonstrated that additional linage commitment can be acquired as MSC were observed to differentiate into muscle cells, neurons and epithelial cells.[49,52] Hence, MSC are used to treat various medical conditions like cardiovascular diseases, spinal cord injuries and bone diseases. In addition, they play an important role in the bone remodeling process.[53]

## 2.2.2 Bone injuries, remodeling and biomineralization

Bone formation and maintenance is a constant, complex process modulated by several different cell types that partly originate from MSC (e.g. chondrocytes, osteoblasts). The two major bone formation processes are endochondral ossification, in which chondrocytes form cartilage, that is subsequently replaced by bone and intermembranous ossification, in which bone is directly formed by osteoblasts.[54,55] The bone remodeling process is conducted by bone forming cells (osteoblasts) and bone degrading cells (osteoclasts), which are both influenced by a network of osteocytes (terminal differentiated form of osteoblasts).[56]

After a fracture occurred or a surgical procedure was conducted, the remodeling process is initiated in the damaged region. Subsequently, the body immune reaction leads to an acute inflammation state in the first step of fracture healing, which triggers MSC migration towards the injury site due to chemotaxis signaling.[57,58] In parallel, osteocyte cell death in the affected area leads to a recruitment of pre-osteoclasts, which bind to the bone matrix and differentiate into mature osteoclasts.[53] These two cell types form together the basic multicellular unit, in which the resorption of damaged bone and the formation of new bone takes place.[56,59] In a next step, mature osteoclasts start to form sealed area underneath them and subsequently secrete hydrogen ions and acid phosphatases into the resorbing compartment, which decreases the local pH value down to 4.5 leading to the disintegration of inorganic bone material. The organic components of the bone matrix are then digested by several enzymes (e.g. gelatinase, metalloproteinase 9), which ultimately leads to the formation of pits (Howship's lacunae) on the surface.[27,56,60] In a second step, MSC cells arrive to the injury location, differentiate into osteoblasts and start to form the ECM, which acts as a scaffold for the biomineralization process. Groups of osteoblasts subsequently secrete a mixture of organic components that forms the osteoid, which mainly consists of dense layers of crosslinked collagen type I as well as

lower amounts of osteocalcin and osteopontin (OPN).[61] Moreover, Matrix Vesicles (MV) are released from osteoblasts into the surrounding environment, which generate and transport $P_i$ in their lumen. These MV bind $Ca^{2+}$ by specialized protein families (e.g. Anx A1) until a critical mass of $Ca^{2+}/P_i$ is reached in the MV lumen and initial CaP-crystals are formed.[62] Initial apatite crystals subsequently bind to the gap regions in between collagen fibers, increase in size by accumulating Ca/P ions from the surrounding media, which ultimately leads to a mineralization of the protein matrix.[62,63] Moreover, osteoblasts can either promote the osteoclast formation by the expression of the regulator molecule RANKL (receptor activator of nuclear factor kappa-B ligand), or inhibit it by utilizing the decoy receptor osteoprotegerin (OPG), which blocks the interaction between RANKL and the surface receptor of osteoclasts RANK (receptor activator of nuclear factor kappa-B).[64] Recent studies also demonstrated that osteocytes, which reside in lacunae inside the bone, can influence osteoclasts by secreting RANKL.[65]

## 2.3 MSC migration and adhesion

Cell adhesion and guided cell migration are important mechanisms closely linked to the bone remodeling process. In case of an injury, MSC cells start to move towards the damaged region mediated by the so-called homing mechanism, which includes a directed cell movement due to chemical gradients (e.g. growth factors, cytokines).[66,67] In order to reach the injury site, cells are transported inside blood vessels until they are close to the desired location.[68] At that point, cell attachment to the vascular walls is induced by the interaction between endothelial surface structures (e.g. chemokine receptors) and cell body surface elements (e.g. integrins). Subsequently, cells form protrusions (e.g. lamellipodia, filopodia, pseudopodia) and start to migrate along the vessel walls until specific locations are reached, where MSC can cross the endothelial border.[69] The MSC transendothelial migration is initiated by finger-like protrusion and blebs, which bind to cells of the endothelial border.[70,71] Consequently, the inter-endothelial cell-cell connections (e.g. gap and tight junctions) are disrupted, which leads to the formation of a narrow channel in the endothelial border.[70,71] Therefore, enough space is available for a paracellular migration.[70,71]

## 2.3.1 Adhesion

The cell adhesion process is tightly connected to ECM components (for detailed information see **Section 2.5.2**) as well as substrate properties such as physical cues and the surface chemistry. The ECM rigidity, for instance, can alter the cell cytoskeleton organization and therefore influence cell migration, growth and differentiation.[72] The link between the intracellular F-actin skeleton and surface elements is established by multiprotein adhesion complexes, which include transmembrane receptors such as integrins, actin filaments and anchoring proteins like talin or vinculin, which strengthen the actin-integrin binding.[72–74] These actin-integrin binding sites allow cells to sense environmental factors such as extracellular matrix components, mechanical forces, substrate topography and surface rigidity, among others.[72] They can be furthermore divided into focal complexes (100 nm diameter, <1 μm length), Focal Adhesions (FA, 1-5 μm length) and supermature focal adhesions (>5 μm length), which differ in their binding strength, thickness and magnitude.[73,75,76] Small adhesion complexes are frequently associated with rapidly formed temporary structures, which allow cell locomotion and therefore quickly dissolve again. Yet, they can also grow into mature FA, which influence cell differentiation processes.[75,77] In case of bone cells, large FA occur on stiff materials, are located at the end points of actin stress fibers and are associated with an osteogenic differentiation.[74,78,79] Furthermore, the formation of large FA can be triggered by modifying the surface of, for instance, Ti with nanostructures (pillars, dots), which results in an osteogenic linage commitment of MSC.[80,81]

## 2.3.2 Migration

Similar to adhesion processes, cellular migration is strongly correlated to the respective environment and depends on cell-cell as well as cell-matrix interactions. While the first cell migration studies were conducted on 2D surfaces, which are frequently used in *in vitro* conditions, the majority of cells move inside a 3D confined space in an *in vivo* environment, which strongly influences their migration mode and morphology.[82] The basic mechanism for cell movement can be described as a repetitive three-step process. Firstly, cell protrusions (e.g. lamellipodia) are formed at a leading front edge of the cell. This process is mediated by actin-polymerization, which extends the plasma membrane towards their polymerization direction.[72,83,84] Secondly, an integrin-based cell attachment to the substrate surface occurs in

positions where cell protrusions persist.[85] Actomyosin contractions lead subsequently to a translocation of the cell rear body part to a specific adhesion site, which is accompanied by a detachment of focal adhesions at the cell rear end. These cell projections initially start to form in random directions from the cell main cell body mass and are used to explore the substrate environment, which is sensed with various intermembranous receptors.[83,86] A subsequent switch to a more directional migration is provoked by several environmental properties (e.g. substrate topography, electric fields, gradients like fibronectin density (chemotaxis)), which lead to a reinforcement of the cellular projections in direction of these surface elements by cell internal positive feedback loops.[81,85,87] Furthermore, the cellular movement can be divided into mesenchymal migration, which involves a high cytoskeletal contractility as well as a strong cell-substrate attachment due to FA, and amoeboid migration, in which cells depict a rounded morphology without large stress fibers and mature focal adhesion complexes.[86] However, the respective migration mode isn't strictly restricted to the cell type, which allows individual cells to switch between both modes while adapting to external cues and therefore assuming an optimal migration behavior.[84,86,88,89] A detailed report of how 3D environmental cues influence the cell migration and adhesion behavior can be found in **Section 2.7**.

## 2.4 Structural implants: Materials and fabrication methods

Structural implants are used to stabilize a fracture side and to promote the bone growth by improving the cell-surface interactions (e.g. cell adhesion, proliferation).[90] In order to function properly, the structural implant material has to match the specific requirements depending on its function and has to possess properties such as a high strength, loading stiffness and wear resistance.[6] Metallic bone implants can be produced with traditional fabrication techniques such as casting, forging and machining as well as with modern, more sophisticated methods of additive manufacturing like selective laser melting and direct metal laser sintering, which allow the fabrication of customized implants that can be adapted to the individual patients requirements.[91–93] Furthermore, various different materials like metallic alloys, composites, bioactive glass, ceramics and polymers can be used to treat bone defects.[94–98] Since in this doctoral thesis metallic implant material were analyzed, this short review will focus on metallic implants and their alloys.

## 2.4.1 Metal implant types

As a lot of metals exhibit a good biocompatibility, high strength and a high corrosion resistance, numerous metallic materials such as pure Ti, Ti-alloys, stainless steel and Co-Cr based alloys are frequently utilized in the medical field.[2,6] However, each material type possesses certain assets and drawbacks and is therefore favored in certain conditions. Stainless steel, for instance, is a low-cost material, which is frequently used as in the medical field.[99] Yet, it possesses a comparable poor corrosion resistance, wear resistance and can cause allergic reaction due to Ni ion release in long term applications.[99,100] As a consequence, steel is nowadays often applied in temporary restricted processes such as fracture fixation (e.g. steel screws, nails).[101]

In contrast to that, Co alloys possess a higher wear resistance, ductility and corrosion resistance than stainless steel as well as depict an excellent resistance in loading conditions.[102] Co is frequently alloyed with molybdenum and chromium, which increase its corrosion resistance (Co-Cr-Mo). These alloys are subsequently used as long-term implants for hip defects.[2,102,103] However, the fabrication of Co-alloys is rather expensive, which limits their wide-ranged usage in contrast to steel-based implants.[101] Another drawback can be found in toxic elements used in Co alloys (e.g. Cr, Ni), which can lead to inflammation and allergic reactions at the implant site.[102]

Another type of implant material is pure Ti and its alloys, which are frequently used in the medical field. β-type Ti alloys, for instance, possess a low Young's modulus close to that of natural bone, a comparable low density (~50% of cobalt, stainless steel) and a high biocompatibility.[10,104] Moreover, a natural $TiO_2$ passivation layer forms rapidly on the surfaces of Ti-alloys, which results in a high corrosion resistance.[105] Thus, the α/β-phase alloy Ti-6Al-4V is one of the most common bone implants materials and is frequently used for hip joints, knee joints and artificial hearts.[106–108] However, recent studies indicate to a cell toxic effect caused by V as well as the occurrence of neurodegenerative diseases (e.g. Alzheimer) related to particle release of V and Al atoms.[109,110] Current research concentrates therefore on the fabrication of new types of Ti alloys in which V and Al are replaced by other elements such as Zr, Ta, Mo or Nb.[108,111,112]

Although metals are frequently used in the medical field, there are many issues that can be improved for future implant applications, such as a reduction of wear particle formation, fatigue corrosion and long-term release of putative toxic ions.

## 2.4.2 Stress shielding and modern implants

New classes of metallic implant materials and alloys with reduced number of toxic elements in their composition as well as with improved mechanical properties, i.e. decreased Young's modulus values, are currently investigated. The elastic modulus, for instance, should be close to that of bone in order to have improved stiffness values. Unfortunately, a huge gap still exists between the Youngs modulus of clinical used materials like stainless steel, Co-Cr-Mo (200 GPa), commercial Ti alloys (100 GPa) and natural bone structures (e.g. cortical bone 10-30 GPa).[14,15] Subsequently, the exterior stress is partially absorbed by these materials, which is known as the so-called "stress shielding effect".[113] As a consequence, the bone formation is reduced at the defect site due to a reduced mechanical stimulation (Wolff's law), which can lead to an implant loosening in the direct aftermath of a surgery or osteoporosis in a long-term scenario.[12,114] A reduction of stress-shielding effects therefore allows a better transfer of mechanical load to the injured bone, which improves bone regeneration processes.[113] Besides developing β-stabilized Ti alloys with specific compositions and microstructural states, another strategy for the reduction of the Young's modulus values is the integration of pores into bulk implants. Those "metallic scaffolds" can exhibit very low Young's modulus values of $\leq 10$ GPa, i.e. comparable to that of spongy bone and the porous design can enable a very good mechanical anchoring/ingrowth of bone tissue. The design of those porous implants based on β-type alloys with low constituent toxicity is considered as an important goal of current research.[115,116]

## 2.4.2.1 β-stabilized Ti-alloys and porous scaffolds

β-stabilized Ti-alloys were originally developed for the aircraft industry and are nowadays used for orthopedic applications.[117,118] Numerous metal elements such as V, Ni, Mo and Nb can function as β-phase stabilizers and lead to a dramatic decrease of the stiffness.[111] Thus, a low Young's modulus down to 40 GPa (e.g. Ti-Nb-Sn) can be achieved, which is a significant improvement compared to standard Ti alloys (80-100 GaP) used in the medical field.[119] For example, for TiNb alloys which were quenched from the β-phase region, it was demonstrated that a high content of Nb (40-45wt.%) alone is sufficient to stabilize a single β-phase with Youngs modulus values of about 60GPa. Additional thermomechanical treatments of those alloy samples can lead to a significant increase of the ultimate compressive and tensile strength

while maintaining the elastic value.[120] This alloy type offers additional benefits as both elements, Nb and Ti depicted a low toxicity and a good biocompatibility.[119]

A further reduction of the elastic modulus can be achieved by the fabrication of porous scaffolds, which offer certain benefits compared to standard bulk implants. For instance, the pore integration allows a bone tissue ingrowth, which improves the implant stabilization inside the body by an enhanced osseointegration.[23] Moreover, pores provide ample space for vascularization ingrowth and facilitate the transport of oxygen and nutrients into the implant.[121,122] Yet, the selection of an appropriate pore size remains a major challenge, as the pore size influences the mechanical stability of the implants and determines the amount of new formed bone tissue inside the scaffold. Porous TiNb scaffold, for instance, can be fabricated with selective laser melting (SLM) and space-holder sintering.[17,123] These scaffolds possess macropores in the range of several hundred micrometers (e.g. 100 -300 µm) and micropores in the range between 1-3 µm.[123] Due to the pore integration, a very low elastic modulus below 10 GPa (e.g. β-type Ti-40Nb), can be obtained and these structures depict a porous network similar to that of trabecular bone.[17,18] Furthermore, while pore sizes in between 100-600 µm are mainly considered to be optimal for bone ingrowth, vascularization, a crucial factor for successful bone remodeling, was observed in pore sizes around 50 µm.[19,23,124,125] Recent studies also demonstrated an initial bone ingrowth in pore sizes smaller than 10 µm and even down to 1 µm.[126,127] Thus, while various pore sizes can improve the bone remodeling process at a defect site, further studies are required to gain a better understanding of a potential bone ingrowth in small micropores.

## 2.5 Implant surface treatments and modifications

Apart from the implant geometry, surface modification and functionalization processes play an important role in the implant development as they improve the body response after a surgery and thereby increase the implant osseointegration.[3] Implants are in direct contact with the biological environment inside the body and constantly interact with its liquid and solid components such as blood, interstitial fluid, tissues and, in particular, different cell types.[33,99,128] Furthermore, the resulting implant-body interactions are dependent on various factors such as the surface chemistry, surface topography (e.g. micropatterns, nano structures) and the surface energy, among others.[128] Thus, biological and non-biological surface modification can be

applied to provide bone cells with natural-like cues in order to enhance the bone formation. Furthermore, recent studies seek to combine these modification types in order to mimic the ECM, which resembles the natural 3D bone cell environment.[129] Hence, the following sections will provide an overview over commonly utilized surface modifications on metal alloys.

## 2.5.1 Non-biological modifications

Non-biological modification processes can be divided into mechanical roughening (e.g. grinding, polishing), physical treatments (e.g. ion implantation or plasma spraying for example of Ca-phosphate compounds) and chemical surface treatments (e.g. etching, anodization-oxidation), which are mostly applied to improve cell responses like an increased cell adhesion, a higher proliferation rate, an enhanced osteogenic cell differentiation and finally, to achieve an optimal osseointegration.[130]

The natural surface state of Ti or a Ti alloy surface is covered with a very thin oxide film – mainly $TiO_2$ - which spontaneously forms under ambient conditions.[131] However, in this state the surface is considered to be "bioinert"."[131] In order to make the surface more "bioactive", mechanical and chemical treatments have to be applied. These treatments aim to increase the surface roughness and to thicken the oxide film, which is known to stimulate bone cell activity and induce tissue growth. It is also desirable to modify the surface in order to obtain antibacterial properties to avoid biofilm formation..[132–134] Meanwhile, there is a variety of oxidation treatments available, with which oxide coatings with macro- to nano-scale thickness and porosities can be produced.[133,135] Furthermore, it has been demonstrated for beta-type Ti alloys that other beta-stabilizers like Nb contribute to the oxide layer formation as they can be incorporated in the oxide film composition forming TiNb-mixed oxides.[136]

Altogether, it is important to emphasize, that a cell is always in contact with a more or less pronounced surface oxide mostly directly grown from the metal/alloy substrate, but is not in direct contact with the bare metal phase.

In the case of Ti-alloys, chemical surface etching with strong acids such as HCL, a mixture of $H_2SO_4$ and HCl or piranha solution (mixture of $H_2SO_4$ and $H_2O_2$) can be utilized to improve the surface properties.[137–140] The immersion of the implant material in acid solutions results in a surface roughness increase, which is caused by the formation of homogeneous nano- or micro-elements in the implant surface.[137,141] The size of these structures can be controlled by the

process temperature, the acid exposure time, the applied acid and its concentration.[142,143] In the case of TiNb alloys, chemical etching with piranha solution leads to a formation of semi-spherical nano-pit (25 nm mean diameter) and an increase of the oxide layer thickness, which is enriched with $Nb_2O_5$.[144] An improved bone cell adhesion, spreading and an upregulated Tissue Nonspecific Alkaline Phosphatase (TNAP) activity was subsequently observed compared to pure Ti, which might be caused by a change of the surface energy state due to the $Nb_2O_5$ fraction.[144]

Anodization is another method frequently used to treat Ti-alloys.[145] The surface modification is based on an electrochemical process which is conducted in a suitable electrolyte and in which the implant metal is employed as oxidizing anode.[118] Since Ti and its alloying elements are mainly so-called "valve-metals", the growth of the oxide layer occurs on basis of high-field growth mechanism and leads to potential-controlled thickening of barrier-type oxide layers.[146] By variation of the process conditions, those anodization treatments can cause not only an increase of the oxide layer thickness but can furthermore alter the surface layer morphology and create a porosity ranging from micro- to nano-scale structures.[147] Various factors such as applied voltage, anodization time, temperature and electrolyte concentration influence the geometry and size of these surface structures (e.g. pores) inside the oxide film.[147,148] Furthermore, titanium oxide nano-tubes in the range of 10 nm to >100 nm diameter can be produced by anodization in fluoride-containing electrolytes, which influence the surface wettability by increasing the surface energy.[149]

In case of β-type Ti-40Nb (wt%) alloys, the Nb constituent was found to strongly influence the formation of those surface oxide structures. This ranges from the growth of highly ordered oxide nanotubes where Nb controls the tube lengths and diameter, to the Nb-controlled formation of micropores and microchannels in oxide coatings grown by a plasma-electrolytic process.[136] In all cases, mixed (Ti, Nb)-oxides were detected whereby the Ti:Nb ratio was nearly transferred from the metal substrate to the oxide phases.[136]

### 2.5.2 Biological functionalization

The above-mentioned methods can be combined with biological functionalization, which utilize, for instance, coatings made of proteins and inorganic components of the ECM in order to improve the bone tissue growth around the implant.[3] The bone ECM is a 3D structure which

regulates the cell behavior and consists of a dense protein meshwork secreted by bone cells as well as inorganic substances such as hydroxyapatite (HA).[150] While it primarily contains collagens (90% of the protein mass), which provide resilience and strength, numerous other non-collagenous proteins (10% of the protein mass) such as glycoproteins, glycosaminoglycans (GAG), fibronectin and several ,osteoproteins' like osteocalcin, osteonectin, osteoadherin, OPN etc. can also be found inside the ECM.[30,151] Other components like growth factors e.g. Transforming Growth Factor β and Bone Morphogenetic Protein (BMP), which influence ECM formation and cell differentiation, are also incorporated in the ECM.[30,151] Subsequently, coatings made of HA, collagen typ I, the RGD (Arg-Gly-Asp) peptide sequence provide integrin attachment sites as well as chondroitin sulfate is deposited on Ti-alloy surfaces to improve their bioactivity.[152–155] One of the most frequently used modifications are artificial HA coatings, which possess similar characteristics as natural formed HA and can be further substituted with Zn, Cu, Mg, Ag in order to add new properties such as an antibiotic activity.[156] Using these HA coatings can cause an increased osteoid formation, bone adhesion, bone formation and implant fixation.[156,157] Further improvements of the Ti alloy osseointegration in terms of an enhanced cell recruitment, adhesion, proliferation and differentiation can be achieved with collagen and GAGs coatings, which facilitate the formation of focal adhesion sites.[158,159] In the case of Ti-40Nb alloys, the adhesion of hMSC was augmented by depositing gold nanoparticles functionalized with cyclic RGD peptides on the material surface, which led to an increased number of focal adhesion points.[160] In summary, surface modifications play an important role in improving the bio response of metal implants, which subsequently can positively affect the osseointegration.

## 2.6 *In vitro* systems for cell analysis

This section provides an overview over microsystems, which are currently used to stimulate and analyze cell responses. Hydrogels, microfluidic devices and metallic scaffolds are frequently used to study cell behavior while providing cells with an artificial 3D *in vitro* environment in order to closely mimic the *in vivo* cell conditions.[161–164] Moreover, new technologies like tubular scaffold platforms are described. These are based on strain-engineered nanofilms and offer the possibility to capture, stimulate and analyze individual cells in a confined 3D environment by using high resolution optical microscopy.[25] In contrast to traditional 2D experiments, complex 3D environments can be tuned to the specific need of a

specific cell type by adjusting the scaffold geometry and by integrating, for instance, signal molecules, which strongly influence the cell reactions.[161] As a consequence, more reliable data can be obtained about how environmental factors (e.g. topography, fluidic stress, electric fields), which are present inside the human body, influence cell responses.[165–167] Furthermore, microplatforms can be fabricated with diameters close to the cell size and consequently facilitate the *in vitro* study of cell-material interactions, which are otherwise challenging to monitor in experiments using bulk scaffolds materials.[25] Due to that, the properties and characteristics of individual cells can be distinguished and analyzed, which is mandatory to develop patient specific therapies for, for instance, cancer treatment.[168] This section describes how 3D cues (e.g. surface patterning, porous structures) and spatial confinement affect cell behavior such as the cell migration, the morphology and the cell osteogenic differentiation.

## 2.6.1 Micropipettes

The monitoring and characterization of single cells becomes increasingly important in current biological research as recent studies depict a high heterogeneity even within the cell population of the same cell type.[169,170] These individual cells possess different properties such as diverse levels of protein expression or spatial heterogeneities compared to adjacent cells and therefore potentially influence the behavior of a whole bulk cell population.[171] Consequently, highly sophisticated analytic tools are needed to study the characteristics and subcellular processes of single cells.

In this regard, micropipettes are one type of modifiable microsystems, which can be used to analyze numerous cell properties such as the membrane elasticity, ion channel activity, the electrophysical state and the cell internal metabolic activity, among others.[25] They consist of an outer conical shell and an internal channel, which permits the exchange of liquids and cellular components.[25] Micropipettes can be furthermore fabricated out of various materials such as glass substrates and carbon-based materials as well as with a large range of different tip sizes.[25,172] While large microtips (micrometer-sized pore diameter) can be used to transfer and analyze whole cells, single cells can be penetrated by tips with smaller dimeters (in the nano range) without causing permanent damage to the respective cell.[173,174] This procedure allows, for instance, an insertion of materials (e.g. drug carriers, nanoparticles) into the cell as well as the extraction of cell components (e.g. organelles, mRNA).[175–178] micropipette tips can be modified with optical fibers and conductive materials, which transform the tips into sensor

devices.[179,180] For example, coating the pipette surface with gold nanoparticles allows high surface enhanced Raman spectroscopic measurements, which can be used to detect intracellular pH values and neurotransmitter contents (e.g. dopamine).[179,181] Microelectrode pipettes on the other hand allow the detection of electrophysical properties inside the cell body, which can be used, for instance, to measure the oxygen consumption of cells and therefore their metabolic activity.[182] Patch-clamp is a frequently used method based on the application of microtips, which is utilized to conduct electrophysiological characterizations on individual cells.[183,184] It is performed by gently pressing a micropipette filled with electrolyte solution onto a membrane patch of an isolated cell.[183,184] Subsequently, a light suction is applied, which leads to the formation of a so-called gigaseal.[183,184] This tight connection enables measurements, for instance, of ionic currents which are generated by an ion flux through transmembrane channels of the respective cell.[183,184]

The patch-clamp method can be therefore used to determine electrophysical characteristics of bone cells and observe effects of specific ion channel activities on their differentiation behavior. In this regard, research is strongly focused on $Ca^{2+}$-ion channels, as they are suspected, for instance, to influence the linage commitment of MSC and the fluid shear stress response of osteoblast.[185,186] Barradas et al. studied the connection in between the activation of voltage-gated calcium channels and the osteogenic differentiation of human bone MSC by measuring the expression level of bone morphogenetic protein 2, which is a protein associated with the osteoblast formation and fracture healing.[187] They showed that the while an inhibition of the calcium channels by nifedipine lead to a decrease of the bone morphogenetic protein expression, active channel increased the gene expression.[187] A similar study reported that the inhibition of calcium channel caused a suppression of rat MSC proliferation.[188] Yet, the exact effect of ion channels on bone cell osteogenesis remains unclear, as contradictory data was obtained from different species. While the inhibition of calcium channel suppressed osteogenesis in rat MSC, the osteogenic commitment was induced by the calcium channel blocker benidipine in a study with mouse MSC.[188,189] Furthermore, pulsed electromagnetic field exposure applied to human MSC was reported to support the osteogenic differentiation towards osteoblasts, as electromagnetic field can trigger $Ca^{2+}$ related mechanisms involved in the osteogenesis.[190,191]

Micropipettes are powerful tools that permit a detailed analysis of various different properties of single cells. Yet, this technique is often limited to static conditions, in which the cell has to stay in a same location for the duration of the measurement. Since nowadays, studies focus on

determining effects of environment factors on cell behavior in dynamic settings (e.g. external fluid flow) and providing cells with realistic surroundings (e.g. 3D structures), the usage of microprobe can be restricted in these conditions, especially with confined analysis platforms.[192–194]

## 2.6.2 Surface patterning, hydrogels and 3D scaffolds

Surface patternings allow the study of spatial effects onto a whole cell population as well as the analysis of single cells at the same time. Patternings can be applied to implant surfaces and provide cells with additional geometric cues, which are known to strongly influence cell adhesion, cell migration and cell layer development. In order to gain a deeper knowledge about the effects of the inserted surfaces structures, *in vitro* samples are commonly modified with pillars, grooves and pits, among others.[195] Pillars and grooves can be fabricated with various heights, diameters, depths, widths and spacing distances and the dimensions of these structural features strongly affect the cell response (e.g. morphology, cell coverage area, adhesion, protein expression).[165,196] Furthermore, arrays of surface structures can be used to spatially arrange cells in a desired pattern.[170] By utilizing structures in the range of the respective cell diameter, cells can be trapped permanently at specific substrate site and subsequently used for single cell analysis.[197] A similar cell sorting can be achieved by coating specific areas of the sample substrate with cell attracting (cytophilic) and cell repelling (cytophobic) substances.[170,198] Laminin and fibronectin are, for instance, frequently used for cell attraction, whereas polymers such as PEG can be employed as passivation layers for cell repelling.[170,199] The chemical modification of the substrate surface subsequently leads to a spontaneous cell migration towards the attraction sites.[199]

Different types of modified surfaces were used over the last years to study the effect of structures on bone cells *in vitro*. For instance, while 2046 nm deep grooves cause the formation of mineralized bone matrices due to an upregulation of osteogenic markers, pillars strongly influence the cell adhesion by decreasing the surface energy.[200,201] Moreover, groove spacing in the nano-meter scale (400 nm) as well as a low pillar density can promote the osteogenic differentiation of hMSC.[202,203] Likewise, micropits with diameters in between 30-40 μm and nano-sized pillars were observed to stimulate osteogenesis by enhancing the bone cell adhesion, improving the cytoskeleton organization and increasing the FA area, which leads to an upregulation of factors such as OPN that is related to osteogenic functions.[77,204]

Apart from 2.5D surface structures, 3D scaffolds closely mimic the 3D architecture of the ECM and strongly influence the cell behavior by providing spatial cues. Hydrogels are a frequently used 3D platform in biological research and provide cells with realistic 3D cues.[161] They can be fabricated out of natural (e.g. alginate, collagen, silk, chitin) and synthetic polymers (poly (N-isopropylacrylamide) (e.g. PNIPAAm), poly(ethylene glycol) (PEG)).[205–207] By using these materials, a 3D network of interconnected pores is formed with dimeter in the μm scale (<20 μm).[208,209] Cells can be seeded into the interconnected structure and encapsulated in these pores, which permits the analysis of tissue growth and development *in vitro*.[161] Furthermore, hydrogels can be modified in order to provide adhesion points for a specific cell type (e.g. angiogenic endothelial cells), to release drugs over time and can be altered to be electrically conductive.[210,211] For instance, the integration of RGD sequences into the porous network can improve the cell viability, adhesion and serve as a guidance system for cell migration and ordered clustering.[161]

Hydrogels can be also modified to promote osteoblast differentiation, increase cell contractility and accelerate osteoblast maturation rates.[212,213] Furthermore, osteoblast adhesion and spreading can be enhanced by integrating positively charged surface elements.[211] While hydrogels possess similar properties like the natural ECM and can be modified to stimulate osteogenic linage commitment, a main drawback for bone cell applications is their low mechanical strength and stiffness.[76] These disadvantages can be partially compensated by combining natural polymers with inorganic materials like calcium phosphate (CaP) which leads to the construction of composite scaffolds.[214] For instance, the insertion of CaP nano particles leads to an increased mechanical strength and rigidity, which subsequently improves the osteoconductivity of the scaffold.[205] While hydrogels are an interesting 3D tool for analyzing the cell layer development *in vitro*, a direct stimulation and observation of a single cell remains challenging with them.

In addition, various types of 3D scaffolds can be produced with hard materials such as metals, ceramics and bioactive glass for *in vitro* cell study applications.[163,164] These scaffolds are fabricated with complex macro- and micro-architectures, which mimic properties of the ECM and provide cells with guidance cues for a controlled tissue development.[163,196] In addition, sophisticated fabrication methods like additive manufacturing allow the implementation of structures in the nano scale, which can influence the cytoskeleton of MSC cells or act as guidance patterns for neuronal cell growth.[215] Complex *in vivo* structures can be subsequently mimicked and used as 3D templates in order to study the spatial effect on cell behavior.[215]

Marino et al., for instance, utilized two-photon polymerization in order to fabricate a trabecula-like structure with a size of 200 µm x 200 µm x 27 µm and studied the reaction of SaOS-2 bone-like cells. They showed that only the interaction with the structure decreased the cell area while increasing the cellular z-depth, which gave the cells a rounder shape compared to a 2D cell culture.[216] Furthermore, the 3D microenvironment reduced the cell proliferation rate, promoted the osteogenic differentiation, which was linked to an elongation of the cell nucleus and increased the amount of hydroxyapatite deposits.[216] Similar studies on bone cells can be conducted with 3D mesh structures fabricated out of Ti and its alloys, materials which are frequently used for orthopedic implants.[212,217] These structures can be manufactured with network of interconnected pores, which allow cell ingrowth into the 3D space as well as promote cell-cell contact and cell-matrix interactions.[218] It was reported that the interaction between bone cells (e.g. MSC, osteoblasts) and porous metallic structures leads to increase levels of alkaline phosphatase and collagen I secreted by MSC, an enhanced maturation of osteoblasts as well as an enrichment of mineralized deposits compared to comparable planar counterparts.[212,217,219] Furthermore, these scaffold can be modified with nanostructures (e.g. titanium nanotubes), which cause, for instance, improved cell proliferation rates by providing a nanoporous topography as well as with magnetoelectric materials, which allow an electric stimulation of bone cells.[218,220]

In conclusion, surface patterning and 3D structures can be successfully used for exposing cells to spatial cues and thereby providing them with an adequate microenvironment, which is necessary for obtaining reliable data in *in vitro* experiments. Yet, both of these systems don't possess optimal properties for cell observation and stimulation. For instance, while a change in cell behavior can be easily monitored on patterned surfaces, they only provide cells with a 2.5D confinement, which doesn't completely resemble the *in vivo* cell conditions allocated by the ECM. In contrast to that, microplatforms consisting of interconnected pores offer cell various biological factors present in the natural environment. Yet, a direct observation of ambient effects on, for instance, single cell is strongly hindered by their scaffold architecture as well as the usage of opaque materials (e.g. Ti alloys). Therefore, a combination of the advantages of the above-mentioned systems would be desirable in order to create an optimal analysis platform for *in vitro* cell studies.

## 2.6.3 Microfluidic systems

Microfluidic systems are nowadays one the most frequently used devices for high throughput cell assays.[221] These systems allow an easy selection, trapping and analyzation of single cells, which is achieved by integrated electric fields, magnetic nanoparticles, acoustic waves and optical stimulation, among others.[221–223] These platforms are suitable for various different application such as drug screening, cell culture, molecule analysis, biosensing and protein manipulation.[166,224] Microfluidic systems usually consist of microchannels, chambers and surface elements, which allow the transportation and separation of cells by liquid flows in the laminar regime.[221] The channels are commonly fabricated by using polydimethylsiloxane (PDMS), a transparent elastomer which can be bound to, for instance, glass substrates as well as lithography processes, which permit a precise control over the channel geometry and dimensions.[221,225] A detailed cell analysis can be achieved by producing microchannels with scales close to that of individual cells and by applying trapping mechanism, which can be used to isolate cells.[223] Cell trapping methods can be further categorized into passive trapping strategies such as hydrodynamic trapping, which is based on the generation of cross-stream flows by changing the channel topography and active trapping by the usage of acoustic waves, electric and magnetic field.[169,226,227] Electric field traps, for instance, can be constructed by integrating gold electrodes into microchannels, which can be used to generate electric fields.[228] Consequently, electrical cell capturing is achieved by applying nonuniform electric fields to a cell body, which leads the generation of dielectrophoretic forces.[229] These forces were used to trap single yeast cells, to extract human breast cancer cell from blood as well as to isolate cervical carcinoma cells.[230,231] Furthermore, modifications to microfluidic platforms permit the detection and stimulation of cells inside the microfluidic channels. For instance, the integration of electronic sensors allows the detection of cell properties such as the cell morphology, ion channel activity and ion flow by impedance spectroscopy.[232] In addition, optical sensors can be used to analyze intracellular signals, pathogens and the release of cell products such as enzymes or proteins.[25,224]

Regarding bone cell research, microfluidic systems were engineered to stimulate bone cells with factors (e.g. flow shear stress, electric fields) relevant in bone development and to analyze bone cell reactions with sensor devices, which were described above.[233,234] Bischel et al., for instance, utilized a microfluidic platform to co-culture bone marrow stromal cells (MC3T3-E1) with an osteotropic prostate cancer cell line (C4-2B) in order to study cancer cell invasion into

bone.[235] They showed that the cross-talk in between the both cell types increased the invasive capacity of the cancer cells, as a higher number of cellular protrusions were formed by C4-2B cells in the microfluidic setting compared to a monoculture.[235] In addition, the device was modified with multi-photon imaging techniques and an enzymatic activity assay, which led to a reduction of the number of cells and reagents needed for obtaining reliable data compared to traditional systems.[235] Moreover, sensor devices with impedance measurement capacities can be used to monitor the osteogenic differentiation state of bone cells and subsequently permit a discrimination between MSC and mature osteoblasts.[236,237] Microfluidic systems can also be used to influence the cell linage commitment by the integration of pumping systems, which provide a shear stress that promotes the osteogenic differentiation of bone cells.[238,239] Besides, hydrogels can be integrated into the microfluidic channels and therefore provide additional 3D cues for cell stimulation.[240] Complex multi-cellular platforms can be therefore created, which can be used to monitor the interactions between different cells types within a highly controllable 3D environment.[207,241,242] Microfluidic systems are in general powerful microplatforms, which offer various ways to monitor and manipulate cells *in vitro*.

## 2.6.4 Tubular microstructures

Tubular microscaffolds (TS) are another type of 3D microplatform, which can be used for a variety of different applications. These microstructures are fabricated with standard photolithography processes, that are commonly used in the chip industry for the production of semiconductors and microelectromechanical systems.[243] The TS fabrication is based on the deposition of 2D stress-engineered nanomembranes, which subsequently self-assemble into structures in the microrange.[244] Moreover, the layer stress and the structure size can be manipulated by depositions factors such as the environmental temperature, the deposition rate and the oxygen background.[26] Subsequently, large TS arrays with various different structure-to-structure distances can be easily fabricated on a single sample.[245] Likewise to microfluidic systems, additional functional layers such as thermoresponsive layers and electrodes can be added into the TS structure as well as several different materials can be used for their structural shells (e.g. metals, magnetic materials, polymers, oxides, glass).[245–249] As a consequence, TS are a highly modifiable platform which can be used in several fields with highly distinct applications (e.g. sensors, photonic applications, energy storage systems, cell studies).[247,250–254]

## 2.6.4.1 Single cell analyses with tubular microscaffolds

In this regard, transparent TS with dimension close to the cells size can be used as 3D microenvironment to study the individual cell behavior in a constricted space. The first attempts to study the confinement effects on single cells were conducted with yeast cells in glass (SiO/SiO$_2$) TS coated with an Al$_2$O$_3$ layer.[255] A directed cell growth was observed inside the TS leading to a cell proliferation along the TS axis, which was in stark contrast to a random cell growth in the standard 2D cell culture.[255] Viability assays were conducted on yeast cells located inside the TS, which confirmed a high cell survival rate inside the constricted environment demonstrating that the nutrition flow and oxygen supply into the TS was sufficient for cell division and proliferation processes.[255] Moreover, the space constriction of TS with diameters (3.5 µm diameter) smaller than yeast cell average diameter (6 µm) provoked a cell morphology change, which led to an elongation of the cell body.[255] These findings were confirmed in subsequent experiment using more complex cells such as neuronal stem cells. These cells closely aligned their cell bodies to the TS geometry and exhibited a higher cell survival rate compared to the cells on a 2D surface.[256] Furthermore, the TS functioned as guidance cues for the axon growth, which led to the formation of a neurite network in the location of a TS array.[256] The importance of a realistic *in vitro* 3D microenvironment was further emphasized in cell experiment with neural stem cells. The space constriction caused a morphology change to a round cell shape, which resembles the natural *in vivo* morphology of this cell type.[254] Moreover, the cells utilized a completely different migration mode inside the TS compared to cell on a 2D surface. After the cells entered the TS, they directly switched from a mesenchymal migration mode into an amoeboid-like migration.[254] In addition, studies with cancer cells (HELA cells, human osteosarcoma cells) demonstrated, that a minimum free space is required for a successful cell division process and a long-term cell viability.[257,258] It was observed that small TS diameters (<10 µm) provoked a change in the nucleus aspect ratio, which inflicted chromosome segregation errors leading to an increased cell death rate over time.[258,259] All in all, the TS platform is a powerful *in vitro* tool, which provides cells with 3D cues of the *in vivo* environment while allowing single cell monitoring by optical microscopy at the same time. This platform can be therefore used to acquire reliable *in vitro* data.

# 2.7 Effects of structures and constriction on cells

Like depicted in the previous **Sections (2.6.2-2.6.4)**, providing cells with a realistic 3D *in vitro* environment is important in order to obtain reliable data. Spatial confinement and surface curvature can be found in many *in vivo* microstructures like the ECM and macroscopic structures like the bone trabecular network.[150,260] Consequently, microsystems were recently developed in order to analyze the effects of these cues by the integration of curved elements and by confining cells spatially. Thus, this section gives an overview over how spatial confinement and surface curvature affect the cell shape, behavior and the cell linage commitment.

## 2.7.1 Confinement effects and *in vivo* migration modes

The cell migration (see **Section 2.3.2**) is strongly affected by the respective microenvironment. Accordingly, recent studies with cells in realistic 3D environments demonstrate an alternative cell migration mode which allows cell movement without the usage of integrin-based attachment complexes (FA).[84,261] The integrin-free migration was observed, for instance, with genetically modified leukocytes lacking the possibility to express integrins, yet still depicted the capacity to migrate inside 3D scaffolds.[262,263] Confinement plays a pivotal role in controlling cell migration, as it can provoke a switch of the migration mode to non-adhesive migration, which is absent on 2D substrates. This alternative migration-mode can be triggered *in vitro* by structures such as non-adhesive gels, glass plates and microchannels, in which higher cell migration velocities were observed compared to 2D conditions.[89,264,265] For instance, higher migration speeds were found in microchannels in between 6-10 µm compared to 50 µm channels as well as an additional inhibition of the respective microtubule polymerization didn't influence the migration speed in channels $\leq 10$ µm.[266] Furthermore, the amount of mature focal adhesions and actin stress fibers were also reduced with a decreasing channels width (50 µm – 3 µm).[266,267]

Several theoretical explanations for integrin-free migration such as chimneying force transmission, cell-substrate intercalation and flow-friction-driven force transmission were proposed and described lately.[84] For instance, cell-substrate intercalation could take place on rough 3D environments, in which laterally formed cell projections penetrate small gaps of the

surrounding 3D matrix and thereby generate traction forces strong enough to enable cell movement.[268–270] In contrast to that, smooth surfaces with high constriction levels like artificial microchannels, could favor chimneying, which depends on tight contact between multiple cell projections and the channel boundaries.[271] As a consequence, actin networks are formed perpendicular to the channel walls and the continuous actin polymerization process build up a pressure gradient, which is higher at the position of the cell nucleus.[272] The resulting pushing forces subsequently generate a viscous friction at the cell- channel-wall interface, which allows the cells to move towards the positions with low pressure levels.[272]

However, the discrimination between different migration modes remains challenging as the morphology of the cells utilizing integrin-free migration is similar to amoeboid-like cells.[273] Thus, while the migration behavior in 3D confinement is still not completely understood, geometric cues are powerful factors, which can be used to steer the cell behavior and control the stem cell linage commitment.

## 2.7.2 Substrate curvature

In addition to the above-mentioned confinement effects, surface curvature, which naturally occurs in most 3D body structures, also strongly affects the cell adhesion and migration behavior.[260] Similar to cell confinement, curved objects force cells to change their morphology in order to adapt to the curved surface geometry, which directly affects the internal cytoskeletal tension.[260] Kilian et al, for instance, restricted human MSC into certain shaped areas and demonstrated that the curvature alone can change the cytoskeletal tension. [274] Consequently, an increase of the cytoskeletal contractility was observed within star-like shapes with concave edges, which provoked an osteogenic linage commitment. This results are in line with previous studies that demonstrated an upregulation of osteogenesis on rigid surfaces with a high stiffness. [194,275] In contrast to that, shapes that induced a low contractility and a round cell morphology promoted adipogenic differentiation. [274]

Furthermore, concave and convex cylindrical structures (diameter between 250-1000 µm) were shown to provoke changes in the morphology and migration mode of human MSC. These cells were subsequently observed to utilize a fast pull movement in contact with a curved object, which led to an increase of the migration speed.[276,277] In addition, single human MSC were observed to actively migrate into concave pits in which they adopted a round morphology and

possessed a nearly spherical cell nucleus.[276,278] It was demonstrated that whole cell layers can sense curvature elements on the substrate surface and react to them in a crystal-like manner, which results in the minimization of the cell layer surface energy.[279–282] Various studies also indicated that convex structures can promote osteogenesis as well as on highly concave structures can upregulate the a formation of osteoid-like tissue by pre-osteoblastic cells.[276,282] Therefore, although current research demonstrated that curvature plays an important role in influencing the cell behavior, the exact mechanisms remains unclear.

# 3 Materials and Methods

**Section 3** is based on the publication (journal Small, License Number: 5090201201398):

R. Herzer, A. Gebert, U. Hempel, F. Hebenstreit, S. Oswald, C. Damm, O. G. Schmidt, M. Medina-Sánchez: Rolled-Up Metal Oxide Microscaffolds to Study Early Bone Formation at Single Cell Resolution. *Small* **2021**, *17*, 2005527.

## 3.1 Microscaffold fabrication

All microtubular scaffolds were produced by standard photolithography using glass as a substrate material. The glass substrates were cleaned with acetone and isopropanol each for 5 minutes in an ultrasonic cleaner prior to usage. They were afterwards treated with an oxygen plasma cleaner (device) for 5 minutes. In general, different setups were utilized for the fabrication of $SiO/SiO_2/Al_2O_3$ (SOA) and Ti-45Nb-oxide (wt%) (TNO) samples. The specific parameters and devices used for the production of the different types of the TS are described in the following sections.

### 3.1.1 Glass tubular microscaffolds

Glass ($SiO/SiO_2/Al_2O_3$ (SOA)) tubular microscaffolds with rectangular structures were fabricated with widths in the range of 100 - 300 μm and rolling lengths of 125 - 400 μm using a standard photolithography procedure. Additional information can be found elsewhere.[258] Briefly, cleaned glass samples were spin-coated with AR-P 3510 (Allresist GmbH, Germany) positive photoresist for 35 sec with 3500 rpm and afterwards baked on a hotplate at 90°C for 3 min. Consequently, the samples were patterned with a maskless aligner (MLA 100 maskless aligner, Heidelberg Instruments kJ, Germany) and developed inside a 1:1 solution of AR 300-35 and Deionized (DI) water. In the next step, layers of SiO (5 nm) and $SiO_2$ (30 – 100 nm) were deposited by e-beam evaporation (DREVA OPT 400, VTD, Germany) with a 30° glancing angle in order to obtain an uncovered area, in which the roll-up process was initiated. The residual photoresist was then released by immersing the samples inside DMSO for 10 minutes, which led to the self-assembly of the TS. Afterwards, the DMSO solution was exchanged with

isopropanol and the samples were dried by utilizing a critical point dryer (Leica EM CPD300, Leica Microsystems GmbH, Germany). In order to stabilize the outer hull of the TS further, a mandatory step for avoiding structure release when using them inside cell culture medium, 20 nm of $Al_2O_3$ was deposited by Atomic Layer Deposition (ALD, FlexAL II, Oxford Instruments, UK). Furthermore, the diameter of the TS was pre-determined by changing the thicknesses of the $SiO_2$ layers.

### 3.1.2 Ti-45Nb (wt%) tubular microscaffolds

For the fabrication of oxide tubular microscaffolds, firstly a sputtering target of a Ti-45Nb (wt%) alloy (ATI specialty alloys & components, USA) was used to produce thin strained layers of Ti-45Nb (wt%) (TN) or Ti-45Nb-oxides (TNO) onto glass substrates. Similar to the SOA-TS samples, Ti-45Nb-oxide tubular microscaffolds (TS) were fabricated using a self-rolling process (see previous works.[283]). In order to prepare TNO-TS structures, glass samples were pre-patterned similarly as the SOA samples, but with AR-P 3510 (~1.6 μm) or Ge (20 nm) as sacrificial layers. For producing Ge layers, cleaned glass samples were spin-coated with an adhesion layer (Ti Prime, 3500 rpm) for 20 sec followed by a heading step at 120°C. Subsequently, AZ 5214 E photoresist (The MicroChemicals GmbH, Germany) was spin-coated (4500 rpm, 45 sec), heated on a hotplate (90°C, 5 min) and exposed to UV-light with a maskless aligner (MLA 100 maskless aligner, Heidelberg Instruments kJ, Germany). In the next step, the photoresist mode was changed from positive to negative with an additional heating step (120°C, 2 min), which was followed by flood exposure (30 sec) and development by immersing the glass sample in AZ 726 MIF developer (The MicroChemicals GmbH, Germany) for 30-50 sec. Ge layers were deposited onto the prepared windows using e-beam evaporation (MP600s, PLASSY Bestek, France) and the residual photoresist was released with a lift off process using acetone, isopropanol and DI water until all redundant metal was removed from the surface. In order to deposit additional strain layers, windows were fabricated in a similar process in proximity to the Ge-layer.

Additional strain-layers (SiO, $SiO_2$, $TiO_2$) were deposited onto both sacrificial layers (AR-P, Ge) to increase the pre-strain followed by strained TN/TNO bilayers. Alternatively, TN or TNO layers were directly deposited onto the pre-patterned square-like structures (widths in the range of 100 - 300 μm, rolling lengths between 125 - 400 μm). The layers were deposited either by sputtering or by Pulsed Laser Deposition (PLD, KrF-Excimer-Laser (LPX305), Lambda Physik, Germany). The PLD laser was located 10 cm apart from the target and operated with

248 nm (UV), which generates an energy of 160 mJ/laser pulse on the Ti-45Nb target area (1.5 mm x 3.5 mm). The oxidized PLD layers were deposited with an $O_2$ background (30%) and a pressure in between 0.1 - 0003 mbar. The pure (non-oxidized) TN layers were sputtered with a pure Ar background and with flat (0° angle) deposition (Q150T ES, Quorum Technologies Ltd, UK). The deposition of TNO was performed with an oxidized Ar background (30-50% $O_2$) within the sputtering chamber (nano PVD, Moorfield Nanotechnology, UK). In the next step, the rolling of the thin films was initialized by dissolving the Ge sacrificial layer using a 3% $H_2O_2$ solution in DI. Subsequently, $H_2O_2$ was replaced by isopropanol and finally placed in a critical point dryer (Leica EM CPD300, Leica Microsystems GmbH, Germany) for drying. Finally, an additional 30 nm TiNb-oxide layer was deposited onto the tubular microstructures to enhance their structural stability.

For the PLD process, glass samples with ARP photoresists and $SiO/SiO_2$ or only $SiO_2$ layers were prepared similar to SOA samples. Thereafter, a 20 nm layer of TiNb was deposited onto the $SiO_x$ layer with a 30° glancing angle and the self-assembly was initiated by incubation in DMSO for 10 min.

The non-oxidized TiNb-TS were oxidized after the roll-up process inside an oven (Muffelofen CSF1100, Ströhlein Instruments, Germany) at 200-600°C for 2-6 h. The resulting TS diameter was pre-determined by modulating the thickness and stress of the particular strain-layers.

## 3.2 Surface analysis methods

### 3.2.1 SEM and TEM measurements

Briefly, hMSCs were fixed with glutaraldehyde (3%, Sigma-Aldrich, USA) and gradually dehydrated with 25%, 50 %, and 100 % ethanol for 7 min each, respectively. Afterwards, a 10 nm Pt layer was deposited onto the samples (inorganic or biological). The TS Scanning Electron Microscope (SEM) images were obtained with a DSM 982 (Zeiss, Germany) instrument operated at 5 kV. The crystallinity of the deposited TiNb-oxide was analyzed by preparing a lamella out of a thin film using an NVision 40 (Zeiss, Germany), which was operated at 30-50 keV. The CaP content inside the TS was analyzed after at least 3 weeks of differentiation medium (see **Section 3.3**) cell culture with Focused Ion Beam (FIB) lamellae from the tubular microscaffolds using a FEI (USA) Helios nanolab 600i, which was operated at 5-30 kV. All lamellae were analyzed using a FEI (USA) Tecnai G2 transmission electron microscope (TEM, LaB6 filament) operated at 200 kV acceleration voltage, which is equipped with an Energy-

Dispersive X-ray spectroscopy/Scanning Transmission Electron Microscope (EDX/STEM) unit and a Si-Li-detector (Oxford Instruments, UK) with a resolution of 136 eV (Mn-K$\alpha$).

## 3.2.2 AFM and contact angle measurements

For the Atomic Force Microscopy (AFM) measurements, a Bruker (USA) microscope was used. $SiO/SiO_2/Al_2O_3$ and TiNb-oxide samples with and without TS were prepared and at least three positions per sample were analyzed. To determine the roughness of the surface, the Root Mean Square (RMS) was calculated using 1 $\mu m^2$-area images.

Contact angle measurements (OCA contact angle system, DataPhysics Instruments, Germany) were conducted applying several drops of distilled water to different locations on the sample surface. Thereafter, the drops were measured using a high-resolution camera and the average angle of the water droplets was calculated. For each material (TNO and SOA), three samples and three locations per sample were used.

## 3.2.3 XRD and XPS measurements

Grazing incidence X-ray diffraction (XRD) analysis of deposited layers was carried out by means of a Philips X'Pert Pro thin film diffractometer (PANalytical, NL). Cu-K$\alpha$ radiation was used (40 mA, 40 kV) with incidence angles of 2, 4 and 6° and the 2$\theta$ range was from 10 to 80°. X-ray photoelectron spectroscopy (XPS) was used to characterize the chemical state of the sputter-deposited layers. These measurements were carried out with a PHI 5600 CI (Physical Electronics, Germany) spectrometer, which is equipped with a hemispherical analyzer running at typical pass energies of 94 eV for survey and of 29 eV for detailed spectra, respectively. The analysis area was around 800 $\mu m$ in diameter. Monochromatic Al-K$\alpha$ excitation (350 W) was used at both 45° X-ray impact and electron emission angle with respect to the sample surface. Depth analysis was carried out using $Ar^+$ ions (3.5 keV, 0.4 $\mu A$, scan size 2 mm x 2 mm, impact angle around 30°) with sputtering intervals of 1 min, which results in a sputtering rate of 3.3 nm/min in $SiO_2$; here Mg-K$\alpha$ excitation (350 W) was applied. Quantitative analysis of the spectra was done using the PHI-MultiPak software with single element standard sensitivity factors.

## 3.3 Cell culture

Human Mesenchymal Stem Cells (MSC) up to passage 5 were used for the cell experiments provided by Dr. Wobus (Stem Cell Lab 2, Universitätsklinikum Carl Gustav Carus Dresden (MTZ), Germany). The donors fulfilled the standards for bone marrow donation (e.g. free of HIV, HBV, and serious illness). Donors were informed and gave their approval for the current research. The study was approved by vote of the local ethics commission (EK263122004). The experiments were repeated three times with three samples per setting.

Cells were seeded in a density of 7,000 hBMSC cm$^{-2}$ in culture medium Dulbecco's Eagle's medium low glucose 1 g L$^{-1}$ (DMEM, Sigma-Aldrich, USA) with 10% heat-inactivated fetal calf serum (FCS, Sigma-Aldrich, USA), 1% PenStrep (Sigma-Aldrich, USA) and 1% sodium pyruvate (standard medium, SM, Thermo Fisher, USA). Cell differentiation was induced by Differentiation Medium (DM = SM supplemented with 10 mM β-glycerophosphate (Sigma-Aldrich, USA) 300 μM ascorbic acid (Sigma-Aldrich, USA) and 10 nM dexamethasone (Sigma-Aldrich, USA) at day 4 after the cell seeding. The medium was changed every 3-4 days during the experiments.

### 3.3.1 Proliferation assay

The metabolic activity of the cells was determined using a 3-(4,5-dimethylthiazol-2-yl)-5-(3-carboxymethoxyphenyl)-2-(4-sulfophenyl)-2H-tetrazolium assay (MTS assay, Cell Proliferation Assay Kit, Abcam, UK). The MTS assay is based on the reduction of the MTS tetrazolium compound, which is added into the cells culture medium together with intermediate electron acceptors.[284,285] Subsequently, the intermediate electron acceptors penetrate viable cells and become reduced by NAD(P)H-dependent dehydrogenase enzymes, which are only functional inside viable cells.[284,285] The reduced intermediate electron acceptors exit the cells and convert the MTS tetrazolium compound into the soluble formazan product.[284,285] The quantity of the formed formazan dye is thereby considered to be directly proportional to the number of viable cells in the cell culture.[284,285]

The assay was conducted by replacing the cell culture medium by a 10% MTS solution in sterile cell culture medium. Subsequently, the well plates were incubated for 2 h at 37 °C (incubator, 5% CO$_2$). The supernatant was transferred into a 96 well plate and the absorbance of the solution

was photometrically analyzed at 490 nm. The metabolic activity was measured at days 1, 2 and 3 after cell plating.

### 3.3.2 Immunofluorescence staining

After aspirating the cell culture medium, cells were washed with PBS (Sigma-Aldrich, USA) and fixed with 4% formaldehyde (Sigma-Aldrich, USA) for 10 minutes. After a second washing step, cell membrane permeabilization was performed with 0.1% TritonX-100 (Sigma-Aldrich, USA)/PBS solution and then the samples were incubated with the primary antibody for 1 h (19.5 µl anti-vinculin-IgG (Sigma-Aldrich, USA) in 1 ml 1% BSA (Sigma-Aldrich, USA) (1:50). After blocking the cells, they were incubated with the secondary antibody (Alexa 568 goat-mouse IgG (Thermo Fisher, USA) (1:50) and Alexa 488-phalloidin (Thermo Fisher, USA) (1:50), suspended in PBS for 1 h). Subsequently, the cells were incubated for 10 minutes in DAPI (4',6-diamidino-2-phenylindole, Thermo Fisher, USA) and visualized using a Cell observer fluorescence microscope (Zeiss, Germany) and a Laser Scanning Confocal Microscope (LSM 780)/Fluorescence Correlation Microscopy (FCS) (Zeiss, Germany), inverse microscope of the Light Microscopy Facility (CMCB at Technische Universität Dresden).

### 3.2.3 TNAP activity

MSC were seeded onto TNO, SOA and TCPS samples respectively and cultured with SM for 3 days. Subsequently, the SM was replaced by DM and cells were kept in the medium for up to 15 days. All TNAP activity assay steps were performed on ice. After washing of the cell layers twice with PBS, 100 µl of ALP lysis buffer supplemented with complete protease inhibitor (Mini Protease Inhibitor Cocktail, Roche, Switzerland, 7:1) was added to each well. Thereafter, the samples were incubated for 10 minutes with gently shaking. Subsequently, the cells were scraped, the lysate transferred into reaction tubes and then centrifuged at 13000 rpm for 30 minutes at 4 °C. Afterwards, the supernatant was transferred into new reaction tubes. For the determination of the TNAP activity, 10 µL supernatant of the lysate was transferred in duplicate into a 96 well plate and then 100 µL substrate buffer supplemented with 3.6 mM pNPP (p-nitrophenylphosphate, 13.5 mg / 10 mL substrate buffer, Sigma-Aldrich, USA) was added into each well. The well plate was incubated for 30 minutes at 37 °C. Afterwards, 100 µL of 100 mM NaOH (Sigma-Aldrich, USA) was added to stop the reaction and then the plate was cooled

for 10 minutes at room temperature. The released p-nitrophenolate was photometrically measured at 405 nm. Additionally, a linear calibration curve prepared with p-nitrophenol (Sigma-Aldrich, USA) was used to calculate the TNAP activity. The protein concentration of the cell lysates was determined with a BCA (bicinchoninic acid, Thermo Fisher, USA) assay. The BCA-assay was used to analyze the total amount of proteins formed by the cells on the particular samples in parallel to the TNAP activity test. TNAP activity was then related to the protein content of the lysates (specific enzyme activity [mU/mg protein]). To analyze the specific TNAP activity of the cells, the total amount of produced proteins is therefore compared to the TNAP proteins produced by the cells. The same lysate was used for TNAP activity determination in the enzyme activity assay as well as for protein determination with BCA reagent. Briefly, 25 µL of the lysate was added into a 96 well plate. Subsequently, 200 µL of the BCA working solution (reagent A and B; 50:1) was added to the wells. The well plate was incubated for 30 minutes at 37 °C and the absorbance was measure at 562 nm. A linear calibration curve determined with Bovine Serum Albumin (BSA) as a standard was used to calculate the protein concentration.

### 3.2.4 qPCR and ELISA analysis

The quantitative real-time Polymerase Chain Reaction (qPCR) and Enzyme-Linked Immunosorbent Assay (ELISA) eanalyses were performed by collaboration partners (Hempel group) at the MTZ (TU Dresden) similar to previous PCR studies.[286–288] In short, TNO and SOA samples with TS (3D) and without TS (2D) were placed into suspension well plates and human MSC were seeded onto the samples. Additionally, MSC were seeded onto TCPS adherent well plates, which were used as control samples. After a 3-day proliferation phase in SM, samples were either immersed in SM or in DM for 11 subsequent days. In order to conduct the qPCR measurements, a RNeasy Mini Kit (Qiagen, Hilden Germany) was used to prepare RNA from cell lysates for the gene expression analysis and the synthesis of cDNA was carried out with a QuantiTect Reverse Transcription Kit (Qiagen, Hilden Germany). Afterwards, the real time PCR reactions were performed with a RotorGene PG-3000 PCR 854 machine with a RotorGene SYBR Green PCR KIT (Qiagen, Hilden, Germany) and the relative expression values were analyzed with the RotorGene software. The house keeping genes (Actin, GAPDH, RPS26) and primers used for the qPCR are depicted in **Table 3.1**. The ELISA analysis was performed with a DuoSet ELISA Development Kit (BioTechne, USA) and conducted following the manufacturer's assay procedure. In short, 100 µl of sample or standard were added into

wells, respectively and incubated for 2 h at room temperature. Samples are washed 2 times with ELISA wash buffer and subsequently 100 µl of detection antibody was added to each well. After two additional washing steps, 100 µl working solution (streptavidin-HRP A) was added and the well plates were incubated for 20 minutes (room temperature). Afterwards, samples were washed twice, 100 µl substrate solution was added to each well and they were incubated for 20 min at room temperature. Finally, 50 µl stop solution was added and the absorption spectra were measured with a SpectroStar (BMG Labtech, Germany) device at 450 nm.

**Table 3. 1: Primer pairs used for the qPCR analysis** [286–288]

| Gene | Forward primer | Binding position | Reverse primer | Binding position | Product length |
|---|---|---|---|---|---|
| Actin | AATGTGGCCGAGGACTTTGATTGC | 1414 – 1437 | TTAGGATGGCAAGGGACTTCCTGT | 1485 – 1508 | 95 |
| GAPDH | TGTTCGTCATGGGTGTGAACCA | 563- 584 | TGATGGCATGGACTGTGGTCAT | 698- 718 | 156 |
| RPS26 | CAATGGTCGTGCCAAAAAG | 286- 304 | TTCACATACAGCTTGGGAAGC | 454- 474 | 189 |
| TNAP | AGAACCCCAAAGGCTTCTTC | 1222 - 1241 | CTTGGCTTTTCCTTCATGGT | 1276 - 1295 | 74 |
| BSPI | AAGCATGCCTACTTTTATCCTCATT | 281- 305 | CATTCGATTCTTCATTGTTTTCTC | 405- 429 | 148 |
| Coll (I)α1 | GGGATTCCCTGGACCTAAAG | 1866 - 1885 | GGAACACCTCGCTCTCCA | 1911 - 1928 | 63 |
| Coll (I)α2 | TCTGGAGAGGCTGGTACTGC | 3016 - 3035 | GAGCACCAAGAAGACCCTGA | 3060 - 3079 | 64 |
| OPG | ACACCAGTGACGAGTGTCTA | 475- 494 | GGGCAGCTCCTATGTTTCAA | 606- 625 | 151 |
| RANKL | TGATTCATGTAGGAGAATTAAACAGG | 200– 225 | GATGTGCTGTGATCCAACGA | 262– 281 | 82 |

## 3.2.5 Alizarin Red Staining and Von Kossa Staining

The nodule mineralization was analyzed with an Alizarin Red S staining kit (Sigma Aldrich, USA) and a Von Kossa staining kit (Abcam, UK). For both assays, the medium was aspirated at day 21 with DM. Cells were washed 3 times with PBS, fixed with 200 µl 4% formaldehyde per well for 15 min at room temperature and washed 3 time with DI water. The samples were incubated for 20 min with gently shaking in 1 mL of 40 mM Alizarin Red S solution. After aspiration of the staining solution, each sample was washed with DI $H_2O$ 5 times. For the Von Kossa staining, the cells were fixed and incubated for 60 minutes (25 °C) with silver nitrate

solution (5%) under UV light. Subsequently, the cells were washed 3 times with DI $H_2O$, incubated for 10 min in Sodium Thiosulfate solution (5%), washed (3x DI $H_2O$) and incubated in Nuclear Fast Red Solution for 5 min. The staining solution was removed and the samples were washed 3-timestimes with DI $H_2O$. Images were taken with an inverted microscope and a color camera. Samples with TS and DM but without cells were used as a control.

### 3.2.6 Live/dead staining

The viable cells were stained with fluorescein diacetate (FDA 5 mg ml$^{-1}$, Sigma-Aldrich, USA) and with propidium iodide (PI 2 mg ml$^{-1}$), Thermo Fisher, USA) for dead cells. The cell culture medium was removed and the samples were incubated 5 min at room temperature in the staining solution. After removing the staining solution, the samples were washed with PBS and analyzed with a fluorescence microscope (Cell observer, Zeiss, Germany). This

### 3.2.7 Statistical analysis

The data normality was verified using a Kolmogorov-Smirnov normality test. The significance of parametric data was assessed by performing an independent two-sample *t*-test.
The significance of non-parametric data was assessed by performing a Mann–Whitney U test. OriginLab (b9.4.0.220, OriginLab Corporation,USA) was used to generate the significance levels. *P*-values < 0.05 were considered as significant. The particular ranges of *p*-values are indicated in the corresponding figure legends and by asterisk in the figures.

# 4 Results and Discussion

In order to fabricate a suitable *in vitro* platform, which allows the observation of single bone cell-implant material interactions, several requirements like a high biocompatibility and an adequate geometrical structure have to be fulfilled. The main challenges of this project are to create an adaptable transparent microsystem while maintaining the material characteristics of the Ti-45Nb (wt%) raw material such as a high Nb content. This is an important requirement to produce reliable *in vitro* data of the cell behavior, as cell reactions differ dependent on their particular chemical and physical environment.[289]

According to the above-mentioned challenges, the first part of this results section addresses the fabrication of Ti-45Nb-based (wt%) oxide tubular microscaffolds by different deposition techniques (**Section 4.1**) and the characterization of the deposited thin layers (**Section 4.2**). Thereafter, cell experiments at a whole cell population level and with single cells are conducted to characterize their long-term viability and their material dependent reactions with the TS-platform (**Section 4.3**). Subsequently more elaborated experiments are conducted to assess the influence of the respective material on the cell differentiation potential and to characterize a potential initial bone formation inside the TS (**Section 4.4**). Finally, the mineralization state is investigated with biological and physical methods (**Section 4.5**).

## 4.1 Tubular microscaffold fabrication

The fabrication of tubular microscaffolds (TS) suitable for optical cell observation was one of the main challenges of this doctoral thesis. The here presented TS were designed to mimic porous structures, which exists in bulky implant scaffolds and improve the bone ingrowth in the macro scale. Consequently, the usage of this *in vitro* microplatform should contribute to facilitate a detailed analysis of bone cell behavior in constricted space and early bone ingrowth into a closely confined environment.

In order to create a realistic 3D structure, different deposition methods were tested and utilized to create thin layers out of the raw material Ti-45Nb (wt%) and with a similar material composition as the original material. Preserving the particular material composition is an important factor, as recent studies showed that the Nb content, for instance, influenced the cell

behavior.[290,291] Since the TS fabrication process is based on strain-engineering and photolithography, several factors such as the deposited layer thickness, the deposition rate and the oxygen background have to be taken into account in order to form TS in the required size.[26] Consequently, the challenge was to find a compromise in between sufficient layer strain, which is necessary for the roll-up process, an adequate transparency for high resolution optical microscopy and deposition parameters for an optimal material composition. Furthermore, the diameter of the obtained TS should lie in the range of the cell size (average diameter: 12.6-30.4 µm), which is dependent on the level of constriction.[45,46]

Accordingly, two different deposition methods, sputtering and Pulsed Laser Deposition (PLD) are introduced in the first part of this section, which were used to produce the required thin layers (**Section 4.1.1**). Subsequently, the sample fabrication steps are displayed with were conducted by using a lithography process and two different sacrificial layers (**Section 4.1.2**). Afterwards, TS fabrication by non-reactive deposition methods is described (**Section 4.1.3**) as well as the subsequent terminal oxidation process (**Section 4.1.4**). In the second part, reactive deposition methods are exhibited, which allow a direct deposition of oxidized layers and the formation of transparent TS (**Section 4.1.5**). In addition, the fabrication of glass TS samples is described (**Section 4.1.6**), which were used as control samples for the cell experiments.

## 4.1.1 Deposition principles and devices

Sputtering and PLD are two physical vapor deposition techniques that can be used to produce thin films, but are conducted with different deposition principles. In short, the sputtering process is based on the momentum transfer between charged particles such as $Ar^+$ and the target material (see **Figure 4.1 a**).[292] These high energy ions are formed in a plasma, accelerated towards the target and collide with it, which leads to ablation of individual atoms from its' surface.[292] This continuous ion bombardment consequently results in the formation of a thin layer of the raw material on the substrate surface, which is placed in a certain angle to the target position.[293] The sputtering chamber can also be partially filled with a reactive gas such as oxygen, which allows the oxidation of the target material during the sputtering process (**Figure 4.1 b**).[292] The PLD process on the other hand, is performed by focusing high energy laser pulses onto the target material, which leads to a material ablation followed by a thin layer formation.[294] In short, the laser pulse energy is absorbed by a small amount of matter on the target surface, which leads to an evaporation of the affected material (**Figure 4.1 c**).[294] This results in a formation of a plume
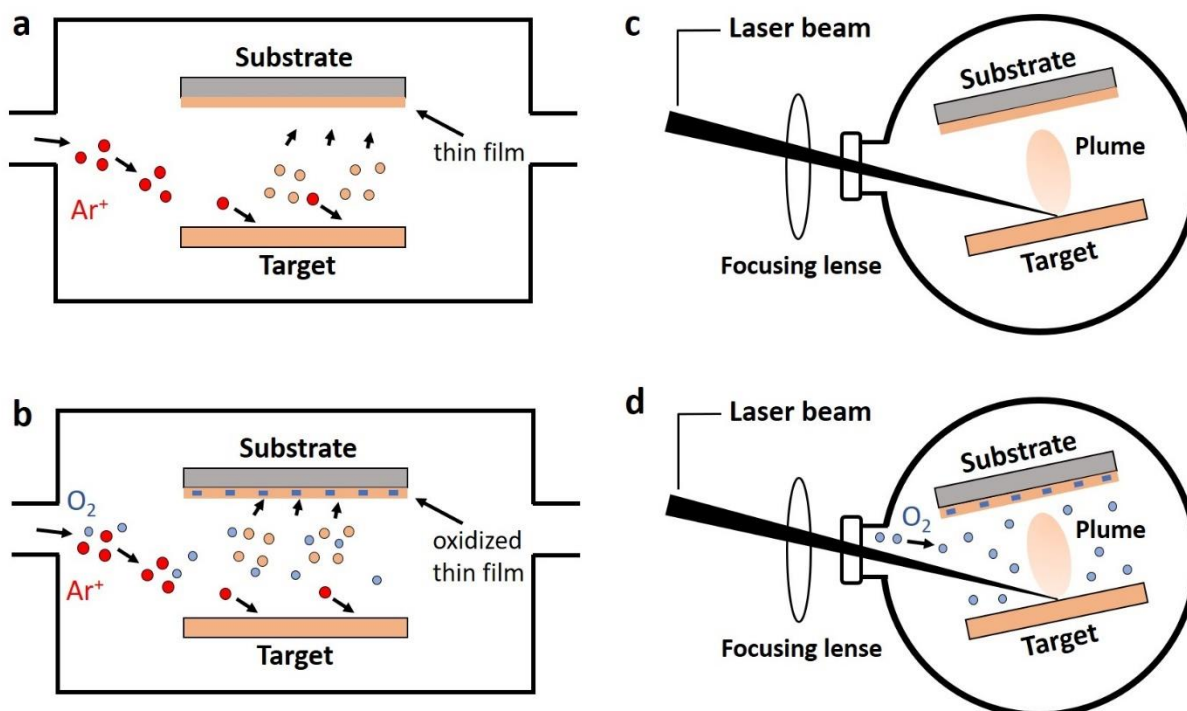
**Figure 4. 1:** Deposition methods. Sputter deposition without (a) and with an oxygen background (b). Schematic of a thin layer production with a non-reactive (c) and reactive (d) PLD process.

(hot plasma), which propagates through the deposition chamber and subsequently condenses onto the substrate in the vicinity.[294,295] Since larger material areas of the initial material are ablated at the same time in the PLD process, a complex material stoichiometry can be transferred with a high accuracy to the substrate.[295–297] Similar to reactive sputtering, a gas (e.g. oxygen, nitrogen) can be introduced into the deposition chamber (**Figure 4.1 d**).[295] Consequently, a material oxidation can be achieved during the deposition process, as the gas molecules can interact with the ablated raw material localized in the plume.[295,298]

Furthermore, since the elemental composition of an alloy consisting of Ti and Nb should be closely transferred to the TS, different deposition methods were used in order to obtain the optimal settings for the stoichiometry displacement. Consequently, two sputtering and one PLD device were utilized in this thesis to produce thin films of the raw material Ti-45Nb (wt%) (**Figure 4.2**). A target was fabricated (**Figure 4.2 a-i**), which could be inserted into all instruments, respectively (**Figure 4.2 a-ii, b-i, c-i**). In addition, while layers were deposited without an angle in case of the sputtering device, a 30° angle was used in the reactive sputtering and PLD setting. In order to fabricate tubular microscaffolds, thin material layers were deposited onto glass substrates, which were placed into the respective sample holders (**Figure 4.2 a-iii, b-i, ii, c-ii**). Moreover, since the holder area was comparable small in case of the sputtering and PLD device, it was only possible to deposit material onto one sample in each deposition cycle. In contrast to that, multiple samples could be prepared simultaneously with
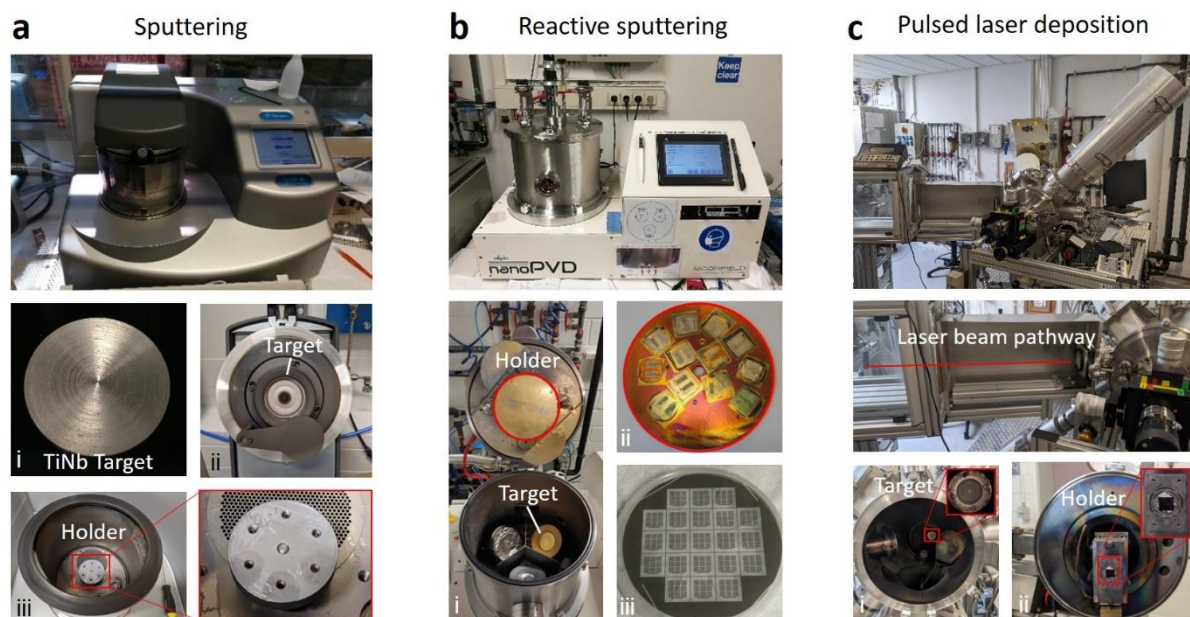
**Figure 4. 2:** Deposition devices. Images of the sputtering (a), reactive sputtering (b) and Pulsed Laser Deposition (PLD) (c) devices used for thin layer production. Ti-45Nb (wt%) target (a-i) inserted in the respective devices (a-ii, b-i, c-i). Sample placement areas for single glass substrates (a-iii, c-ii), multiple substrates (b-ii) and wafers (b-iii).

the reactive sputtering device. In addition, a wafer was introduced into the holder, which allowed the production of 21 samples in each deposition cycle (**Figure 4.2 b-iii**). Two different pathways were utilized in this thesis for obtaining oxidized TS. In the first setting, pure layers were deposited in a non-reactive process (**Figure 4.2 a, c)**, which were subsequently oxidized in an additional thermal oxidation step. In the second setting, the deposition chambers of either the reactive sputtering device (**Figure 4.2 b)** or the PLD device (**Figure 4.2 c)** were filled with an oxygen background, which allowed the direct formation of oxidized films in a reactive deposition process.

## 4.1.2 Lithography fabrication steps

Apart from the deposition methods, two different approaches were used in this thesis in order to fabricate TS in the desired geometry and size. The fabrication is based on photolithography, which was used to pre-pattern the substrate surface with sacrificial layers, that are necessary to initiate the roll-up process (process details are describes in **Section 3.1**). Since a transparent platform should be obtained for cell observation, glass was used as a substrate in all fabrication conditions.

In the first procedure, glass substrates were coated with AR-P photoresist and subsequently exposed in order to obtain the desired pattern (**Figure 4.3 a**). Consequently, the polymer layer was selectively disintegrated with the corresponding developer, which resulted in free-standing photoresists structures. In the next steps, thin layers were deposited and the subsequent removal of the sacrificial layer by DMSO initiated the autonomous roll-up of the pre-strained layers. Furthermore, angled e-beam deposition was used in some cases to selectively accumulate more material at one side of the AR-P structure leading to the formation of a shadow in the opposite position. As less material is located in the shadow, the roll-up process normally starts in this position, which results in an orientated TS rolling.

In the second procedure, glass substrates were coated with AZ photoresist and exposed in an inverse process with a specific pattern in order to obtain "windows" on the substrate surface, which were formed by disintegrating the residual photoresist with the corresponding developer solution (**Figure 4.3 b**). A thin layer of Ge was deposited into the windows and free-standing
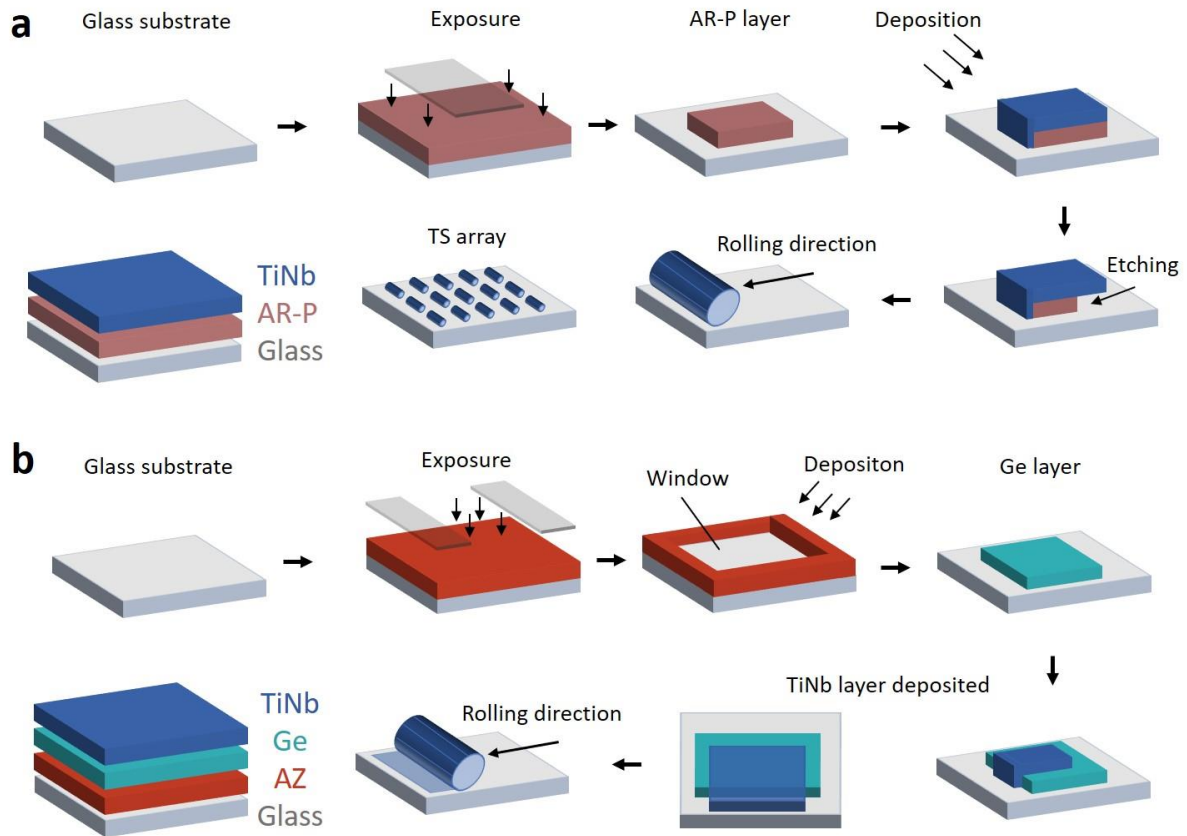


**Figure 4. 3:** Lithography steps for TS fabrication**.** a) Fabrication of a patterned glass substrate by UV exposure of an AR-P sacrificial layer and the subsequent deposition of thin layers followed by etching of the sacrificial layer, which leads to the formation of single TS and TS arrays. b) Patterning of glass substrates with a Ge sacrificial layer by creating windows using an AZ photoresist and the subsequent formation of TS by the deposition of thin TiNb layers onto the Ge-layer, which is followed by a selective Ge etching with $H_2O_2$.

Ge structure, which were used as a sacrificial layer, were acquired after photoresist etching (DMSO). Afterwards, a second window was created, which partly overlapped with the Ge layer and thin layers of TiNb were deposited onto Ge and onto the substrate surface. The TS roll-up was then initiated by etching Ge with an $H_2O_2$ solution. Since the Ge layer is partly covered with TiNb and the corresponding area can't be easily reached by the etching solution, a directed rolling was achieved towards the overlapping area. Furthermore, an advantage of the Ge approach is the possibility to generate a high number of layers by generating additional windows. As a consequence, the inner surface of the TS could be modified with, for instance, electrodes in order to add further functionalities, which is not possible with the AR-P approach.

### 4.1.3 Non-reactive deposition

In this section, the non-reactive deposition techniques are presented, which were used to produce opaque thin layers of the Ti-45Nb (wt%) raw material. After the execution of the roll-up process, these opaque TS were treated with a thermal oxidation step in order to obtain transparent structures for optical microscopy cell analysis. Since the variation of the deposition rate provoked only comparatively low changes of the TS diameter in preliminary experiments, the main focus was lain on the deposition of different layer thicknesses, which are known to influence the layer stress. In addition, it was observed that increasing the layer thickness led to the formation of TS with larger diameters. In order to avoid a high layer thickness of unoxidized Ti-45Nb (wt%) (TN) layers, additional transparent pre-oxidized stress layers (SiO, $SiO_2$, $TiO_2$) were deposited to influence the TS diameter. This is an important factor, as increasing layer thicknesses reduce the changes of a complete material oxidation with thermal processes.

**Figure 4.4 a** depicts TS obtained with AR-P as a sacrificial layer and TN thin layer deposited with sputter deposition. It was possible to acquire arrays of TS by using SiO (5 nm)/$SiO_2$ as basic stress layers and TN (15-30 nm) as the top layer (**Figure 4.4 a-i**). Moreover, tuning the $SiO_2$ layer thickness in between 50-80 nm resulted in TS with diameters in between 26-40 μm. Since the SiO/$SiO_2$ were deposited with an angled deposition process (e-beam), a uniform rolling direction was achieved due to the deposition shadow and the TS possessed a cylindrical shape with only slight aberrations on the side (**Figure 4.4 a-i, red box, white arrow**). In addition, the SiO layer was kept at 5 nm (deposition rate: 5 A/s) for all of the following fabrication conditions and since SiO didn't strongly influence the TS diameter, mainly the $SiO_2$ was changed in order to tune the respective TS diameter. In another approach, TS were obtained
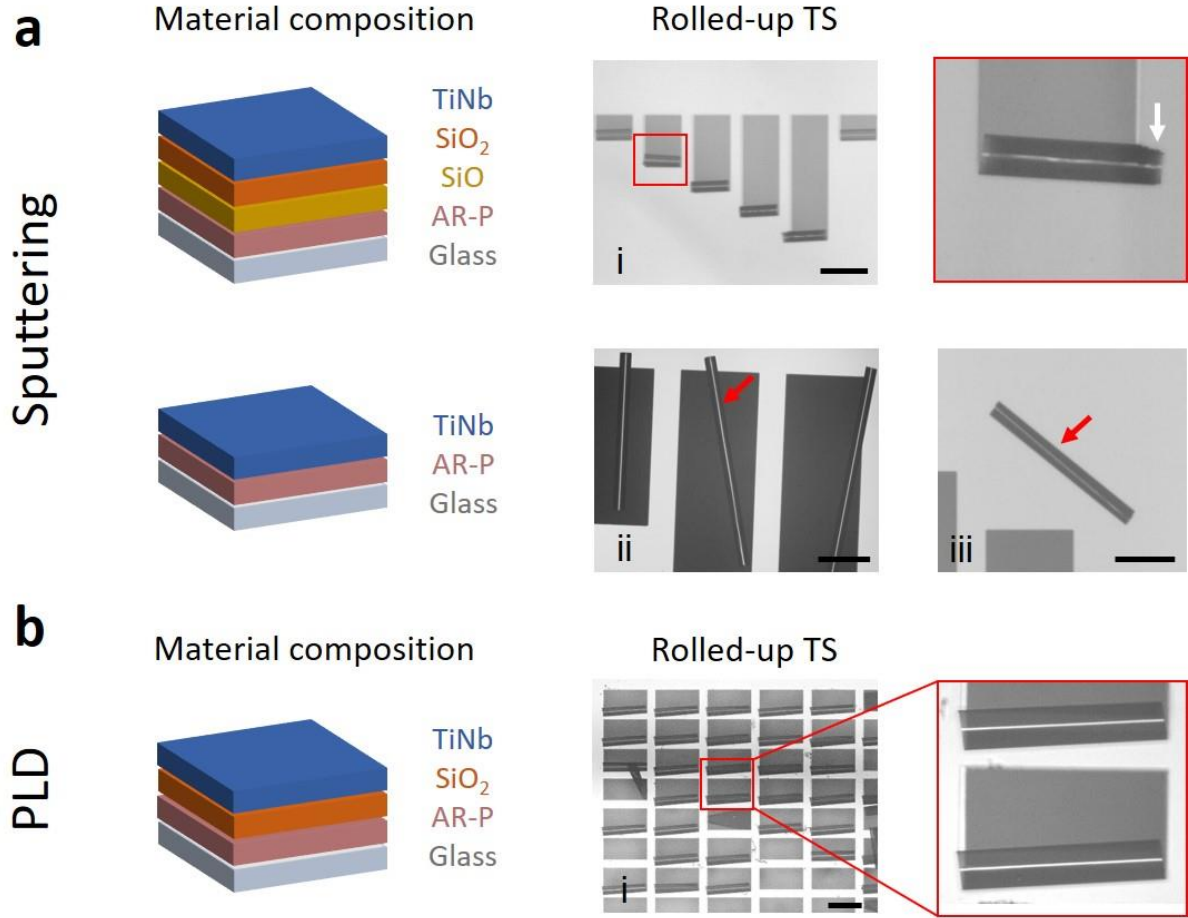
**Figure 4. 4:** TS fabrication with the non-reactive deposition methods and an AR-P sacrificial layer. a) TN-TS fabrication was achieved by using Si-oxides (a-i) and pure TN layers (ii) as strain layers, which partially detached from the surface (ii, iii, red arrow); b) PLD was utilized to form thin TN layers, which led to the formation of TS arrays. Scale bars: a-i: 200 μm, a-ii, iii: 100 μm; b: 200 μm.

by using a single TN layer, which was directly sputtered onto the AR-P sacrificial layer (**Figure 4.4 a-ii**). By tuning the TN layer thickness (15- 70 nm), TS diameters in between 10-26 μm were acquired. However, in contrast to the SiO/SiO$_2$/TN TS, no preference of the rolling direction was observed with TS obtained by a single TN layer, which resulted in a random distribution of the structures on the sample surface. Since the TS were not connected the substrate surface on a specific position, a high number of TS detached from the surface (**Figure 4.4 a-ii, red arrow**) as well as began to float in the etching medium (**Figure 4.4 a-iii, red arrow**). In addition, PLD was used to deposit pure TN layers (20 nm) onto samples pre-patterned with AR-P (**Figure 4.4 b**). Similar to the sputtering approach, oriented rolling was observed on samples prepared with additional SiO and SiO/SiO$_2$ layers. Furthermore, TS arrays were fabricated (**Figure 4.4 b-i**) and modulation of the SiO$_2$ layer thickness (30-70 nm) resulted in TS diameters in between 12-30 μm. Likewise to the sputtered structures, cylindrical shaped TS were acquired in the PLD approach, which depicted a slight tilt at the side of the structure (**Figure 4.4 b-i, red box**).
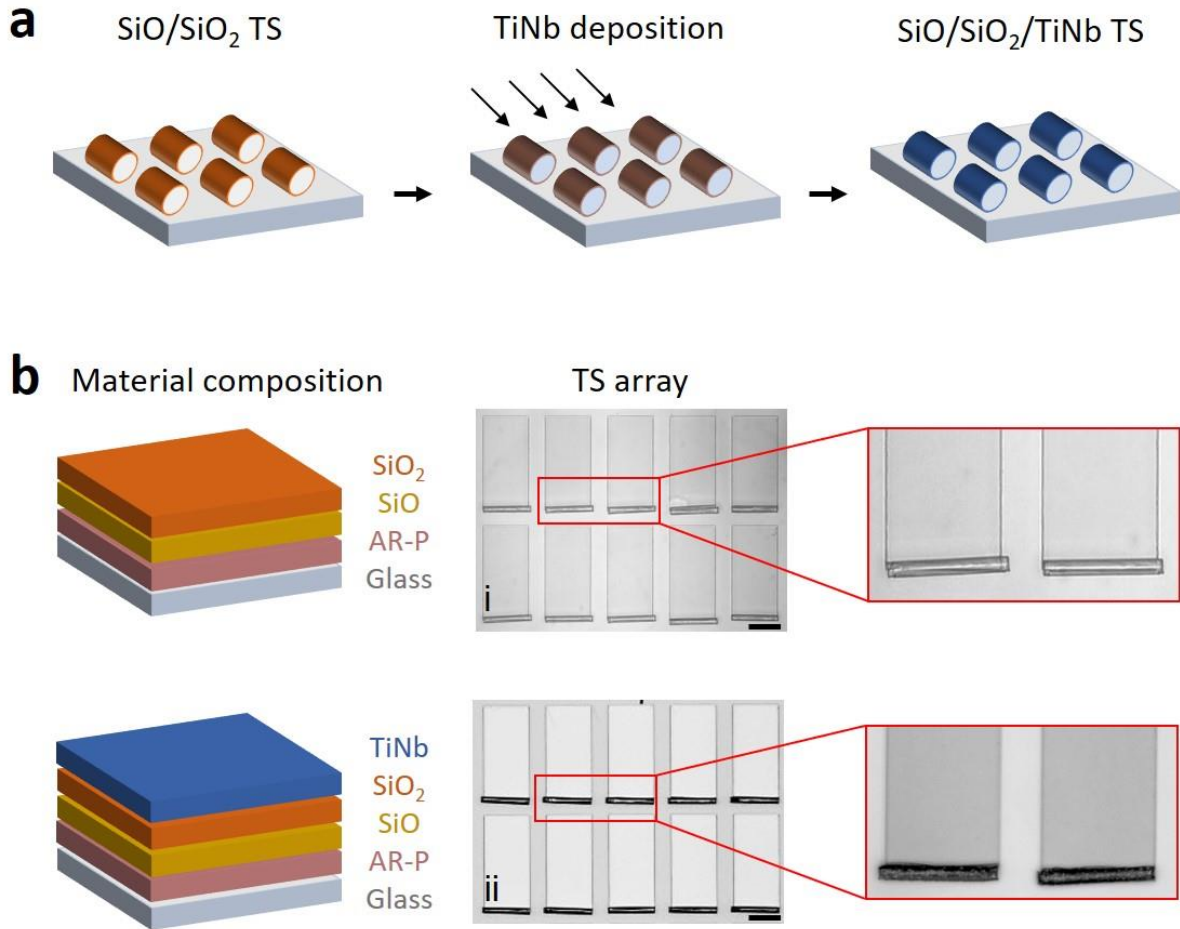
**Figure 4. 5:** TN-TS fabrication with pre-rolled $SiO/O_2$ TS. a) Si-oxide TS were rolled and a thin TN layer (20 nm) was sputtered on their outer hull. b) Images of the microstructures show the TS arrays before (i) and after (ii) the TN deposition. Scale bars: b-i, ii: 100 μm.

All in all, while TS arrays could be fabricated with both sputtering and PLD, the fabrication procedures with additional stress layers (**Figure 4.4 a-i, b-i**) only allowed the production of TS with a TN layer in the structure interior. Unfortunately, no ordered arrays were acquired with a pure TN layer due to the TS detachment (**Figure 4.4 a-ii**). Since the aim of this thesis is to observe the material effect of TN onto the bone cell layer and single cells, TS with an outer and inner TN layer would be preferred, as cells could interact with TN from both sides of the structure in this setting. Consequently, a different approach was used to fabricate TS with a TN shell layer (see **Figure 4.5**). In contrast to the previous procedure, firstly $SiO/SiO_2$ layers were deposited onto an AR-P sacrificial layer and directly rolled-up to form TS arrays (**Figure 4.5 a, b-i**). Subsequently, a TN thin layer was deposited to the outside, which resulted in $SiO/SiO_2/TN$ TS (**Figure 4.5 b-ii**). While this approach has the advantage that the TS diameter can be solely tuned by changing the layer thickness of $SiO_2$, only TS with an outer TN layer were achieved. Consequently, a combination of both production cycles depicted in **Figure 4.4 a-i** and **Figure 4.5** would be desirable in order to fabricate TS for bone cell experiments. Yet, such an approach

could lead to an increased total TN layer thickness, which consequently would complicate the thermal oxidation of the opaque TS.

In addition, Ge was used as a sacrificial layer in order to fabricate TN TS. Therefore, glass substrates were firstly pre-patterned with Ge and a TN layer was subsequently deposited either onto additional stress layers (**Figure 4.6 i, ii**) or directly on top of the sacrificial layer (**Figure 4.6 iii, iv**). Three different fabrication designs were used in the case of sputter deposition which included the TS production with $SiO_2$ and $TiO_2$ as stress layers as well as with a pure TN layer. While TS arrays were obtained in case of the $SiO_2$/TN (**i**) and TN (**iii**) material composition, only few TS were acquired in the setting with $TiO_2$/TN (**ii**). However, a high number of $SiO_2$/TN TS detached from the surface after the roll-up process (**Figure 4.6, red arrow**) and floated in the etching solution. In addition, in a number of instances, an uncompleted roll-up
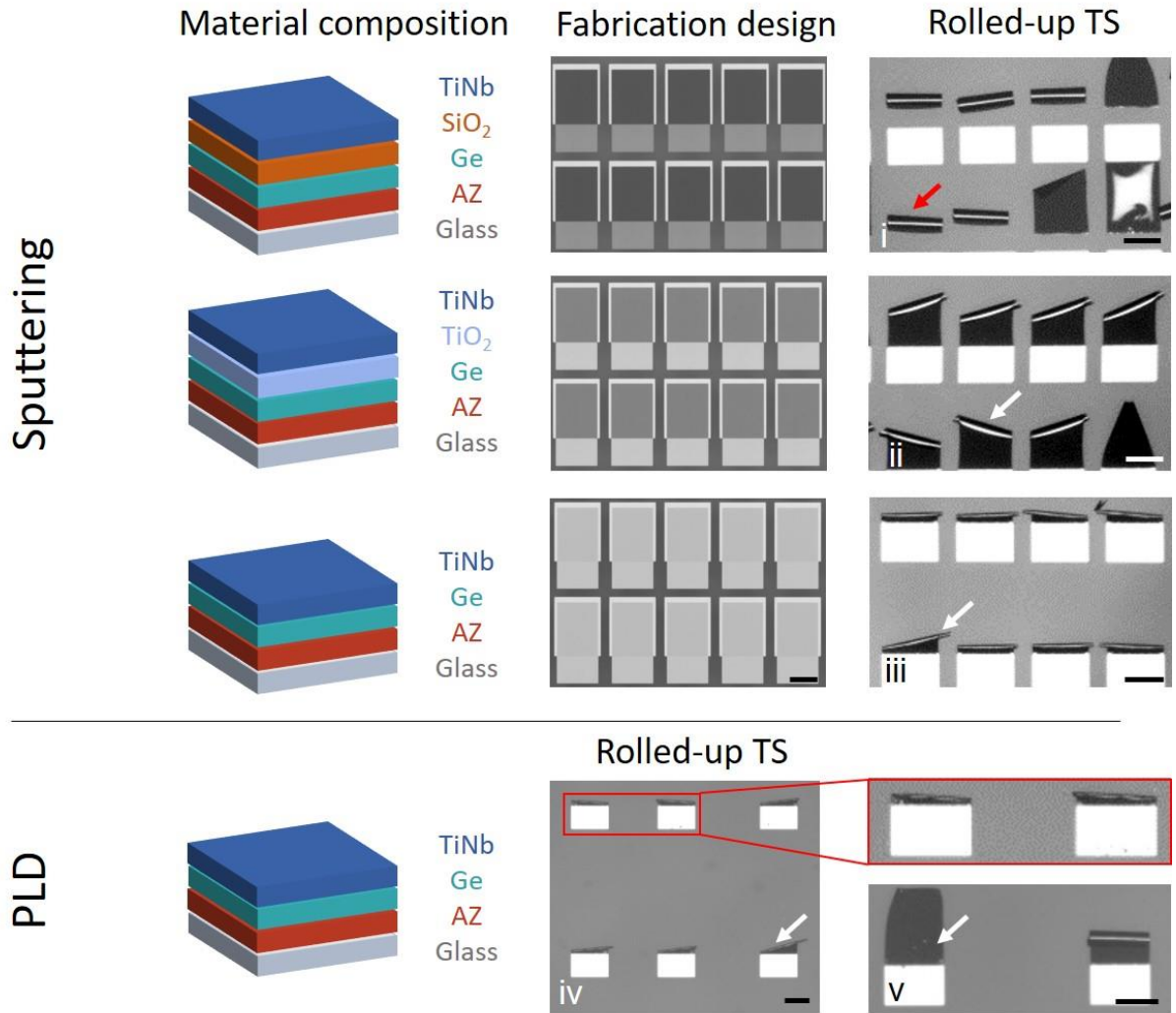


**Figure 4. 6:** TS fabrication with non-reactive deposition methods and a Ge sacrificial layer. The images depict the fabrication of TS arrays with $SO_2$/TN (i), $TiO_2$/TN (ii) and pure TN (iii) layers by using sputter deposition. Different TS diameters were also achieved with PLD (iv, v), yet not all of the TS completely rolled-up (white arrows). Scale bar: 100 μm.

process (**Figure 4.6, white arrow**) was observed and was stronger pronounced in the case of TiO$_2$/TN-TS compared to pure TN-TS. This is likely caused by an insufficient layer strain, which can result, for instance, from a high layer thickness. Overall, the variation of the layer thicknesses by sputter deposition yielded TS with diameters in between 10-38 μm (material composition: SiO$_2$/TN; layer thickness range: 50-70 nm/20-50 nm), 11-22 μm (material composition: TiO$_2$/TN; layer thickness range: 50-70 nm/20-50 nm) and 8-30 μm (material composition: TN; layer thickness range: 30-80 nm). Complementary, TS were fabricated with PLD, which was used to deposit either a single TN layer onto the Ge sacrificial layer (**Figure 4.6 iv, v**) or onto an additional stress layer (SiO/SiO$_2$) (not shown here). After performing the etching process with H$_2$O$_2$, cylindrical shaped TS were acquired (**Figure 4.6 iv, red box**). However, uncompleted roll-up processes similar to the previous sputter samples were observed in this fabrication procedure, which reduced the number of functional TS (**Figure 4.6 iv, white arrows**). Furthermore, the amount of defective TS increased with an increasing TN layer thickness, which could impede the TS rolling (**Figure 4.6 v, white arrows**). All in all, a slightly higher range of TS diameters (11-32 μm) were acquired by alternating the layer thickness of pure TN layers (50-80 nm) compared to TS diameters (6-18 μm) obtained by changing the SiO$_2$ thickness (50-70 nm).

In conclusion, while it was possible to fabricate TS with all of the above-mentioned procedures, the selection of the deposition methods and sacrificial layers (AR-P, Ge) influenced the quality, diameter and amount of obtained TS. In order to compare the different fabrication cycles, all of the used parameters such as the material compositions, the layer thicknesses and depositions devices are summarized in **Table 4.1**. Since the TS were constructed to analyze cell-material interactions, two main criteria have to be fulfilled to obtain a suitable TS platform. Firstly, the TS should possess a diameter in the range of MSC size (12.6-30.4 μm), which is a mandatory condition to study cells inside the TS lumen. Secondly, a high number of ordered TS (array) on the substrate surface is desired, as it enables an analysis of how microtopography affects the cell layer behavior. In the AR-P approach, these objectives were reached by TS fabricated with the material combination SiO/SiO$_2$/TN and PLD, as TS arrays with single TS diameters in the range of the cell size were acquired. In contrast to that, while no TS arrays were obtained in the Ge approach by PLD, a high number of suitable TS were acquired with sputter deposition using the material combinations TN and SiO$_2$/TN, which provided the highest diameter range. Yet, SiO$_2$/TN TS detachment after roll-up lead to a reduction of the TS yield, which might be caused by an insufficient adhesion in between the

**Table 4. 1:** Parameters used for non-reactive deposition TS fabrication.

| Deposition method | TN layer thickness [nm] | Sacrificial layer | Stress layer | Stress layer thickness [nm] | TS diameter range [μm] |
|---|---|---|---|---|---|
| Sputtering | 15-30 | AR-P | $SiO_2$ | 50-80 | 26-40 |
| Sputtering | 15-70 | AR-P | TN | - | 10-26 |
| Sputtering | 20-50 | Ge | $SiO_2$ | 50-70 | 10-38 |
| Sputtering | 20-50 | Ge | $TiO_2$ | 50-70 | 11-22 |
| Sputtering | 30-80 | Ge | TN | - | 8-30 |
| PLD | 20 | AR-P | $SiO_2$ | 30-70 | 12-30 |
| PLD | 20 | Ge | $SiO_2$ | 50-70 | 6-18 |
| PLD | 50-80 | Ge | TN | - | 11-32 |

thin layers and the substrate surface. Furthermore, while transparent pre-rolled $SiO/SiO_2/TN$-TS could be obtained, they only possessed a TN layer on their outer shell, which eliminates the possibility to study cell-implant material interactions inside the TS interior in this case.

Each of the two sacrificial layers AR-P and Ge were adequate to induce the roll-up process, yet the Ge approach offers some advantage. Since the deposited thin layers are in direct contact with the substrate surface in case of the Ge setting, no further angled deposition of additional strain layers is needed for an oriented TS rolling. Consequently, a significantly lower number of fabrication steps are necessary in order to fabricate ordered arrays of TN-TS with Ge compared to, for instance, $SiO_2/TN$-TS prepared with AR-P, for which the usage of an additional deposition device is needed. Another disadvantage of the AR-P approach is the fact that TS fabricated with these layers can't be further modified by additional lithography steps. In conclusion, the results show that both deposition techniques, PLD and sputtering are suitable methods in order to fabricate TS in the desired diameter range. However, all of the earlier produced TS are still opaque and are therefore not yet suitable for observing single cells inside the TS confinement. An optimal deposition setting is therefore depending on the oxidation potential of the respective material compositions and layer thicknesses. In order to achieve transparent TS, a thermal oxidation step is introduced in the next chapter, which is a common technique for material oxidation.

## 4.1.4 Anchor fabrication and thermal oxidation

Like above-mentioned, TS detachment caused a reduction of the TS yield in case of, for instance, $SiO_2$/TN TS fabricated with a Ge sacrificial layer (see **Figure 4.7 a-i**). Since in the case of the Ge approach, further layers can be inserted with additional lithography steps, the TS detachment might be mitigated to some extend with the introduction of an "anchor" system. This anchor should consist of a thick, transparent biocompatible material and cover parts of the strain layers in order to fix them to the substrate. Therefore, a "window" was created at the juncture between the $SiO_2$/TN layer (**Figure 4.7 a-ii**), which is directly connected to the glass substrate and the Ge layer. Subsequently, 100 nm of $TiO_2$ was deposited onto the samples and the residual material was removed in the lift-off process conducted with DMSO, which resulted
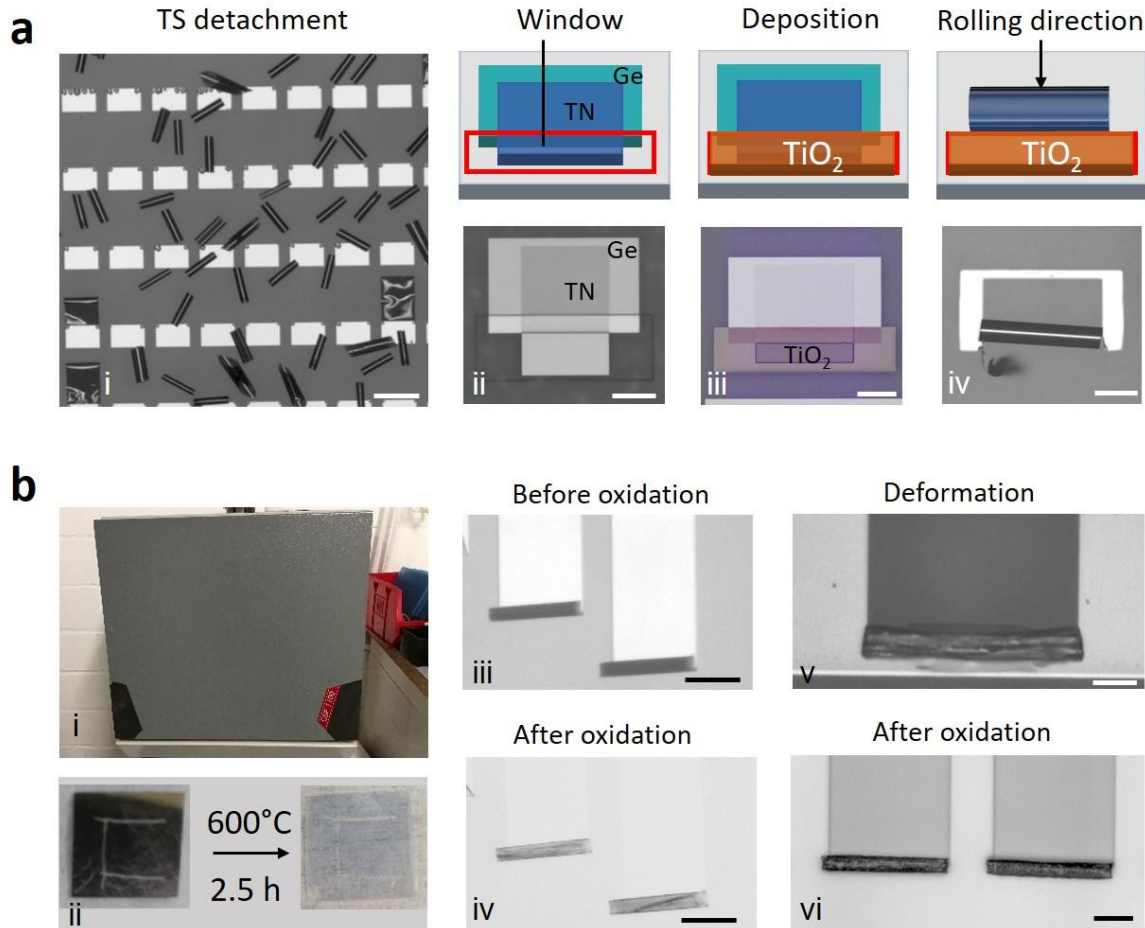


**Figure 4. 7:** TN TS anchor stabilization and thermal oxidation. a) The TS detachment (i) was mitigated by introducing an anchor. A "window" was created (ii), 100 nm $TiO_2$ was deposited (ii) and TS were rolled-up. The anchor stabilized the TS, which remain at the end of its rolling area (iv); b) An oven (i) was used to oxidize thin TN layers (ii) and TN TS (iv-vi). While, a temperature treatment with 300°C, 2.5 h) on TN TS (ii) results in the TS transparency (iii), a temperature treatment on thicker TN layers can cause a structure deformation (iv). TS with an outer TN shell remained opaque (vi). Scale bars: a-i: 200 μm, ii, iii: 100 μm, iv: 50 μm; b-iii, iv: 100 μm, v = 20 μm, vi: 50 μm.

in a large structure positioned above the strain layers and the sacrificial layer (**Figure 4.7 a-iii**). In the next step, the Ge layer was dissolved with $H_2O_2$, which initiated the TS roll-up process by layer strain release. Like displayed in **Figure 4.7 a-iv**, an orientated rolling was achieved, which led to a layer movement towards the anchor structure and the formation of TS. It was observed that the roll-up process was halted at the anchor location and the TS stayed in that position. However, it remained unclear if only the anchor fixed the TS onto the substrate surface or if the residual Ge side structures also prevented a TS detachment. In conclusion, this technique was successfully applied in order to fix TS onto the substrate layer and subsequently facilitates the fabrication of ordered $SiO_2$/TN TS arrays for future applications.

Apart from TS detachment, the optical properties of the previous constructed TS remained a major obstacle for the usage of high-resolution optical microscopy devices. Since all of the above-acquired TS were fabricated with thin layers obtained by non-reactive deposition processes, the TS remained opaque after the roll-up process. Yet, transparent TS are mandatory for analyzing single-cell material interaction inside the TS. This challenge was addressed by treating glass substrates with TS on their surface with a thermal oxidation process. Thermal oxidation is a common technique frequently used on implant materials (e.g. metals) in order to oxidize their surface, which increases, for instance, their corrosion resistance.[299] For example, treating titanium with temperatures above 200 °C results in the formation of a thick oxide layer on the metal surface.[299] Furthermore, Zorn et al. treated a Ti-45Nb (wt%) alloy sample with 600 °C for 1 h and subsequently obtained a TiNb-oxide layer with a thickness of more than 100 nm.[300] An oven was used in this thesis in order to oxidize the opaque TS (**Figure 4.7 b-i**). The thermal oxidation was conducted by placing the TS samples into the oven followed by an upregulation of the internal temperature, which allows the integration of oxygen in the background gas (e.g. air, $O_2$) into the material.[301] Samples were treated for 1-6 h with temperatures in between 200-600 °C, which are typical temperatures used for Ti alloy oxidation.[299] Preliminary tests were conducted with thin TN layers produced by sputter deposition and with an air background in the oven chamber. The obtained data showed that, while a 6 h treatment with 200 °C was insufficient to oxidize a 20 nm TN layer, transparent layers were achieved with process temperatures in between 300-600 °C and a process duration between 1-2.5 h (see **Table 4.2**). A treatment with 600 °C for 2.5 h led to a bending of the glass substrate (**Figure 4.7 b-ii**), which might damage TS arrays on the substrate surface. Thus, the process temperature was restricted to a maximum of 300 °C. In the next approach, $SiO_2$/TN TS fabricated with a 20 nm TN layer were treated with 300°C for 2.5 h (**Figure 4.7 b-iii**). The thermal oxidation process resulted in transparent TS (**Figure 4.7 b-iv**), which furthermore kept

**Table 4. 2:** Thermal oxidation treatment parameters used on TS.

| Temperature [°C] | Process time [h] | Geometry | Layer property |
|---|---|---|---|
| 200 | 2.5 - 6 | Thin film | Opaque |
| 300 | 2.5 | Thin film | Transparent |
| 300 | 2.5 | TS | Transparent |
| 500 | 1 | Thin film | Transparent |
| 600 | 2.5 | Thin film | Transparent |

their original geometry and form. However, TS fabricated with TN layer thicknesses higher than 20 nm remained opaque after treatment with the same process conditions (**Figure 4.7 b-v)** as well as the heating step resulted in deformations of the TS geometry, which increased in magnitude with higher temperatures and longer duration times. In addition, thermal oxidation was performed on SiO/SiO$_2$/TN TS fabricated like described in **Figure 4.5**. In this specific case, a 20 nm TN layer was deposited onto the pre-rolled SiO/SiO$_2$ TS and the samples were treated with 300°C for 2.5 h. The experiment results revealed that, while the thermal oxidation didn't lead to TS deformation, the TS mainly remained opaque (**Figure 4.7 b-vi**). Furthermore, a 100% oxygen background was used in order to oxidize TN TS (data not shown here). Transparent TS were acquired during the heating step and likely due to the high amount of oxygen in the background of the oven. Yet, the procedure also caused deformation of the TS geometry, which reduced the number of functional TS.

In conclusion, while thermal oxidation could be used to oxidize thin layers of TN, an oxidation of rolled-up TS remained challenging. Since the maximum heating temperature had to be limited to 300 °C due to structural deformations and TS with TN layer thicknesses above 20 nm remained opaque with this specific temperature, the production of transparent TS by using thermal oxidation is quite limited. The temperature limitation is a disadvantage, as higher temperature were observed to facilitate the oxidation of Ti alloys and would probably increase the number of transparent TS.[299] Yet, an increase of the process temperature would damage the TS. These restrictions also strongly diminish the possible usage of TS fabricated with non-reactive deposition as a cell analysis platform, as transparency can only be achieved with few material compositions and with TN layer thicknesses up to 20 nm. For instance, since TN layer thicknesses in between 30-80 nm were used for the fabrication of pure TN TS (Ge approach, Figure), it is improbable to acquired transparent TS under these conditions. Consequently, transparent structures can only be obtained with SiO$_2$/TN TS fabricated with sputter deposition (Ge approach, **Figure 4.6 i**) and PLD (AR-P approach, **Figure 4.4 b**). However, since these TS

only possess an internal TN layer, they can only be used to study cell interactions with TN occurring inside the TS, which limits their application range. In order to reduce the number of cell experiments for obtaining reliable data, the TS platform should simultaneously allow the observation of how the microtopography of the TS arrays affects the development of the cell layer, how the material influences the cell behavior and how the spatial constriction inside the TS affects, for instance, the cell morphology and migration behavior. Since it was not possible to oxidize the outer TS shell of pre-rolled TS (see **Figure 4.7 b-vi**), the TS acquired from the non-reactive deposition approach can only be used to party solve the above-mentioned challenges.

### 4.1.5 Reactive deposition

In a second approach, reactive deposition was utilized in order to fabricate thin Ti-45Nb-oxide (wt%) (TNO) layers. Like previously described in **Section 4.1.1** (**Figure 4.1 b, d**), the procedure is conducted by introducing oxygen into the deposition chamber, which allows the oxidation of the raw material during the deposition process. Glass substrates were pre-patterned with Ge and thin TNO layers were prepared with reactive sputtering and PLD. Likewise to the non-reactive sputtering approach, TNO layers were either directly deposited onto the Ge sacrificial layer or on top of an additional $TiO_2$ layer, which was used in order to influence the TS diameter (see **Figure 4.8 a**). In case of the reactive sputtering approach, etching of the Ge sacrificial layer with $H_2O_2$ resulted in cylindrical shaped transparent $TiO_2$ TS (**Figure 4.8 a-i, ii**) and pure TNO-TS (**Figure 4.8 a-iii**). The TS were mostly fabricated with a 30% oxygen background (for the TNO deposition), yet TS could also be fabricated with a 50% oxygen background. However, since an increased oxygen concentration reduces the number of available $Ag^+$-ions in the deposition chamber, which subsequently reduces the deposition rate in case of the reactive sputtering, TNO layer fabrication was focused on the 30% oxygen condition. In contrast to the sputtering approach, while transparent layers were also achieved with reactive PLD (30 % oxygen background), the layer stress was insufficient for a complete TS roll-up process (**Figure 4.8 a-iv, red arrow**). Similar to the non-reactive approach, an increasing layer thickness led to an increased TS diameter. In case of $TiO_2$/TNO-TS (30% oxygen background), diameter ranges in between 8-32 μm were achieved by changing the TNO (20-50 nm) and $TiO_2$ (20-40 nm) layer thicknesses. For instance, while combing a 30 nm TNO layer with a 20 nm $TiO_2$ layer resulted in a TS diameter in between 16-17 μm (**Figure 4.8 a-ii**),

increasing the TiO$_2$ layer to 40 nm resulted in TS in between 26-29 µm (**Figure 4.8 a-i**). In case of pure TNO-TS (30% oxygen background), a diameter range of 10-42 µm was achieved (**Figure 4.8 b**), which is similar to the TiO$_2$/TNO-TS values. Increasing the TNO layer from 40 nm to 50 nm led to an increase in the diameter from 20-23 µm (**Figure 4.8 b-ii**) to 27-30 µm (**Figure 4.8 b-iii**). In spite of changing the layer thickness, all fabricated TS remained transparent and it was possible to fabricate large arrays of TNO-TS (**Figure 4.8 c-i**) and TiO$_2$/TNO-TS. These structures exhibited a uniform cylindrical shape along the x-axis (**Figure 4.8 c-ii**) and they possessed a spherical shaped tube opening (**Figure 4.8 c-iii**), which would allow a cell migration into the TS interior. Furthermore, the usage of the Ge-approach led to an oriented rolling, which resulted in a maximum yield of 67% of well rolled-up structures in case of the pure TNO-TS.
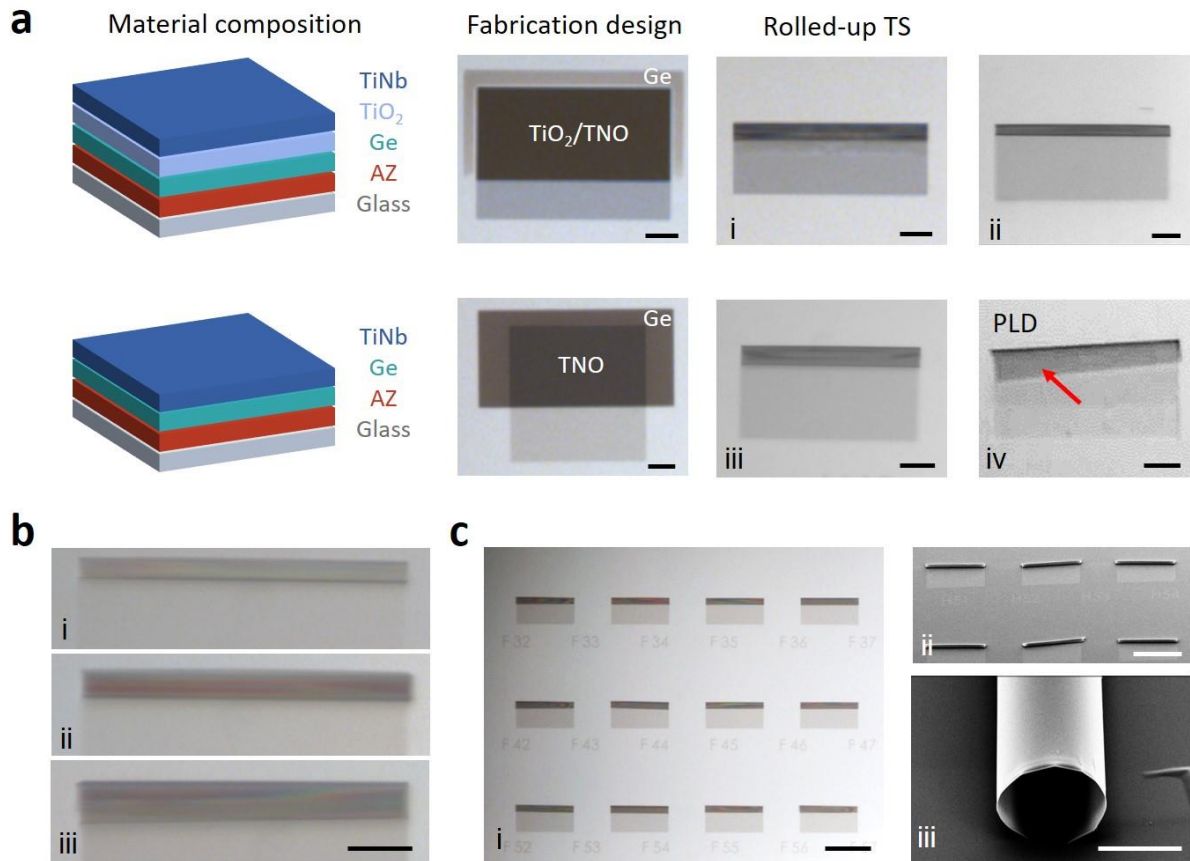


**Figure 4. 8:** TNO TS formation with reactive deposition methods. a) TS were formed with TiO$_2$/TNO strain layers (i, ii) and pure TNO layers (iii) by using Ge as a sacrificial layer and reactive sputtering. Transparent TNO layers were also deposited using reactive PLD (iv), yet no TS were acquired due to insufficient stress (red arrow). b) TS with different diameters (12-30 µm) were obtained by changing the TNO layer thickness (i-iii). c) Full arrays of TS with a uniform geometry were fabricated (i), which was confirmed by SEM (ii). The TS displayed roundly shaped openings (iii). Scale bars: a, b: 50 µm; c-i, ii: 200 µm, iii = 10 µm. Figure modified from reference.[302]

In conclusion, it was possible to produce transparent TS in a suitable diameter range for cell experiments by using reactive sputtering. Similar diameters were acquired with and without a $TiO_2$ strain layer and TS arrays were achieved with both material configurations. However, since the $TiO_2$ layers were deposited with another device (e-beam), less steps are required in order to fabricate pure TNO-TS. In contrast to the $TiO_2$/TNO-TS, pure TNO-TS also possess a TNO layer as an internal layer and a shell, which allows the simultanious study of single cell-material interactions inside the TS and cell layer interactions with the TNO-TS array. Consequently, pure TNO-TS are the preferred fabrication product. Moreover, the outer TNO shell is an advantage compared to the non-reactive strategy, in which it was not possible to generate TS with a TNO shell. Compared to the non-reactive deposition appraoch, TNO-TS arrays can be constructed with a much lower amount of fabrication steps, as only one sputtering device is necessary in order to deposit the required transparent layers. Since no TS detachment was observed in the reactive deposition setting and transparent layers were directely obtained during deposition, no furthermore process steps such as a thermal oxidation treatment or a fabrication of an anchor are needed. Thicker layers of TNO also remained transparent, which facilitates the production of different TS diameters and allows an observation of cell-implant material interactions inside the TS with optical microscopy. Moreover, like displayed in **Figure 4.2 b-iii**, the reactive sputtering device can be used to fabricate up to 21 glass samples (wafer design) at a time, which is in stark contrast to only 1 sample per deposition cycle in case of non-reactive sputtering and PLD. Since a higher number of control samples are normally needed when conducting cell experiments, the mass fabrication capacitiy of the reactive sputtering device is another advantage of the reactive sputtering method compared to the other devices. In summary, reactive sputtering offers an easy way to produce high amounts of pure TNO-TS with tunable diameters, which makes it superior to the above-displayed non-reactive approach. The subsequent material analysis is therefore mainly focused on TNO layers obtained by reactive sputtering in order to identify their material composition.

### 4.1.6 Glass tubular microscaffolds

Beside the production of TNO-TS, glass TS were fabricated as control samples for cell experiments. Therefore, SiO (5 nm layer thickess)/$SiO_2$ strain layers were deposited onto an
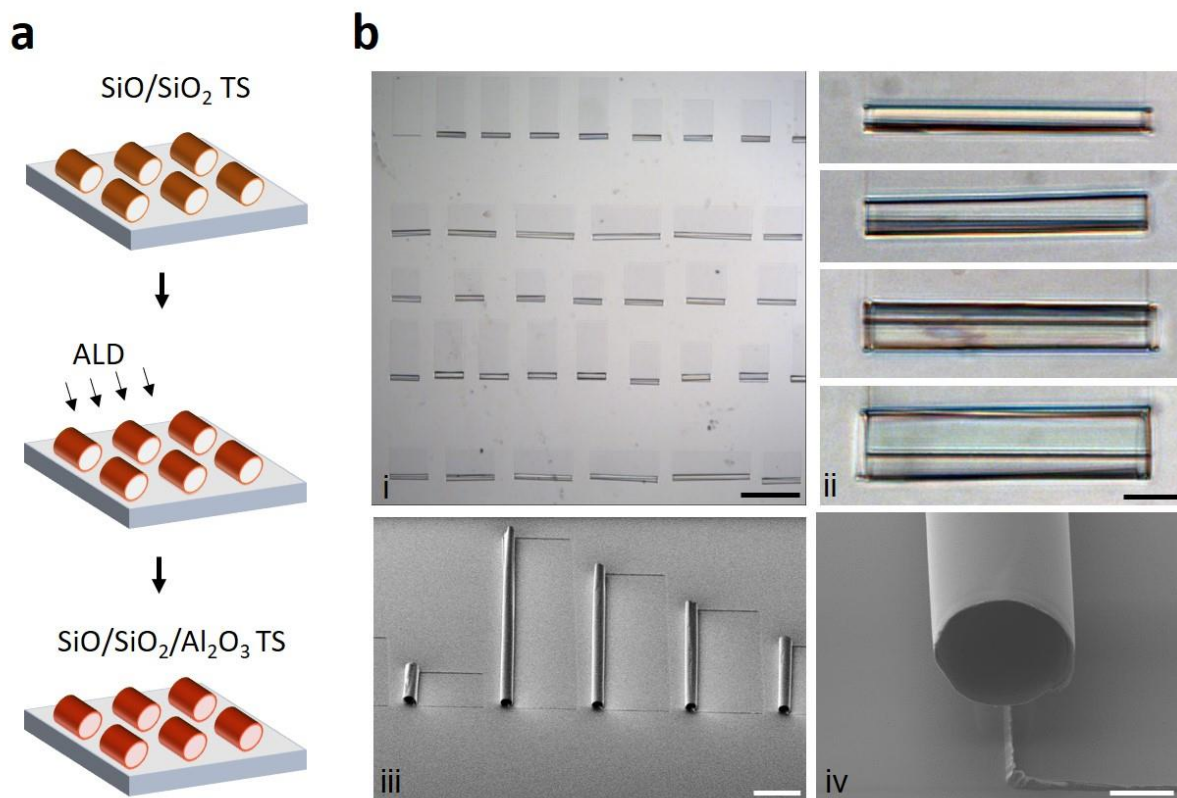
**Figure 4. 9:** SOA TS fabrication. Arrays of SiO/SiO$_2$/Al$_2$O$_3$ (SOA) TS were fabricated with different lengths (i) and diameters (ii). A uniform tubular geometry (iii) and roundly shaped TS openings (iv) were confirmed by SEM imaging. Scale bars: i, ii: 50 µm, iii: 100 µm, iv: 10 µm. Figure modified from reference.[302]

AR-P sacrificial and the roll-up process was initiated by removing the photoresist. In order to stabilize the TS further, a Al$_2$O$_3$ layer (20 nm) was deposited onto the TS shell (**Figure 4.9 a**). Like depicted in **Figure 4.9 b-i**, large arrays of SOA-TS with different lengths were acquired after etching (**Figure 4.9 i**). By tuning the SO$_2$ layer thickness in between 50-100 nm, TS with different diameter in the range of 10-50 µm were obtained (**Figure 4.9 ii**). The TS diameter range is therefore sufficient for cell experiments and comparable to the ones acquired with TNO-TS. Furthermore, the cylindrical geometry was confirmed by SEM imaging showing fully rolled-up TS with a circular tube entrance likewise to TNO-TS (**Figure 4.9 iii, iv**). Since SiO/SiO$_2$/Al$_2$O$_3$ (SOA) TS possess a distinct material composition compared to TNO-TS, these TS can be used to detect changes in the cell behavior caused by differences in their material chemistry and surface properties.

## 4.2 Material characterization

The following section addresses surface and material composition studies conducted on the above fabricated thin films for TS production. A detailed knowledge of the surface properties facilitates the evaluation of cell-material interactions, as bone cells react to surface characteristics such as the nano-, micro-roughness and the surface chemistry, among others. Furthermore, since this study is aimed to closely transfer the material composition of the raw implant material Ti-45Nb (wt %) onto the TS platform, possible compositional changes caused by the particular deposition methods have to be analyzed and evaluated. Subsequently, XPS, XRD and TEM studies were performed to analyze the chemical and crystalline state of TNO thin layers (**Section 4.2.1**). The surface properties of all fabricated thin layers (TNO and SOA) were characterized by AFM and contact angle measurements (**Section 4.2.2**).

### 4.2.1 Ti-45Nb (wt %) layer characterization

Like depicted in **Section 4.1**, it was possible to fabricate TS by using different deposition strategies. Since the elemental composition of a material can influence cell reactions, it is important to analyze the elemental distribution of Ti and Nb after the deposition process. Thin layers of Ti-45Nb (wt%) were therefore deposited onto glass substrates with sputtering, reactive sputtering and PLD using the same deposition parameter like shown above. The composition of the layers was subsequently analyzed in order to evaluate, which device delivers an optimal material transfer. The layer properties were compared to a polished Ti-45Nb (wt%) bulk sample, which was used as a reference. The material analysis was performed with XPS (for experiment details see **Section 3.2.3**), which is a commonly used material characterization technique based on the photoelectric effect.[303,304] In short, a beam of x-rays is focused on the material and the photon energy is subsequently absorbed by electrons of the raw material, which leads to the emission of the affected electron.[303] The material properties are then deducted from the kinetic energy of the photoemitted electrons, which depends on the bound state of the specific element and its' chemical environment and the amount of the respective element is deducted from the number of measured electrons.[304,305] Furthermore, XPS measurements can be combined with a sputtering device, with which depth profiles of the material can be acquired.[303] The results from the XPS measurement are displayed in **Table 4.3**, which depicts the atomic ratio of Ti and Nb at the layer surface and inside the layers (sputter equilibrium). It

**Table 4. 3: Elemental ratios of thin Ti/Nb layers obtained with XPS**

| Sample and fabrication method | Ti/Nb atomic ratio (surface) | Ti/Nb atomic ratio (sputter equilibrium) |
|---|---|---|
| $Ti_{70}Nb_{30}$ (at%) reference (bulk target) | 70/30 | 70/30 |
| $Ti_{70}Nb_{30}$ (at%) sputtering | 82/18 | 76/24 |
| $Ti_{70}Nb_{30}$ (at%) sputtering + thermal oxidation | 84/16 | 78/22 |
| $Ti_{70}Nb_{30}$ (at%) reactive sputtering 30% $O_2$ | 64/36 | 56/44 |
| $Ti_{70}Nb_{30}$ (at%) reactive sputtering 50% $O_2$ | 64/36 | 56/44 |
| $Ti_{70}Nb_{30}$ (at%) PLD 30% $O_2$ | 85/15 | 70/30 |

was observed that the atomic concentration of Ti was increased on the surface of all deposited layers, which resulted in a decreased Nb concentration compared to the reference sample ($Ti_{70}Nb_{30}$ (atomic content %, at%)). The ratios obtained from reactive sputtering ($Ti_{64}Nb_{36}$ (at%)) were close to the properties from the original material, which is in contrast to the elemental distribution acquired from the thermal oxidation process ($Ti_{84}Nb_{16}$ (at%)) and PLD ($Ti_{85}Nb_{15}$ (at%)). In addition, a sputtering process was used in order to analyze the Ti/Nb ratio inside the layers. It was observed that, while the nominal elemental content in the bulk target was maintained during the procedure, the amount of Ti was reduced in the sputter equilibrium on all deposited thin layers. Consequently, the Ti/Nb ratio obtained from PLD ($Ti_{70}Nb_{30}$ (at%), equilibrium) matched the reference composition in this setting as well as the values acquired from oxidized layers ($Ti_{78}Nb_{22}$ (at%)) were closer to the bulk target ratios compared to the layer deposited by reactive sputtering ($Ti_{56}Nb_{44}$ (at%)). However, it is known that the $Ar^+$ ion bombardment of the sputtering process can lead to a shifting of the elemental concentration and provoke changes of the respective oxide states.[136,291] The binding energies of Ti and Nb of each sputtering step were therefore analyzed by using a $Ti_{70}Nb_{30}$ (at%) layer deposited with reactive sputtering (30% $O_2$). It was observed that sputtering led to a reduction of the Ti and Nb-oxides to lower valence states. All in all, since it remains unclear if the ratio acquired in the sputter equilibrium reflects the actual material composition of the bulk material, the surface values were considered as the main criterion for the elemental distribution. Further material characterization studies were therefore conducted on layers obtained with reactive sputter deposition (30%), since the Ti/Nb atomic ratios (surface) acquired for these layers closely matched the reference values.
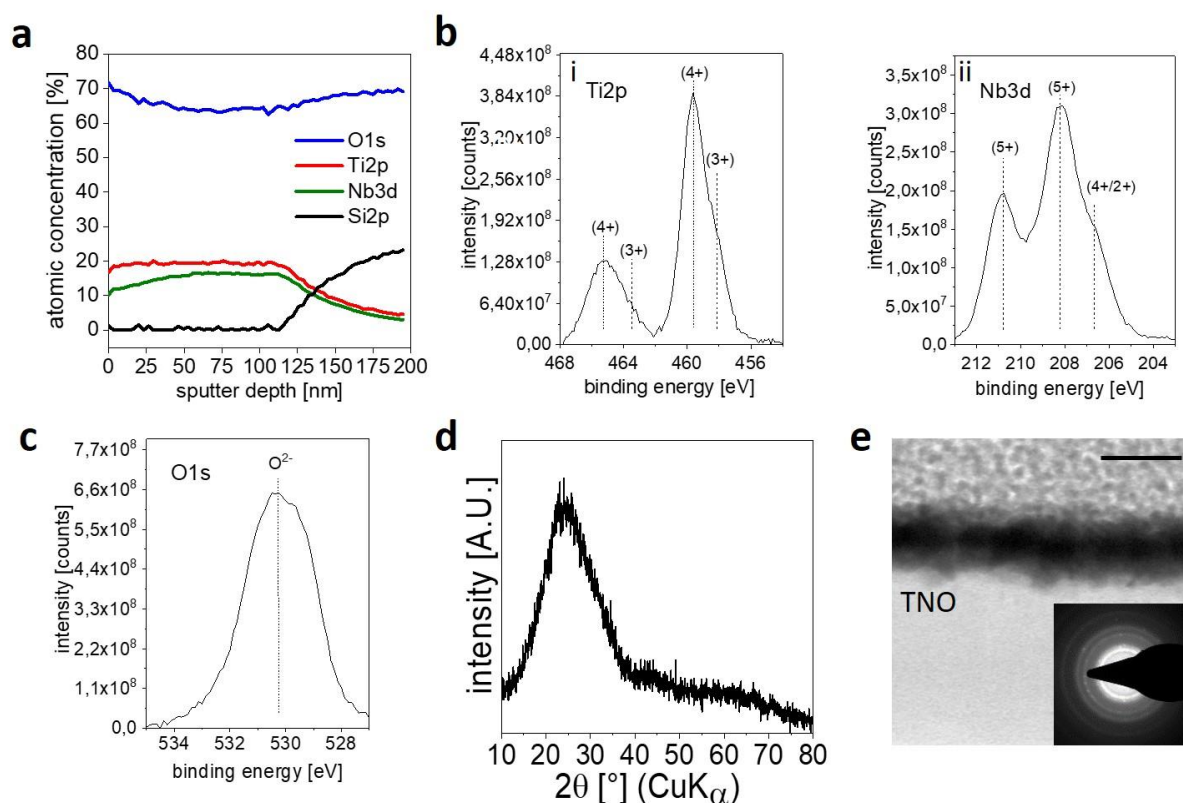
**Figure 4. 10:** TNO layer characterization. a) A high oxygen amount was found all through the TNO layer thickness with XPS sputter depth profiling. Core level spectra of the b) Ti2p (i), Nb3d (ii) and c) O1s states taken from the non-sputtered layer surface. d) XRD spectrum shows amorphous state of TNO layer. e) TEM/SAED analysis confirms the homogeneous amorphous state of the deposited TNO thin layer (reactive sputtering, 30% $O_2$) as no crystal reflexes were visible. Scale bar: 20 nm. Figure modified from reference.[302]

Additional XPS measurements were conducted on 110 nm thick TiNb-oxide layers (reactive sputtering, 30% $O_2$, referred to as TNO) in order to analyze, if the thin layers are oxidized throughout the whole layer thickness as well as if the Ti and Nb contents remained constant inside the deposited layer. The results in **Figure 4.10 a** exhibit a very high oxygen concentration, which was maintained during the whole stepwise $Ar^+$ ion sputtering process duration. Moreover, the Ti2p and Nb3d concentrations stayed constant after the initial surface layer was sputtered and a certain sputter equilibrium was reached. Subsequently, the core level spectra of Ti2p and Nb3d of the TNO layer were analyzed in more detail. In case of Ti2p, two main peaks at 459.6 eV and at 465.2 eV (**Figure 4.10 b-i**) were detected, which can be related to the $Ti^{4+}$ state of $TiO_2$ and the slight asymmetry of the peaks hints to a sub-stoichiometric $Ti^{3+}$ state. In case of Nb, two peaks were located at 208.2 eV and 210.8 eV, which correspond to the $Nb^{5+}$ state of stoichiometric $Nb_2O_5$ and a shoulder observed at 206.6 eV implies the existence of sub-stoichiometric oxides with a $Nb^{(4+/2+)}$ state (**Figure 4.10 b-ii**). In addition, no metallic

state ($Nb^{(0)}$) was found in the Nb3d spectra. The $O^{2-}$ state of oxygen was verified as the related main peak was observed in the O1s spectra at 530.3 eV (**Figure 4.10 c**).

Furthermore, thin layers of TNO (reactive sputtering, 30% $O_2$) were deposited onto glass substrates and analyzed by using grazing incidence XRD measurements in order to study the structural state of the layer. A broad diffuse halo was thereby observed, which is characteristic for a highly disordered amorphous state and in line with the lack of a crystalline oxide phase in the XRD pattern (**Figure 4.10 d**). Moreover, a TEM lamella was prepared out of a 35-40 nm TNO layer with Focused Ion Beam (FIB) in order to check its' structural state. The TEM brightfield image (**Figure 4.10 e**) shows the TNO layer covered by a Pt conductive layer. Besides the diffuse halos, which are indicative for an amorphous oxide phase, only weak nanocrystalline reflections were observed in the subsequent Selected Area Electron Diffraction (SAED) pattern (inset in **Figure 4.10 e**), which might be caused by the deposited Pt layer. Scanning Transmission Electron Microscope (STEM) analyses were conducted in order to determine the elemental ratio of Ti and Nb atoms in the deposited layers. Compared to the nominal element content of the bulk target ($Ti_{70}Nb_{30}$ (at.%)), a slightly higher concentration of Nb atoms ($35 \pm 2$ at.% ) was detected in the thin oxidized layer, which implies a higher transfer rate of Nb during the deposition process. Accordingly, the concentration of Ti was lower with $65 \pm 2$ at%. All in all, the data obtained from the TNO layer characterization indicates towards the presence of mixed Ti- and Nb-oxides in the deposited layers. This is in line with previous studies showing that Ti and Nb can form various mixed oxide states, which can be described with the formula $(Ti_xNb_{1-x})O_2$.[306] In addition, shoulders were observed in the core spectra, which indicate towards additional sub-stoichiometric oxides in the strain layers and the here reported oxide states are similar to states observed in earlier studies conducted on $Ti_{70}Nb_{30}$ (at%) bulk scaffolds, whose surfaces were oxidized by anodization.[136,291,307] XPS analysis conducted on thin $Ti_{70}Nb_{30}$ (at.%) layers showed that the respective deposition methods strongly influences the Ti/Nb ratio of the deposited film. The ratios obtained by reactive sputtering ($Ti_{64}Nb_{36}$ (at.%), non-sputtered surface value) were closer to the reference material ratio compared to the values acquired by the other approaches. This device is therefore the preferred method for further TNO layer deposition. In addition, a STEM analysis was conducted on these layers, which resulted in Ti/Nb ratios that closely matched the XPS data as well as suggested the presence of a $(Ti_{0.65}Nb_{0.35})O_2$ compound.[306] However, the Ti/Nb ratio shifted towards higher Nb concentrations when reaching the sputter equilibrium ($Ti_{0.46}Nb_{0.35}$ (at.%)), which could indicate towards the formation of sub-oxides caused by the $Ar^+$ ion bombardment.[291,308] Since the amounts of Ti- and Nb-oxides could vary along the cross-section

of the deposited films, the exact oxide phase composition remains unclear. The deposited layers are therefore considered as amorphous TNO, which mainly consist of $(Ti_xNb_{1-x})O_2$ (x range 0.65 to 0.5) and with minor fractions of sub-stoichiometric oxides. Since the reactive sputtering (30% $O_2$) approach allowed a close transfer of the elemental composition from the $Ti_{70}Nb_{30}$ (at.%) bulk scaffold to thin transparent layers, subsequent material characterization were conducted with these layers as well as TS were fabricated out of TNO layers (reactive sputtering, 30% $O_2$) for the following cell experiments.

## 4.2.2 Surface characterization

Beside the material composition, the surface topography and nano roughness play an important role in directing, for instance, the cell adhesion and migration behavior. In order to analyze the material characterization, TNO layers (reactive sputtering, 30% $O_2$ background) and SOA layers were deposited onto glass substrates. The surface properties of the thin films (TNO, SOA) were characterized by Atomic Force Microcopy (AFM) in order to study the surface roughness (Root Mean Square = RMS) as well as by contact angle measurements conducted by using DI water to assess the surface wettability. In order to estimate the influence of the fabrication process, 2D samples, in which SOA and TNO layers were directly deposited onto cleaned glass pieces (2D samples) and samples with TS on the surface (3D samples) were fabricated. This procedure is necessary since the samples were treated with photoresist developer solutions and organic solutions (acetone, isopropanol; details in the experimental section) during the 3D sample preparation, which might influence their properties. In order to analyze the influence of the deposited layers, all of the samples were compared to basic untreated glass samples.

The results from the AFM analysis depict a distribution of nano-sized hikes and pits on the glass samples, the 2D samples and on TNO-3D samples in between the TS (**Figure 4.11**). Moreover, he material deposition only led to small changes of the surface roughness. While a slight RMS reduction was observed on SOA-2D samples (0.62 nm ± 0.3 nm) and TNO-3D samples (0.551 nm ± 0.09 nm) compared to pure glass (0.68 nm ± 0.10 nm), a slight increase was detected on TNO-2D samples (0.96 nm ± 0.008 nm) samples. In contrast to that, higher amounts of nano-sized hikes were detected on the surface of SOA-3D samples and on the inner
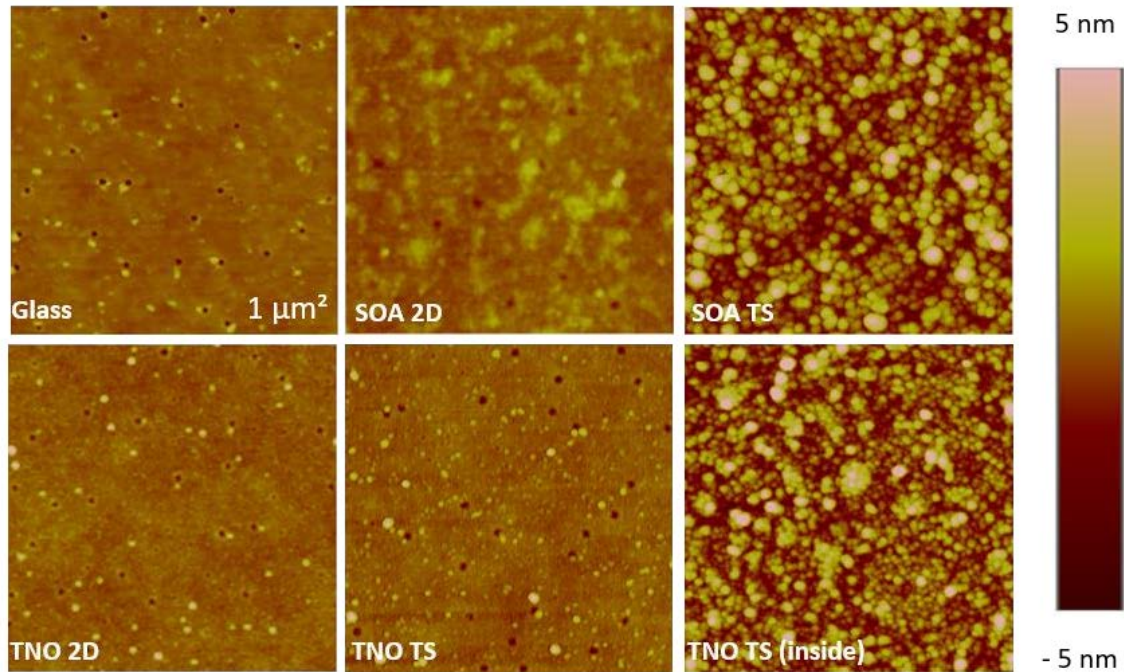
**Figure 4. 11:** AFM measurements of glass, SOA and TNO samples. The material deposition causes only small differences in the surface roughness compared to glass. The RMS increased as well as the formation of hikes can be found on the SOA TS samples and inside TNO-TS structures. All image areas: 1μm². Figure modified from reference.[302]

walls of TNO-TS 3D structures. A strong increase of the surface roughness was observed for SOA 3D samples (1.97 nm ± 0.74 nm) and inside the TS on TNO-3D (1.41 nm ± 0.13 nm) compared to the other settings. All RMS values determined by the AFM analysis are summarized in **Table 4.4**.

**Table 4. 4: AFM RMS values for glass, SOA and TNO samples**

| Sample | RMS values (1 μm²) |
|---|---|
| Glass | 0.68 nm ± 0.10 nm |
| SOA-2D | 0.62 nm ± 0.38 nm |
| SOA-3D | 1.97 nm ± 0.74 nm |
| TNO-2D | 0.96 nm ± 0.08 nm |
| TNO-3D | 0.51 nm ± 0.09 nm |
| TNO-3D (inside TS) | 1.41 nm ± 0.13 nm |

Furthermore, contact angle measurements (**Figure 4.12**) revealed lower contact angles for the TNO samples (40°-70°) compared to their SOA counterparts (75°-90°). In both cases, lower contact angles were observed on the 3D samples, which implies that the fabrication process and the TS have indeed an impact on the sample wettability, as otherwise the same layer thicknesses and substrates were utilized for both settings. Thus, it can be assumed that the above-mentioned etching steps by isopropanol or hydrogen peroxide influenced the chemical state of the materials as both 3D samples depicted a higher hydrophilicity. Additionally, the contact angles of the depicted TNO layers lied in in the optimal range for protein adsorption (40°-70°).[309] This might therefore improve the biological response on these layers compared to SOA layers, as extracellular matrix proteins present in the surrounding medium could adhere in the right amount and conformation on the TNO layers.[309] Beside wettability, surface nano-roughness also plays a vital role in protein and cell adhesion processes. However, as only small deviations between the deposits and the glass substrates were detected, large effects based on surface roughness effects are unlikely. Merely, the slightly higher RMS-values and widespread hikes on the sample surface of SOA-3D samples and inside TNO-3D TS might influence cell adhesion to a minor extent. All in all, transparent TS constructed from reactive sputtering can be considered as an adequate tool for studying cell-implant interactions *in vitro*.
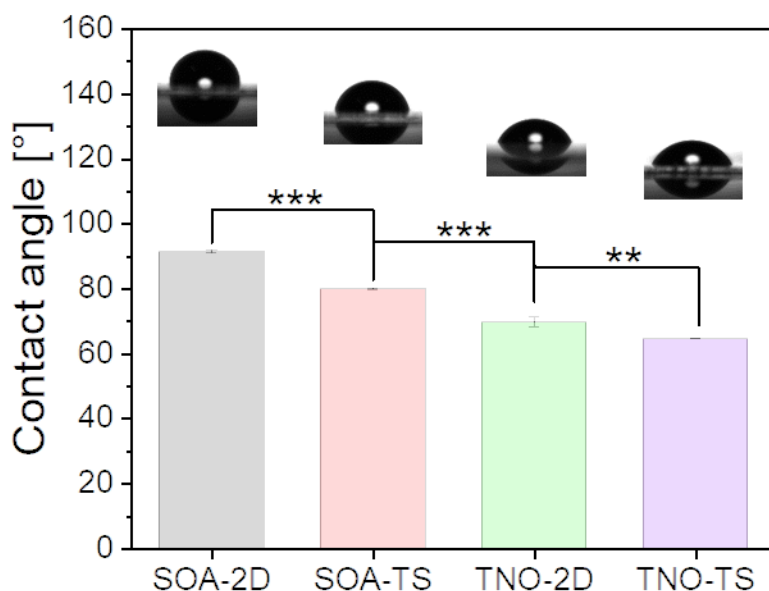


**Figure 4. 12:** Contact angle measurements of TNO and SOA layers. Pure water drops are deposited on sample surfaces respectively and contact angles are compared: SOA-2D and TS, TNO-2D and TS. Mean values ± SD of 3 distinct TS samples (n=3, * $p < 0.1$, ** $p < 0.05$, *** $p < 0.01$), respectively. Figure modified from reference.[302]

## 4.3 Initial cell experiments

This section describes first cell studies, which were performed with human Mesenchymal Stem Cells (MSC) in contact to TS produced out of TNO and SOA thin layers. Therefore, TNO-2D (without TS) and SOA-2D (without TS) samples are compared to TNO-TS and SOA-TS samples in order to assess how the cell adhesion, proliferation and survival is influenced by factors such as the fabrication process, material type and the micropatterning of the TS arrays. Moreover, these studies should clarify if the TS are stable under cell conditions and if the experiments can be maintained for at least three weeks, which is the time duration for cell differentiation and initial bone mineralization processes.

### 4.3.1 Cell proliferation and adhesion studies

In order to analyze the proliferation potential depending on the material type, MSC were seeded onto TNO, SOA samples and plastic cell culture plates (Tissue Culture Polystyrene (TCPS)), which functioned as a control. The proliferation assay was performed with a 3-(4,5-dimethylthiazol-2-yl)-5-(3-carboxymethoxyphenyl)-2-(4-sulfophenyl)-2H-tetrazolium) (MTS) assay, which measures the metabolic activity of cells by the amount of formed formazan (**Figure 4.13 a**). The proliferation was measured after 24, 48 and 72 hours on all samples, respectively. A slightly higher proliferation rate was observed on 2D samples compared to their 3D counterparts in the initial phase after 24h, whereas the highest metabolic activity was measured on TCPS. The cell proliferation rate strongly increased on the 3D samples until TNO-TS exhibited the highest metabolic activity after 72h. Compared to the planar samples, the cell number increased by 16.7 % on TNO-TS and 36.6 % on SOA-TS, which indicates towards an influence of the material properties onto the cell growth. Especially the hydrophilic state of TNO layers and their high Nb content could have led to an improved protein adsorption and thereby provoke higher cell adhesion and proliferation rates compared to the other conditions. Material type dependent cell spreading was subsequently analyzed using the same samples settings like described above (**Figure 4.13 b**). Only slight differences of the cell spreading area were observed on the planar samples (SOA-2D, TNO-2D, TCPS), and they depicted average values around 5000 µm². In contrast to that, a significantly lower cell spreading area was detected inside TS, whereas TNO-TS and SOA-TS possessed a similar spreading area with maximum values of 800 µm². This shrinkage of the cell area is likely caused by confinement
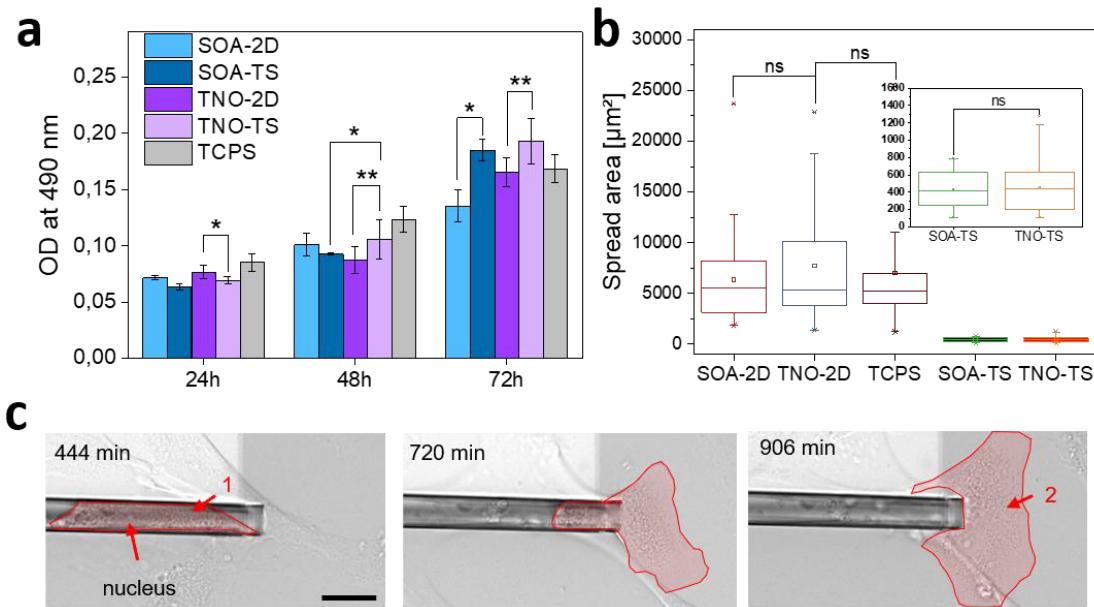
**Figure 4. 13:** Cell proliferation and cell morphology changes inside TS. a) MTS assay showing in average a constant increase of the cell number on all the evaluated materials: TNO, SOA and tissue culture polystyrene (TCPS), mean values ± SD correspond to triplicate experiments (n=3, * p<0.1, ** p<0.05, *** p<0.01) with more than 200 TS per individual TS sample. b) Cell spreading area on planar and TS samples obtained by measuring the spread area of 50 cells from 3 distinct experiment samples (n=3, p>0.1 (ns)), respectively. c) Morphology changes and a stepwise increase of the spreading area of the hMSCs were observed when the cell moved out of the TS (inside microscaffold: 1; outside microscaffold: 2). Scale bar: 25 μm. Figure modified from reference.[302]

dependent effects inside the TS, which restrict a free cell spreading in the lateral direction. Furthermore, cells attached to the TS walls inside the TS interior, which is depicted in **Figure 4.13 c**. While the cell initially possessed an elongated cell shape inside the TS (time point 444 min), migration out of the TS provoked a gradual morphology change until a wide spread cell shape was reached outside of the TS (time point 906), which is typical for cells in 2D environments. Furthermore, cells interacted with the outer surface of the TS (**Figure 4.14 a-i**), recognized TS from a distance with their cell extensions (**1**) and subsequently moved the whole cell body towards the TS (**2**). The cell aligned to the TS walls (**3**), moved on top of the structure (**4**) and migrated to the other TS side (**5**). Cell attachment to the TS was also confirmed with SEM images (**Figure 4.14 a-ii**), in which parts of the cell was attached to the side and top of the TS (**red box**).

In order to obtain more information about the cell attachment behavior, immunofluorescence staining was conducted. The cytoskeleton (actin filaments) was labeled with phalloidin (green), vinculin, a component of focal adhesion complexes, was labeled with anti-vinculin/Alexa 568 (red) and the cell nucleus with DAPI (blue). This procedure allowed the visualization of attachment points as yellow-orange signals, in which the actin and vinculin signals merged. The
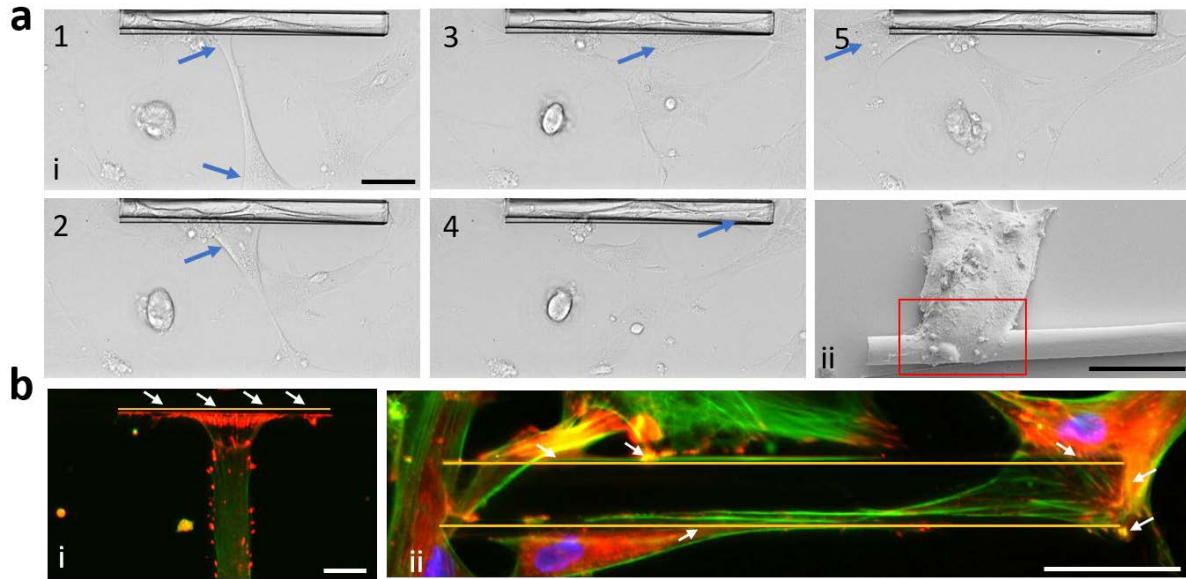
**Figure 4. 14:** Cells interacting with single TNO-TS. a) Cell migrate towards the TS and attach to it (1-5). SEM image showing multiple cells attaching to TS side (ii). b) Fluorescence images (vinculin (red), actin (green), cell nucleus (blue) show cell attachment to the TS (i) and cell alignment (ii) along the TS wall with multiple FA (white arrows). Scale bars: a, b: 50 µm. Figure modified from reference.[302]

positions of these focal adhesion points further represent strong cell interactions with the surrounding environment. As seen in **Figure 4.14 b-i**, cell interaction with the TS wall invoked a large orange signal (white arrows), which implies a strong attachment to the TS. Furthermore, various sizes of focal adhesion points were observed from several cells around the TS (**Figure 4.14 b-ii**). While small FA were distributed around the TS, which were probably caused by cell alignment along the TS walls, very large signals were detected at edges and the entrance of TS. Cells might be confronted with a larger contact area in these positions as single cells could attach their bodies to the outer and the inner TS part at the same time, which could be responsible for the stronger fluorescence signal.

## 4.3.2 1h vs 24h cell adhesion

The cell attachment on planar surfaces of TNO and SOA samples was further analyzed by comparing the cell attachment 1h and 24h after cell seeding (**Figure 4.15**). Cells exhibited round shapes with small spreading areas on both materials after 1h. The actin and vinculin contents were mostly equally distributed while a slightly higher vinculin amount was concentrated around the cell nucleus as well as no signs of an actin stress fiber formation were observed. In the merged images, yellow-orange signals were mostly found close to the cell core
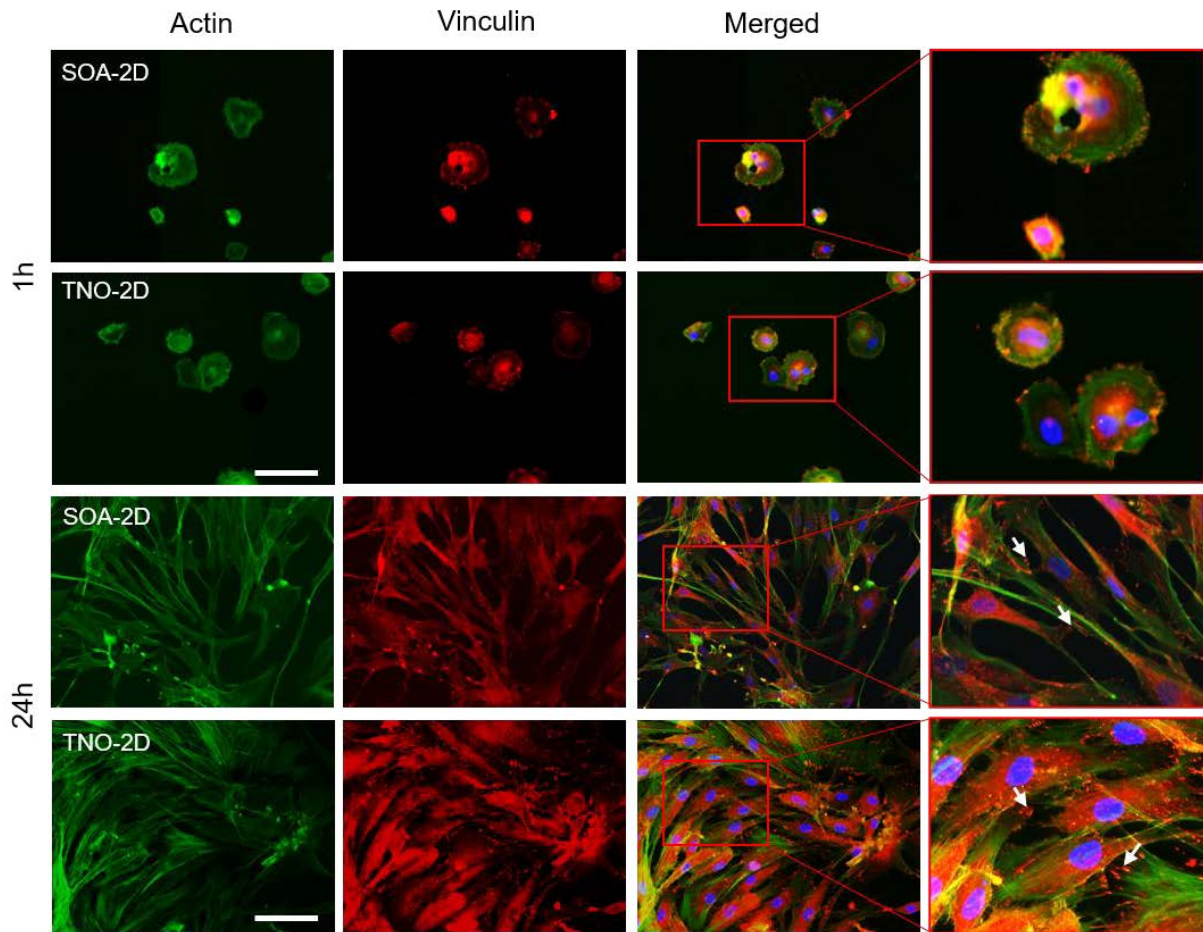
**Figure 4. 15:** Fluorescence staining on planar substrates. hMSCs adhesion on planar sample surfaces stained with immunofluorescence dyes (vinculin (red), actin (green), cell nucleus (blue)) 1 h after cell seeding. Cells depict a more roundly morphology with small focal adhesion points at the rim as well as a small spreading area. hMSCs 24 h after cell seeding formed focal adhesion points and stress fibers on SOA and TNO samples (white arrows). The cell adhered to the surface and enlarged their spreading size. Scale bar: 50 μm. Figure modified from reference.[302]

and small needle-shaped Focal Adhesion (FA) points were visible at the cell body rim regions, which indicates towards a beginning cell-surface attachment. In contrast to that, cells were full spread and exhibited a typical spindle-like cell shape after 24h. Furthermore, stress fibers were formed alongside the long side of the cell bodies. While a higher part of the vinculin content was concentrated around the cell nucleus, FA were formed and distributed all over the cell body, especially at the end of actin filaments. By comparing the materials, more prominent FA were found on TNO samples, which indicates towards a stronger cell attachment and a higher osteogenic differentiation potential on this material.

## 4.3.3 Cell adhesion and migration inside tubular microscaffolds

In order to obtain more information about how TS confinement influences the cell attachment behavior and cell morphology, fluorescence images were taken from cells in TS. Like depicted in **Figure 4.16 a**, a small part of the cell was located inside the TS during the entering process, while the main cell body with the cell nucleus was still positioned at the entrance of the TS, which resulted in a strong merged signal in that position. Only few small FA (**white arrows**) were formed by the cells inside the TS in most cases, which were mainly distributed around the cell bodies (**Figure 4.16 b-i**). Furthermore, the actin and vinculin contents were mostly overlapping similar to the cell state after 1h and no large actin fibers were present inside the TS. However, larger FA were observed in situations when cell "scanned" the inner TS walls with their cell extensions and subsequently attached to several different positions at the same time (**Figure 4.16 b-ii**). The different attachment behaviors might result from multiple forms of migration modes available inside the confined environment. Like depicted in **Figure 4.17**, cells utilized two separate migration modes inside the TS. The cells either elongated their cell extensions, attached to multiple points of the TS wall and moved slowly to the end position (**Figure 17 a-i, b**) or strongly attached to a specific point, which was followed by a rapid cell movement to that specific position, in which the cell assumed a round shape (**Figure 4.17 a-ii**).
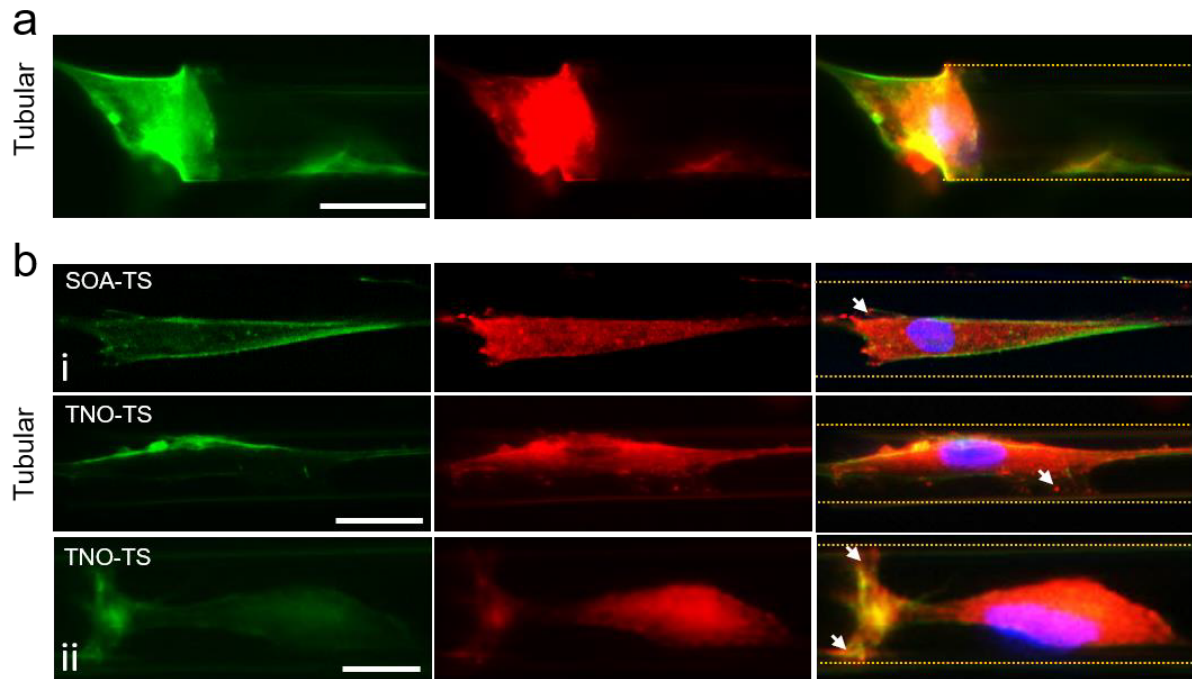


**Figure 4. 16:** Cell adhesion inside TS. a) Fluorescence imaging shows a cell entering the TS. b) Cell adhesion inside TNO-TS and SOA-TS samples (i, ii). Cell extensions adhere to the TS wall (focal adhesion points (white arrows)) (ii). Scale bars: a: 25 μm; b-i: 25 μm, b-ii: 10 μm. Figure modified from reference.[302]

Furthermore, a higher number of contact points were formed inside the TNO-TS compared to their SOA-TS counterparts as well as long dendritic-like cell protrusions with lengths longer than 100 µm were formed inside the TS, which scanned the inner parts of the TS and attached to several positions of the TS wall (**Figure 4.17 c, blue arrows**). Cell-cell contact was also established inside the TS by cell extensions, which might attract other cells towards the TS cavity.
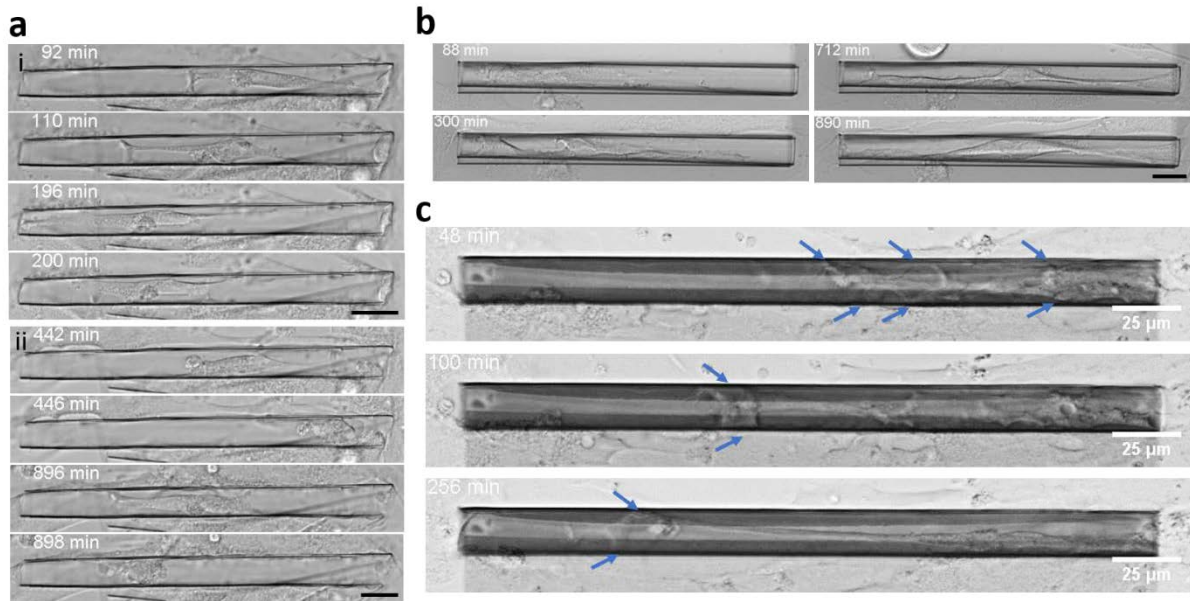


**Figure 4. 17:** Cell migration inside TS. Cells utilize two types of migration modes inside SOA-TS (a) and TNO-TS (b). The cells either moved slowly and elongated (a-i, b) or fast with a pull movement (a-ii). c) Cell scans the TS walls with long dendritic like extensions (blue arrows). Scale bars: 25 µm. Figure modified from reference.[302]

## 4.3.4 TS effect on cell attachment and migration

The here presented results demonstrated that TS were mechanically stable inside the cell culture conditions and the TNO-TS transparency was sufficient to allow live observation of cell migration inside the TS as well as immunofluorescence imaging. Both fabricated TS settings (SOA, TNO) allowed cell adhesion and spreading leading to increasing cell numbers within 72h. In addition, effects of the material type were observed as the proliferation rate and the amounts of focal adhesion complexes were increased on TNO samples compared to their SOA counterparts, which is in line with the results from the earlier material characterization results (**Section 4.2**). Furthermore, a direct effect of the TS was observed as the cell morphology as well as the adhesion and migration behavior differed strongly inside the TS interior compared to 2D surfaces. This might be attributed to confinement effects, which led to reduced sizes of

cellular focal complexes and might be the reason for the observed change in between different migration modes. The here reported results are in line with a study by Doolin et al., which showed that human MSC can migrate through microchannels with a width from 50 μm down to 3 μm.[266] The constriction led to a reduction of the actin fiber network, which appeared diffuse and less fibrillar in small channels (3 μm).[266] In addition, Holle et al. studied the influence of microchannels with widths between 3-10 μm onto the migration behavior of breast cancer cells.[267] They reported a switch from the mesenchymal to the amoeboid migration mode in small channels (3 μm) and a usage of both modes in channels with a width of 10 μm.[267] The spatial confinement also led to an increase of the migration velocity, the formation of large cell protrusions (> 100 μm), a decrease of mature focal adhesions. Cells also exhibited blebbing in those narrow channels, which is comparable to the cell behavior observed in TS.[267]

Moreover, as stated in the fundamental section (**Section 2.7**), 3D constricted environments might allow an integrin-free migration, which would explain the lack of large focal adhesion complexes inside the TS. As only a low roughness of the thin layers was observed in the AFM studies, TS could favor a chimneying migration mode similar to artificial microchannels.[84] Like depicted above, cells formed multiple contact points with the TS walls, which could lead to intracellular pressure gradients as well as friction forces between the cell body and the TS walls. Both effects could explain the observed cell movement inside the TS without the need of large focal adhesion complexes. It could be further speculated that the migration mode is depending on the dimension ratio between cell size and TS diameter. TS with small diameter could facilitate a tight contact between the cell body and the TS walls as well as an increasing cell sizes, which is related to the passage number.[48] Thus, depending on the particular dimension ratio, middle-sized cells might use both migration modes inside the TS, while larger or smaller cells might be restricted either to the focal adhesion based migration mode or to chimneying.

The change of migration mode might also be explained by curvature effects provided by the geometry of the TS. A study conducted by Werner et al., analyzed the curvature effects on human MSC cells by using arrays of concave and convex cylindrical structures with widths in between 250-1000 μm.[277] They observed that the migration persistence was lower on concave cylindrical surfaces compared to convex surfaces as well as the migration speed was higher on concave surfaces.[277] This was caused by lifting the cell body off the substrate leading to a reduction of the contact area with the substrate to distinct adhesion points, which allowed a faster remodeling of the focal adhesions and the cytoskeleton as well as provoked significant morphology changes.[277] A further influence of curvature onto the migration mode was observed in a study with spherical concave structures, in which cells used a two-phase extend-and-pull

movement.[276] This type of migration was initiate by the formation of long cell protrusions and a subsequent adhesion to a specific point on the substrate. This was followed by a pull leading to a fast movement of the cell body towards the adhesion point.[276] Additionally, Pieuchot et al. reported that MSC respond to cues provided by curved structures with a diameter close to the cell size.[310] Cells were observed to migrate into concave areas in order to position their nucleus close to the topological minimum, which led to more spherical nuclei shapes caused by a mechanical relaxation of the cell core.[310] Since similar changes of the migration behavior and cell shapes were observed inside TS, it might be assumed that the curvature of the TS walls is another important environmental factor, which influences cells inside small pores.

In conclusion, while this study demonstrates that TS strongly affected MSC migration and adhesion compared to 2D surfaces, further detailed studies with, for instance, TS with various diameters are necessary in order to determine the dominant factor responsible for the exhibited cell adhesion and migration behavior.

## 4.4 Cell differentiation and cell layer development

This section is focused on osteogenic differentiation experiments, which were conducted in order to verify if the cell layer development, the cell viability and differentiation potential is influenced by TS arrays on the sample surface. Furthermore, the TS platform was used to analyze the single cell differentiation inside the TS, which resemble micropores in porous bulk implants. In order to analyze the influence of the TS and the material choice (TNO, SOA) on the osteogenic cell differentiation of human MSC, TNAP activity and qPCR analysis were performed with TCPS as a control. The qPCR analysis, for instance, can be used to identify markers of osteogenesis (e.g. collagen expression), which indicate towards a MSC differentiation into osteoblast progenitor cells. In parallel, the cell layer development over time was visualized via optical microscopy and the cell viability was checked with a live/dead staining. An optical analysis of the cell layer growth during osteogenic differentiation provides additional information about the differentiation state of the layer, which is indicated by, for instance, the formation of mineralized nodules on the substrate surface.[311] Furthermore, surface patternings are known to affect the cell alignment and the extracellular matrix orientation, which can lead to changes of the tissue formation in the macro scale.[312] Consequently, optical images can be used to analyze the impact of micro/nano structures and the substrate curvature (provided by the TS array) onto the cell layer behavior (e.g. attachment, layer shape).[312,313] In

order to observe cell layer changes caused by the differentiation process, the samples were either immersed in Differentiation Medium (DM) in order to stimulate the osteogenic differentiation or in Standard cell culture Medium (SM), which subsequently functioned as control samples.

## 4.4.1 TNAP activity

The TNAP activity was measured at day 9, 11, 13 and 15 after the differentiation was initiated (**Figure 4.18**). A significantly higher TNAP activity was found on all materials (TNO, SOA,
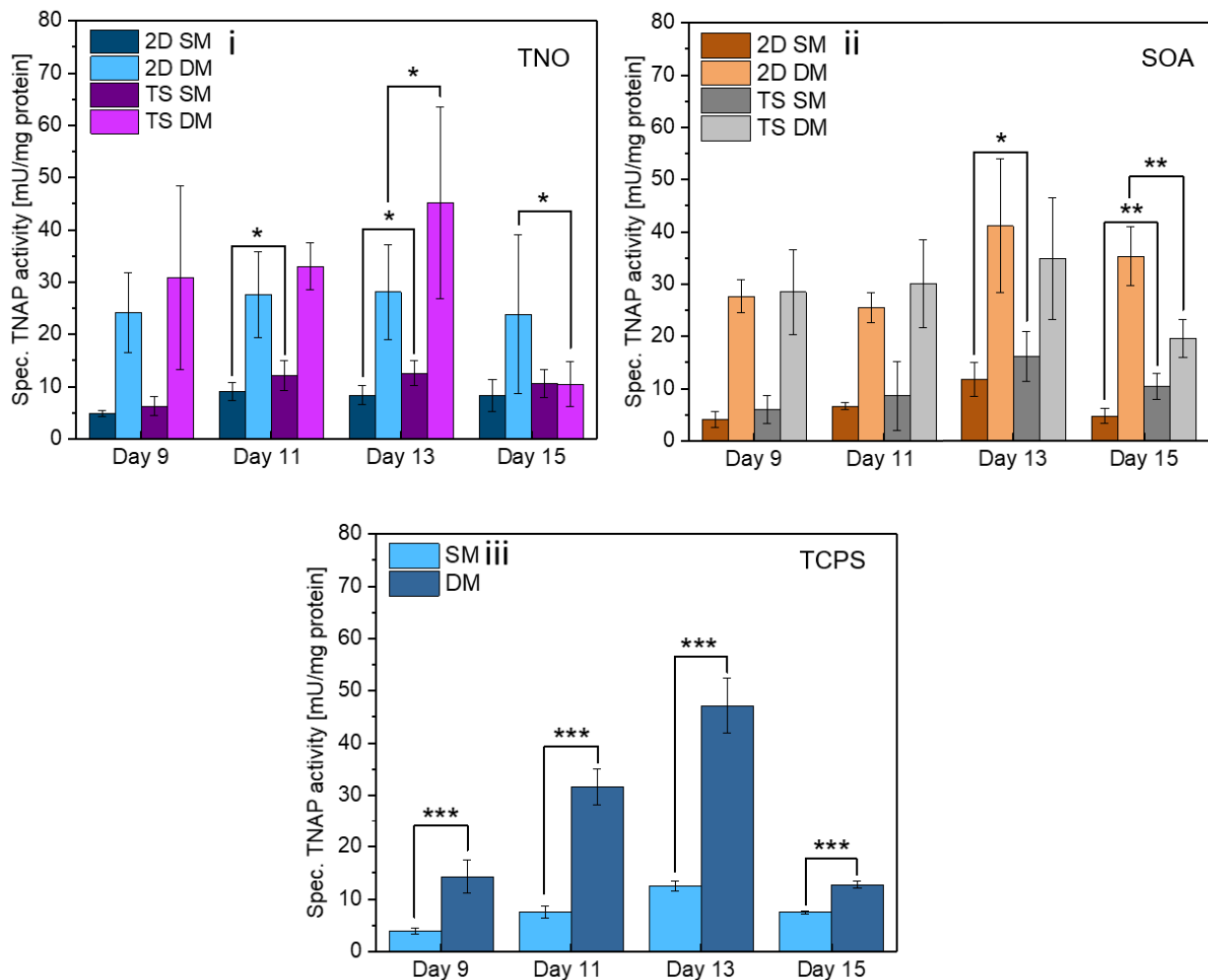


**Figure 4. 18:** Osteogenic differentiation capability of hMSC evaluated with TNO, SOA and TCPS samples. TNAP activity (related to the total protein concentration) of hMSCs seeded onto TNO (i), SOA (ii) and TCPS (iii) samples immersed in SM and DM after day 9, 11, 13 and 15. A higher TNAP activity was observed in samples with differentiation medium (DM) compared to the samples with standard medium (SM) (n=3, * p<0.1, ** p<0.05, *** p<0.01). Figure modified from reference.[302]

TCPS) in DM compared to SM between day 9 and 13. The TNAP activity increased until day 13, where an activity maximum was reached followed by a decline until day 15. The TNAP activity saturation was observed for all samples independent of their material composition and might be caused by a TNAP inhibition due to increased phosphate levels at day 13.[314] Furthermore, the TNAP activity was stronger pronounced in all SM samples with TS compared to their planar counterpart, which hints to a osteogenic effect caused by the TS themselves or by effects from the sample preparation procedure. While the general increase of TNAP values on TNO and SOA samples might be explained by a material-induced osteogenic effects, increasing TNAP activity values were also observed in the TCPS SM samples. These values might originate from already existing pre-osteoblast in the initial seeding culture as the cells used in this study were extracted from the bone marrow, in which cells in different states of the differentiation process exist next to each other. Furthermore, higher values for the TNAP activity were measured at day 9 and day 11 on TNO and SOA samples compared to the TCPS control, which indicates to a material dependent effect on the osteogenic cell differentiation by the deposited materials in the early phase of osteogenesis.

## 4.4.2 ELISA and qPCR analysis

Complementary to the TNAP activity measurements, ELISA and qPCR assays were conducted at day 11 after the change to DM. Factors such as hTNAP, hCol(I)$\alpha_1$, hCol(I)$\alpha_2$, hOPG and hRANKL, which are typically expressed during the early phases of osteogenic differentiation were analyzed. Likewise, to the TNAP activity assay, TNO-2D, TNO-3D, SOA-2D and SOA-3D samples were fabricated and compared to TCPS control samples. **Figure 4.19 i** shows the results of the TNAP gene expression. Similar to the TNAP activity assay, the TNAP gene expression at day 11 was upregulated in DM compared to their SM counterparts and TNO DM as well as SOA DM samples possessed higher expression levels than TCPS samples. Furthermore, higher gene expression levels were observed in 2D samples compared to their 3D counterparts, which is in contrast to the previous results. In summary, the material dependent increase of the TNAP gene expression by SOA and TNO samples was similar to the results from the TNAP-activity. Regarding the difference of 2D and 3D samples, one could speculate that other factors in the cell surroundings could inhibit the protein productions in case of the 2D sample, which would explain the higher TNAP-activity in the TS experiment setting.
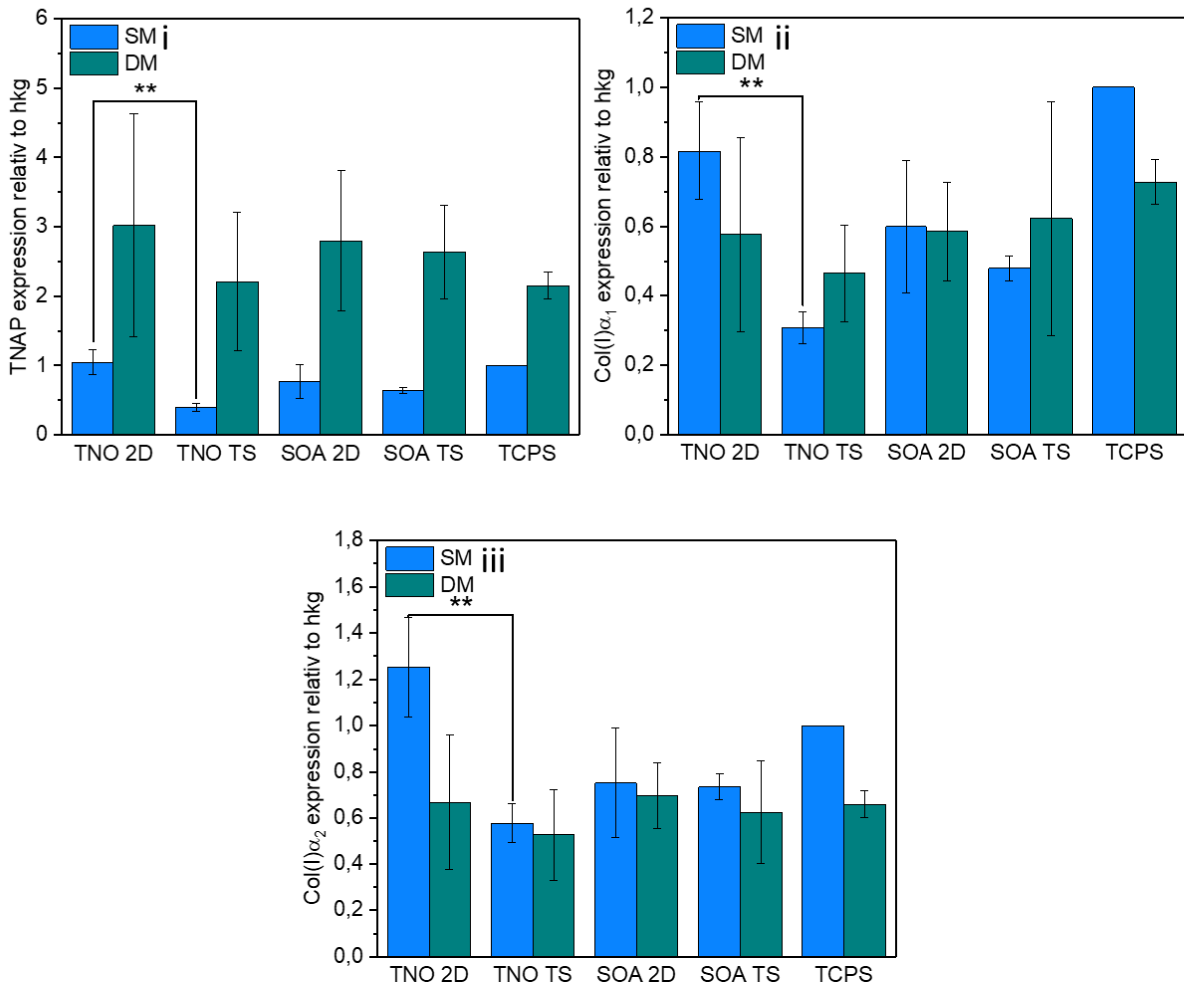
**Figure 4. 19:** Osteogenic differentiation capability of hMSC evaluated with TNO, SOA and TCPS samples. TNAP, Col(I)$\alpha_1$ and Col(I) $\alpha_2$ expression relative to hkg. hMSC were seeded on samples immersed in SM and DM, respectively and the expression was measured with qPCR at day 11. (n=3, * p<0.1, ** p<0.05, *** p<0.01).

In order to analyze the osteogenic differentiation potential of human MSCs, the collagen I gene expression ($\alpha_1$, $\alpha_2$) was determined (**Figure 4.19 ii, iii**), which is an indicator for osteoblast progenitor inside the cell culture.[315] While a higher col I($\alpha_1$) gene expression was observed on all 2D samples compared to their 3D counterparts, the col I($\alpha_1$) gene expression on TNO-3D and SOA-3D samples was increased compared to their planar counterparts. Moreover, the col I($\alpha_2$) gene expression of TNO and SOA samples immersed in DM was in most cases increased compared to TCPS DM samples as well as the TNO-2D SM samples possessed the highest values in the DM experiment setting. The frequently higher values of the SM samples are presumable caused by dexamethasone present in the DM medium, which is known to suppress the collagen expression.[316] Nevertheless, SOA and TNO patterned samples still depicted higher values in the DM and SM setting compared to TCPS, which hints to a material dependent effect on the collagen expression. Additionally, osteoprotegerin (pro-osteoblast factor) and RANKL
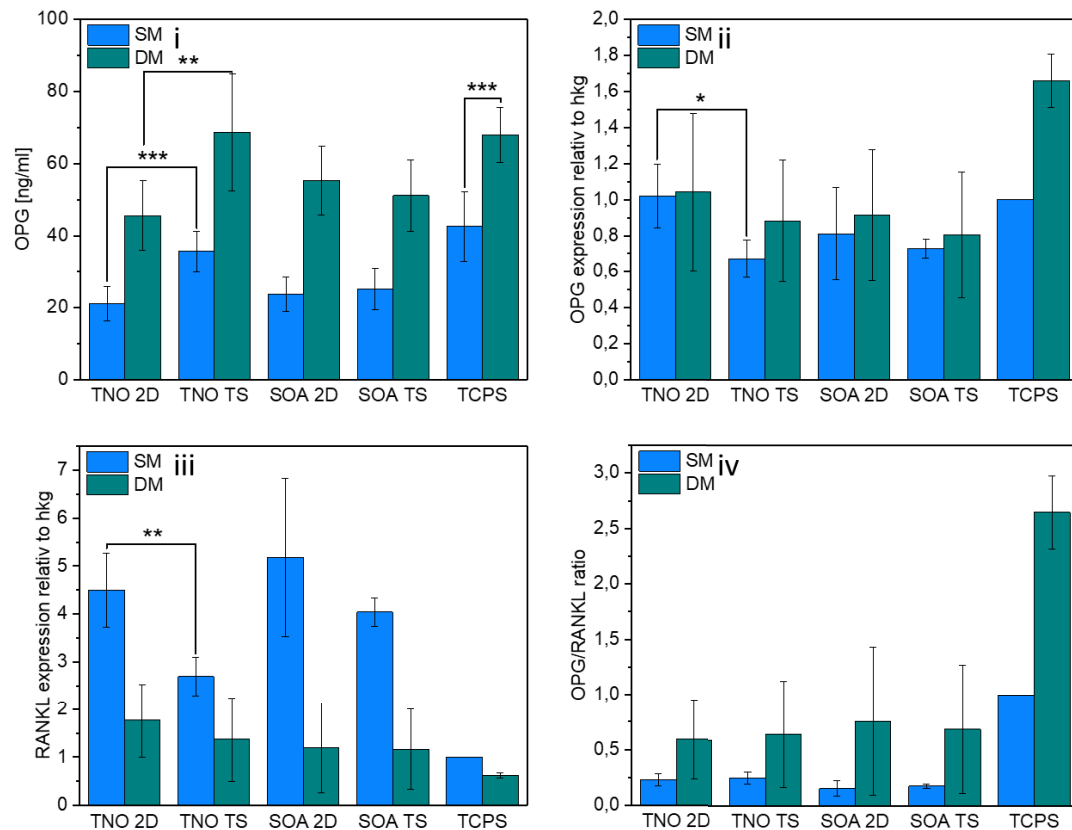
**Figure 4. 20:** Expression levels of OPG and RANKL on TNO, SOA and TCPS samples. hMSC were seeded on the samples and the OPG expression was measured with ELISA (i) and qPCR (ii) at day 11 after cell seeding. The RANKL expression (iii) relative to house-keeping genes (hkg) was measured with qPCR and the OPG/RANKL ratio 8iv) was calculated, which is an indicator for osteogenesis. Samples immersed in DM depicted a higher OPG expression compared to the SM setting, which led to a higher OPG/RANKL ratio in the DM setting (n=3, * p<0.1, ** p<0.05, *** p<0.01).

(pro-osteoclast factor) gene expressions were determined in order to calculate the OPG/RANKL ratio, which is an indicator for osteogenesis (**Figure 4.20**). A high OPG/RANKL ratio favors bone growth as OPG, which is expressed by osteoblasts, suppresses osteoclast formation by inhibiting the RANK-RANKL mechanism, which is necessary for bone resorption.[317] While a stronger OPG gene upregulation was observed in TNO-2D (DM and SM setting) and SOA-2D (SM setting) samples, the amount of expressed protein was higher in their 3D counterparts, which is similar to the results observed with the TNAP gene expression and the TNAP activity. The general amount of RANKL was reduced in the DM experiment setting, which might be caused by OPG functioning as a decoy receptor for RANKL as well as diminishing amounts of immature osteoblasts, which are known to be responsible for an increased RANKL expression.[318,319] Moreover, it was demonstrated that an advancing osteoblast differentiation decreases the expression levels of RANKL mRNA while increasing the OPG mRNA levels at the same time.[319,320] A simultaneous low expression levels of RANKL in combination with an increasing TNAP expression was therefore correlated with the presence

of mature osteoblasts in the cell culture.[319] In addition, SOA-3D and TNO-3D samples immersed in DM exhibited lower levels of RANKL gene expression than their 2D counterparts, which hints to an influence of the TS array. In line with the previous data, a slightly higher OPG/RANKL ratio was observed in samples with TS immersed in SM (TNO and SOA) and DM (TNO), which further indicates to a effect of the TS on the osteogenic differentiation.

### 4.4.3 Optical analysis of the cell layer development

Complementary to the protein and DNA analysis, optical images were taken in order to identify potential effects of the material type, fabrication setting (2D and TS samples) and the TS array on the cellular differentiation. Human MSC were therefore seeded on samples with TNO and SOA and subsequently imaged after 3 weeks in DM medium. The formation of nodules (**Figure**
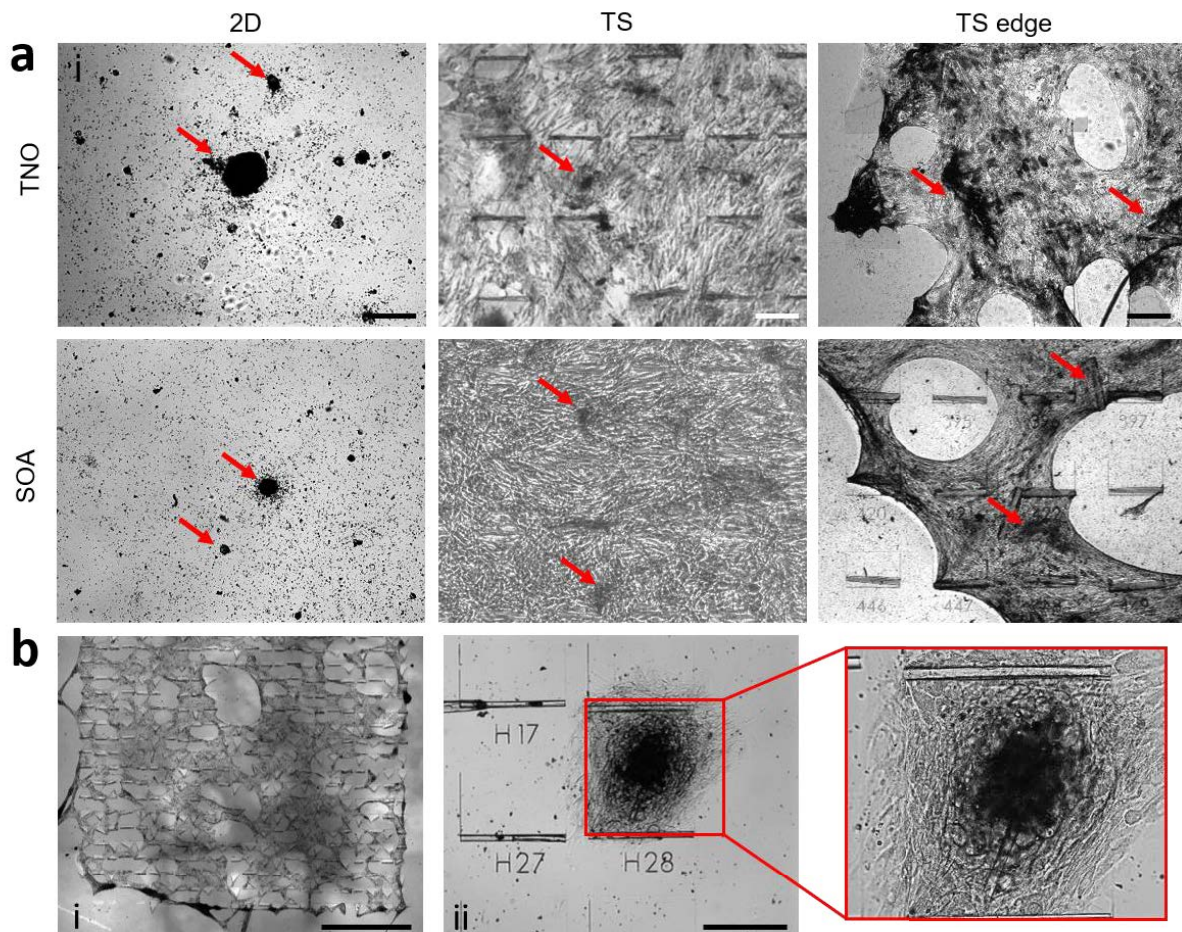


**Figure 4. 21:** Optical analysis of the layer development during osteogenesis. a) hMSC after 3 weeks in DM. Nodule formation (red arrows) was observed on TNO and SOA-2D and TS samples as well as viable cell layers were visible on the TS samples. A cell layer spanning between the TS was especially pronounced at the edge of the TS array, where the cell number and the attachment points were fewer. b) Cells start to attach to the TS at day 8 with DM (i) as well as cell clusters with nodules can be found in between several TS after 5 weeks in DM (ii). Scale bars: a: 200 µm; b-i: 2 mm, ii: 200 µm. Figure modified from reference.[302]

**4.21 a**, black aggregates, red arrows) was observed on TNO-TS, SOA-TS samples and their planar counterparts. However, while on TNO-2D and SOA-2D samples only few large nodules were observed, nodules with different sizes were scattered all over the TNO-TS and SOA-TS samples, which were also embedded in a cell layer spanning around the TS structures. The cell viability and cell layer spreading in the 3D setting was in stark contrast to the 2D samples, in which only few viable cells were still visible after 3 weeks. Furthermore, the cell layer spanning from TS to TS was stronger pronounced at the TS edge, in which a lower cell number was present. This cell layer attachment behavior towards the TS "anchor points" started in between the 7$^{th}$ and 14$^{th}$ day (**Figure 4.21 b-i**), at which point the first cells started to accumulate at the outer rim of the TS array. Thus, the alignment of the cells to the TS array might be a reason for the more ordered nodules formation detected on the 3D samples and is in strong contrast to the randomly placed nodules in the 2D condition. In addition, small isolated groups of cells were observed in the middle of the particular cell clusters, which were located in between two or more TS, after 5 weeks of DM cell culture (**Figure 4.21 b-ii**). Altogether, the observed results indicate to an effect of the TS array on the cell layer development and thereby towards an increased cell survival rate during the differentiation process.

## 4.4.4 Cell survival during osteogenic differentiation

A more detailed investigation of the cell viability on samples with TS, inside the cell nodules and in the constricted space of the TS interior, was conducted using a live (green, FDA)/dead (red, PI) staining on cells cultured 35 days in DM medium. **Figure 4.22 a** shows a cell layer around a large nodule, which is located in between a TNO-TS array. A high number of viable cells was observed in between the TS as well as close to and inside the nodule. Moreover, nearly all of the dead cells were found inside the nodule, whereas the majority of these dead cells were located at the border of the nodule structure. In line with the previous results, only few single viable cells were found in the 2D setting (data not shown here). In addition, viable cells were detected inside the TS lumen (**Figure 4.22 b, c**) and in close proximity to a presumed CaP accumulation (**Figure 4.22 b**) after 5 weeks of DM treatment. The cell movement was limited by CaP inside the TS structure that blocked the transit of cells through the TS interior. It was observed that cells migrated into the TS (**68 min**), moved close to the CaP accumulation (**92 min**) and used, in some cases, cellular extensions to partially penetrate the obstacle (**384 min**). Subsequently, time-lapse images were taken in positions in which cells were completely
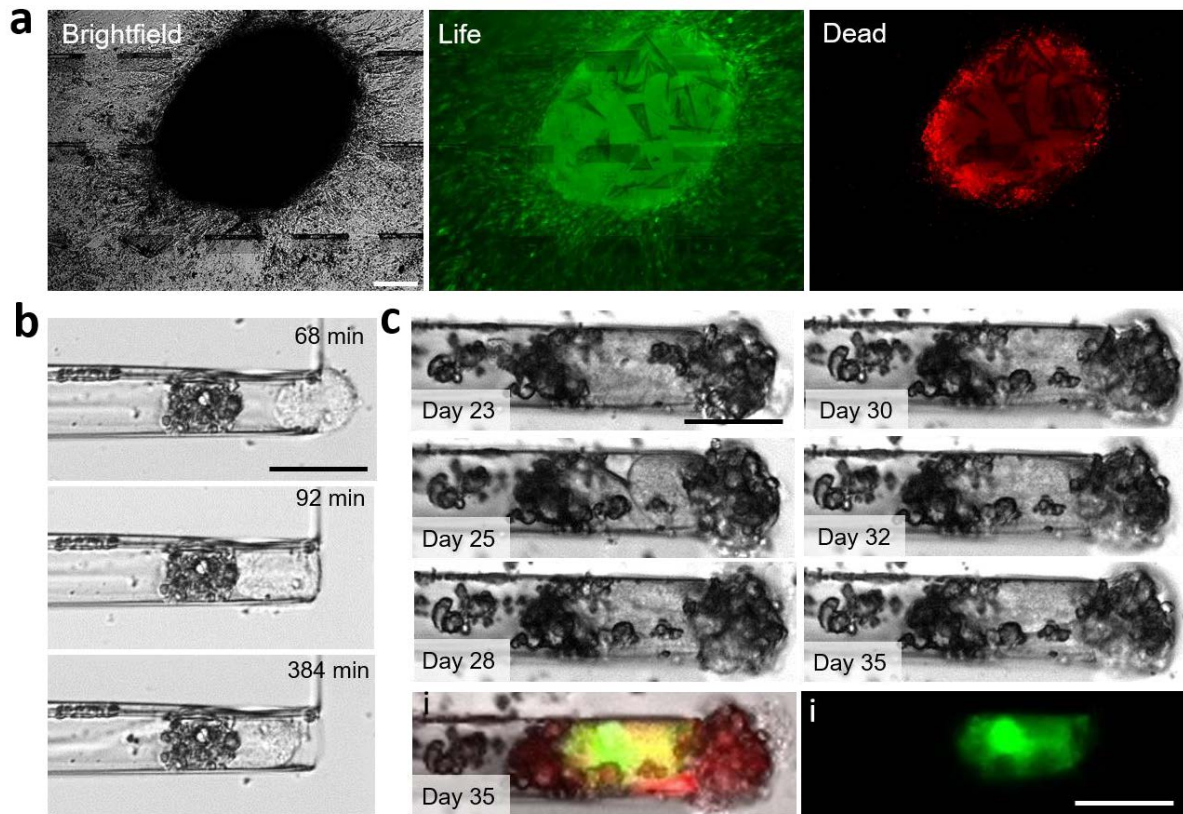
**Figure 4. 22:** Cell viability analysis of cells inside a nodule as well as in between and inside TS. a) Life/dead staining shows alive cells in between the TS and inside and around a nodule at week 5 with DM as well as dead cells are located inside the nodule. b) Cell enters TS (68 min) and is blocked by calcified material (92 min) inside the TS. It forms a lamellipodia, which partially penetrates the mineralization site (384). c) A single cell blocked between calcified material was located inside the same TS for 12 consecutive days. The viability of the cell was confirmed with a life/dead staining (green: alive, red: dead) at day 35 (ii). Scale bars: a: 200 µm; b, c: 25 µm. Figure modified from reference.[302]

surrounded by the presumed mineralized material. A temporal cell migration out of the TS would be hindered in that way, which allows an analysis of the long-term cell survival inside the constricted space of the TS. Cells could be tracked inside the interior space for 12 subsequent days (**Figure 4.22 c**), which indicates towards a sufficient oxygen and nutrition flow for long-term cell survival. Furthermore, while the cell viability was confirmed by a life/dead staining (**Figures 4.22 c-i**), also a weak red signal was observed in the position of the presumed mineralized CaP, which hints to the presence of a dead cells body. Thus, a more detailed study of the single cell mineralization inside the TS was conducted, which can be found in **Section 4.5**.

## 4.4.5 TS effects on the layer development and cell survival

The data retrieved from the TNAP activity, ELISA and qPCR measurements implies a maturation of hMSC into pre-osteoblasts/osteoblasts as key osteogenic differentiation makers such as TNAP and OPG that are upregulated during the differentiation process. The results also indicate to TS dependent effect onto osteogenic factors. This is especially pronounced in case of the TNO setting, in which osteogenic parameters were mostly upregulated in the 3D samples compared to their planar counterparts. Yet, in order to clarify the exact bone cell behavior, further studies with additional time points (later than day 11) and the analysis of late osteogenic factors would be helpful to understand possible genetic cell alterations in more detail.

In line with the protein assays, an osteogenic differentiation process was confirmed optically, as the formation of nodules was observed on all samples immersed in DM. Furthermore, the layer formation was affected by the presence of TS on the sample surface, which led to a spanning of the cell layer around the TS. This spanning might by caused by the high TNAP content in the early phase of differentiation (day 9) measured in samples with TS, which is known to lead to a multi-layered nodule formation with cell-free spaces in between.[321] Hanna et al. also demonstrated that osteogenic differentiation leads to a cell multilayer formation, in which the cells in the upper layer are in a later differentiation state.[322] Thus, early pre-osteoblasts could move onto the human MSC layer and start forming a collagen matrix above it, which is followed by the deposition of mineralized nodules. The spanning of the cell layer could also increase the layer spreading area during differentiation as additional attachment points are provided by the TS array, which might increase the nutrition supply in the lower layers. In line with that, a high number of viable cells were observed in the TS array and inside the nodule structures after 5 weeks in DM, which indicates to a long-term viability and an ongoing osteoid formation inside the nodules. However, most of the dead cells were located inside the nodule structure as well. Thus, it could be speculated that while the TS array favors the formation of a cell monolayer, which increases the cell survival rate, this effect is reduced in very dense cell accumulations like in the large nodule structures. This might explain the high cell death rate in samples without TS, which could be caused by the lack of nutrition in the lower cell layer.[323] Furthermore, the naturally occurring osteoblasts apoptosis might play a role, as it is linked to an increased CaP formation.[314]

Besides, recent studies demonstrated that the substrate curvature as well as curved microstructures influence individual cells and direct the growth of bone tissue.[260] These studies

showed that the collective organization of a cell layer increased its' sensing capacity compared to that of individuals cells, which allowed the detection of weak curvature fields and therefore an alignment of the cells along the presented curvature.[279–281] In addition, it was demonstrated that cells cultured on PDMS scaffolds with constant mean curved surfaces depicted a liquid crystal-like behavior, which caused a bridging of the cell layer in between the edges of the scaffold as well as depends on the cytoskeletal tension of the cells.[282] This collective self-organization of cells consequently led to an energy minimizing of the cell layer.[282] The above-depicted layer development might be therefore connected to the curvature provided by the regularly ordered TS array. Consequently, it can be speculated that the cell layer recognizes the TS arrays as an ordered curved environment, which leads to a layer alignment to the presented topography. The surface layer tension subsequently increases, which might be counterbalanced by surface energy reduction due to layer spanning from TS to TS.

## 4.5 Cell driven mineralization processes inside TS

The major aim of the project was the fabrication of a realistic platform that mimics micropores present in *in vivo* implants to study bone cell mineralization processes in confined microspaces. The first steps towards that goal were acquired by characterizing the cell layer development, the viability and the osteogenic potential of the relevant materials. This section subsequently provides a detailed analysis of the mineralization processes inside the TS. The amount of presumed calcium deposits was therefore analyzed in different sized tubular microscaffolds and the cell-mediated formation of CaP inside the TS was characterized with time-lapse imaging. Furthermore, the presence of calcified organic material was verified using staining procedures (Alizarin Red, Von Kossa) and the composition of a presumed hydroxyapatite crystal was identified by a TEM analysis.

### 4.5.1 Amounts and states of calcified material inside TS

TNO-TS were examined for an internal presence of presumed CaP contents after 5 weeks of Differentiation Medium (DM) treatment (**Figure 4.23 a**). Due to the limitations of conventional optical microscopy, only 2D images of the lower TS side were taken and not from the complete 3D volume. The provided data is therefore an estimation of the CaP volume inside the TS based
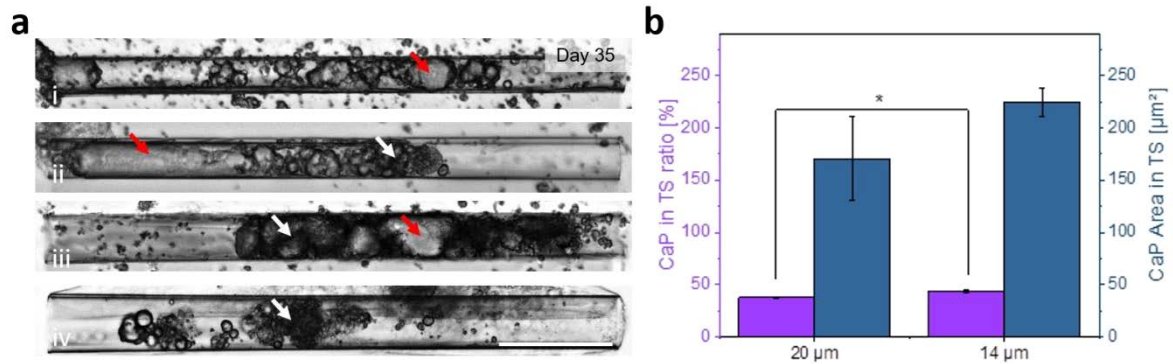
**Figure 4. 23:** Mineralization inside TS with different diameters. a) Presumed CaP deposits are found in TNO-TS with different diameter. The amounts and positions of CaP content varies inside the TS as well as a non-crystallized state (white arrow) and a crytallized state (red arrow) were observed inside TS; b) Ca/P ratio and CaP covered area inside the TS was compared between samples (at least more than 250 TS per samples) with a mean TS diameter of 14 μm and 20 μm. More calcified TS were seen on the sample with smaller TS diameter (14 μm, mean value over the whole sample) compared to higher diameters (20 μm) as well as a larger area of the TS was covered with calcified material. (n=3, * p<0.1, ** p<0.05, *** p<0.01). Scale bar: 50 μm. Figure modified from reference.[302]

on the particular TS diameter (height). Presumed CaP formations were found within TS with a diameter range in between 10-40 μm, in different positions inside the TS (middle and side) and diverse quantities. While only small sections of the whole internal volume were covered with CaP in some TS (**Figure 4.23 a-i, -iv**), nearly a full coverage of the TS area was reached in other TS (**Figure 4.23 a-ii, -iii**). Furthermore, different states of the internal material were observed, a lighter, more solid phase (**red arrows**), as well as a darker more loosely, disconnected state (**white arrows**). The CaP content (CaP-ratio: calcified TS/total number of TS) was determined with samples with a similar average diameter (~14 μm and ~20 μm), which possessed at least 250 TS on their sample surface (**Figure 4.23 b**). A slightly higher number of CaP formation sites were observed in TS with 14 μm compared to their 20 μm counterparts, which also resulted in a higher area coverage inside these structures.

## 4.5.2 Time lapse imaging of mineralization processes inside TS

A detailed analysis of single cell mineralization processes inside TS was conducted with a time-lapse image sequence tracking single cells inside TNO and SOA-TS during 5 weeks of osteogenic differentiation. In case of the TNO-TS (**Figure 4.24 a-i**), viable cells were detected at day 8 and 10 inside the TS confinement. The cell morphology strongly changed in the following days, which included the loss of the cell body integrity (day 14) indicating to an occurred cell death. Subsequently, a gradual darkening of the cell body took place in between day 14 and 21. The dark material was thereafter replaced with a light-colored crystal-like
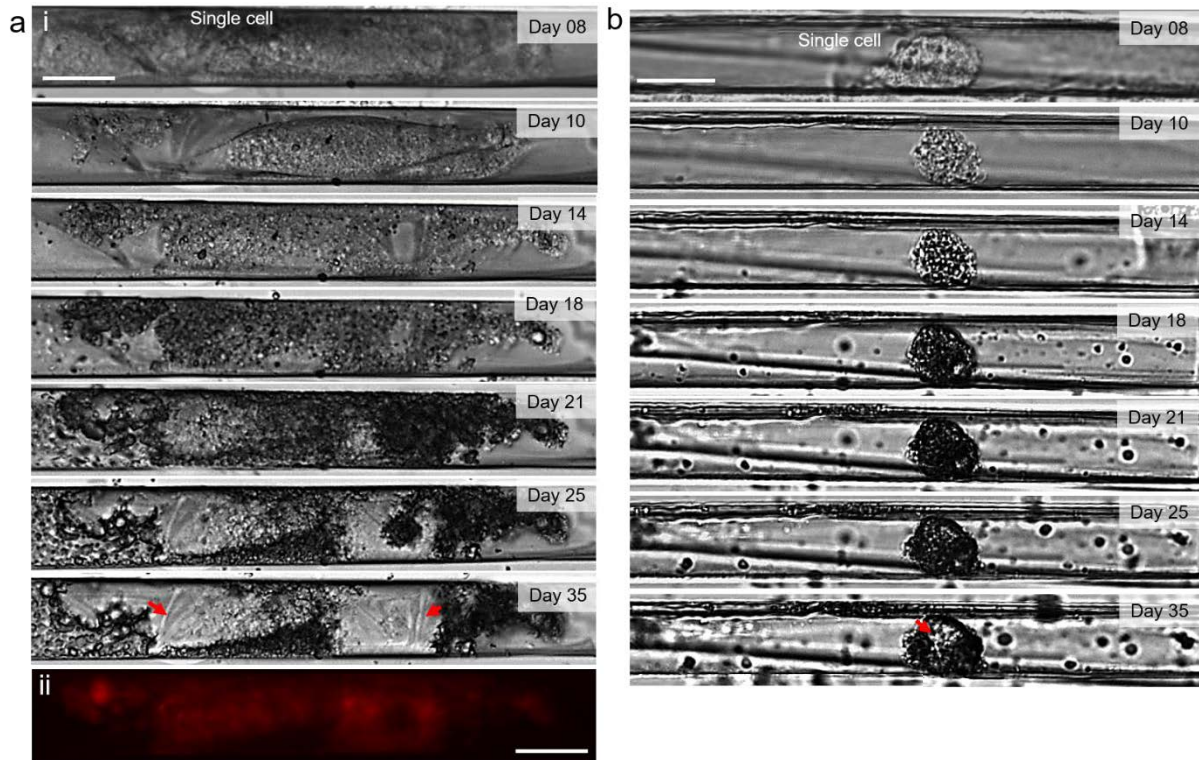
**Figure 4. 24:** Mineralization over time inside TS by single cells. a) TNO-TS and b) SOA-TS are depicted between days 10 – 35 in DM. After a presumed cell death between days 8 – 14, CaP accumulates and the cell body crystallizes (red arrows) over time (a-i, b). Live/dead staining of the former cell identified it as a dead cell (a-ii). Scale bar = 25 µm. Figure modified from reference.[302]

material until day 35 (**Figure 4.24 a-i, red arrows**). A similar process sequence was observed inside the SOA-TS in between day 10 and day 21, in which a deformation and darkening of the former living cell (day 8) occurred (**Figure 4.24 b**). The dark material was subsequently replaced until day 35, which is similar to the process observed on TNO-TS. The difference in cell size and the magnitude of the mineralization processes in the two different TS settings could be explained by a natural occurring variance of cell sizes in the contemplated cell population, which is known to be affected by several factors such as cell aging.[48] Furthermore, segments of the crystal-like parts were identified as dead cell compartments by using a live/dead staining (**Figure 4.24 a-ii**). All in all, the observed process indicates to a dead cell body induced mineralization process, in which a gradual calcification of the organic cell parts occurs.

### 4.5.3 Alizarin Red and Von Kossa staining

In order to identify mineralized deposits inside the cell layer, cells were seeded on TNO and SOA samples, cultured for 3 weeks immersed in DM and subsequently treated with an Alizarin red staining (**Figure 4.25 a**). Samples immersed in SM with cells and samples immersed in DM
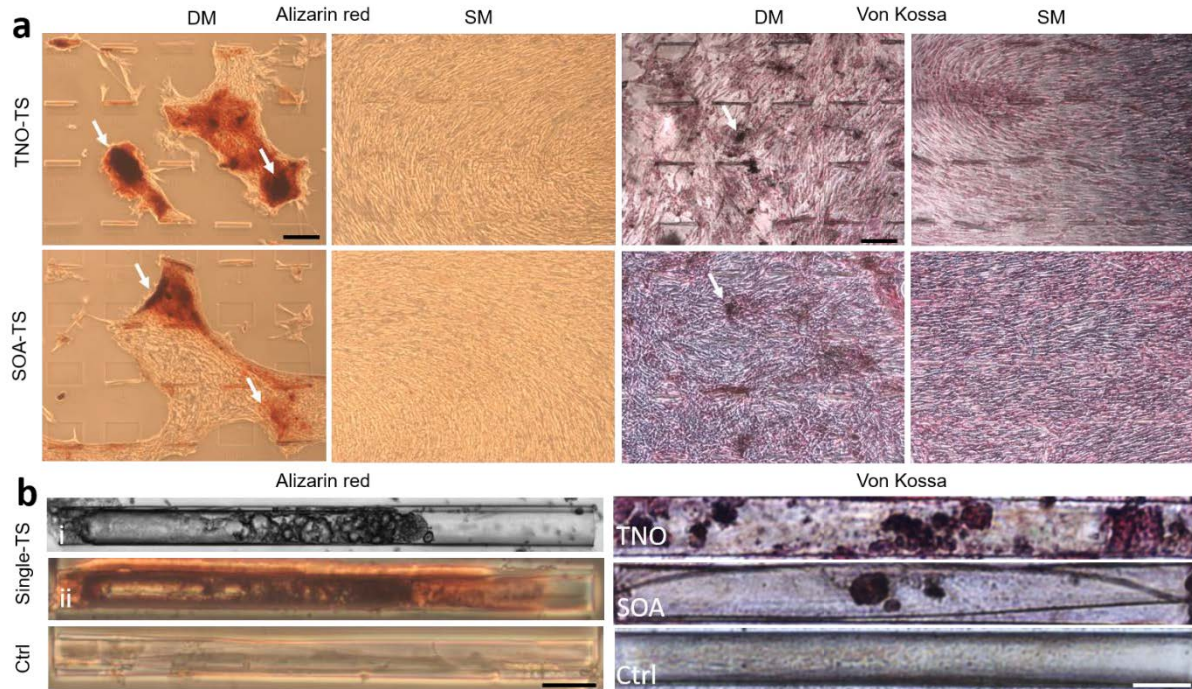
**Figure 4. 25:** CaP deposit staining of the cell layer and inside TS. a) Ca deposits stained with Alizarin Red and Von Kossa of TNO and SOA samples immersed in DM. CaP deposits were only found on samples with cells, which were immersed in DM. b) CaP depositions could also be found and stained inside single TS. Scale bars: a: 250 μm; b: 25 μm. Figure modified from reference.[302]

without cell functioned as a control. On both materials types (TNO-TS and SOA-TS), the black aggregations (nodules, **white arrows**) were stained red, which confirmed the presence of mineralized material (calcium) in the particular nodule. In contrast to that, no nodules and mineralized components were identified on samples with SM. These results were verified by Von Kossa staining (**Figure 4.25 a**), in which mineralization deposits (calcium and phosphate) were stained black (metallic silver). Mineralized deposits were observed in between TS on both material types in the DM setting. In line with the Alizarin Red results, no signs of an osteogenic differentiation were observed on samples with SM and on samples without cells. Furthermore, numerous healthy cells (stained pink) were identified inside the cell layer, which confirmed a high viability after 3 weeks in DM samples with TS. Regarding the CaP formation inside the TS, single TNO-TS were imaged before and after the staining process (**Figure 4.25 b-i**). The observed presumed CaP formations were stained red by the Alizarin Red solution, which verified the presence of CaP inside the TS (**Figure 4.25 b-ii**). In addition, no signs of a false negative staining was encountered in the control samples (Ctrl) as well as in TS without internal deposits on the same sample. These results were confirmed by a Von Kossa staining, which showed mineralized deposits inside TNO-TS and SOA-TS immersed in DM, but not in the control samples (**Figure 4.25 b**, **Von Kossa**).

### 4.5.4 Mineralization state characterization

Complementary to the staining experiments, TEM studies were conducted to provide detailed information about the CaP composition inside the TS. Structures with internal deposits were selected by optical microscopy and subsequently analyzed with a TEM setup. In order to access the CaP material, a FIB-cut was performed, which allowed SEM and TEM imaging of the internal material without inflicting large damage to the TS structure (**Figure 4.26 a-i**). The SEM images depict mineralized material inside the TNO (**Figure 4.26 a-ii**) and SOA (**Figure 4.26 a-iii**) TS, which possessed a typical CaP crystal structure on the outer surface. Furthermore, high magnification images revealed two distinct material phases inside the dense material layer (**Figure 4.26 b-i**). Small, porous darker parts (**1**) were surrounded by a thick white mass (**2**), which indicate to a crystallized phase surrounded by biological cell mass. Moreover, nano-sized needle-like structures were observed in the assumed mineralized area with TEM imaging (**Figure 4.26 b-ii, -iv**), which represent typical growth patterns of hydroxyapatite crystals.
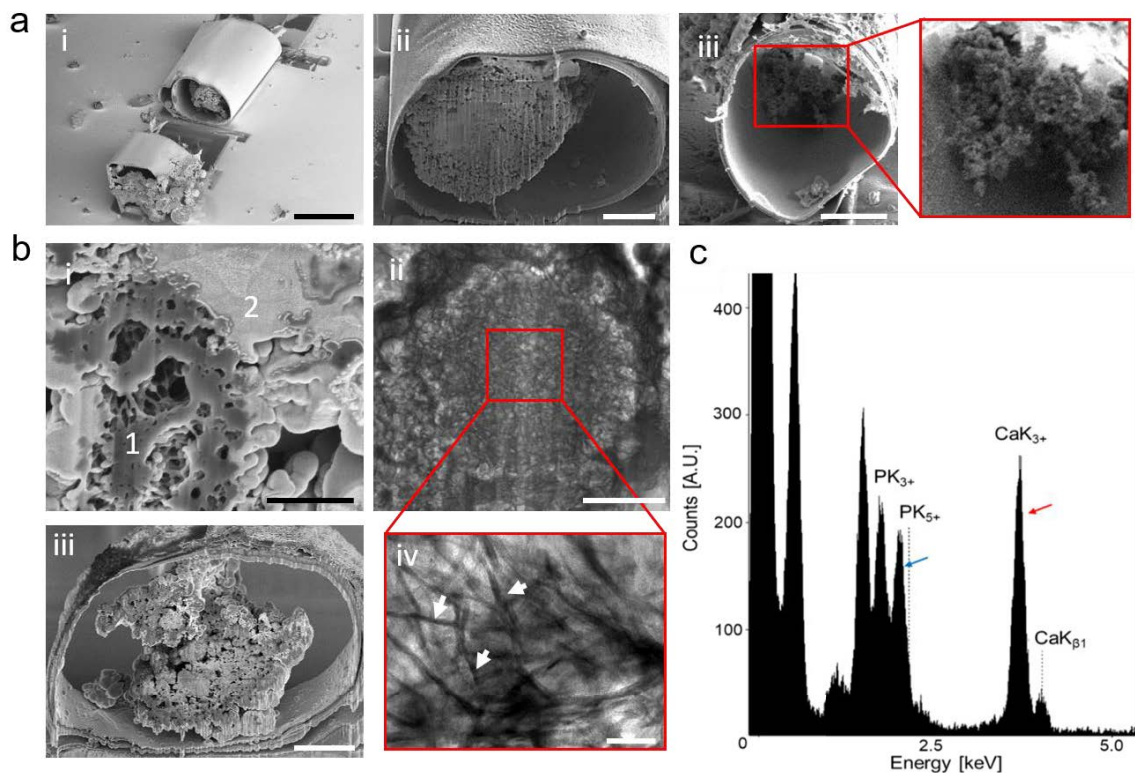


**Figure 4. 26:** SEM and TEM analysis of mineralized material inside TS. a) FIB-cut of TS with CaP content inside its lumen (i). CaP content was located in TNO (ii) and SOA (iii) TS b) TEM analysis of the mineralized material (i) shows a CaP like structure (1) surrounded by a presumed biomass (2). High magnification images of the crystallized areas show characteristic needle-like CaP structures (ii, iv). A thin of the mineralized material inside the TS was prepared for further studies. c) EDX spectrum depicts CaP peaks from the mineralized material inside the TS. Scale bars: a-i: 25 µm, a-ii, iii: 5 µm; b-i, ii: 500 nm, b-iii: 5 µm, b-iv: 50 nm. Figure modified from reference.[302]

Additionally, a thin lamella (**Figures 4.26 b-iii**) of the mineralized material was prepared, which allowed an investigation of the particular Ca and P components by Energy-Dispersive X-ray spectroscopy (EDX). The EDX pattern revealed typical peaks of P ($PK_{3+}$ and $PK_{5+}$) and Ca ($CaK_{3+}$ and $CaK_{\beta1}$) located next to the atomic components of the particular TS (**Figure 4.26 c**). Several positions inside and outside the TS were subsequently analyzed with EDX, which resulted in an average CaP molar ratio between $1.26 \pm 0.14 - 1.29 \pm 0.04$ (**Table 4.5**).

**Table 4. 5:** Ca/P ratios obtained by EDX measurements

| Element | Outside TS | Inside TS |
|---|---|---|
| P-K (at%) | $44.44 \pm 0.82$ | $43.67 \pm 2.96$ |
| Ca-K (at%) | $55.56 \pm 0.82$ | $56.33 \pm 2.96$ |
| Ca/P ratio | $1.29 \pm 0.04$ | $1.26 \pm 0.14$ |

While these values are slightly lower than the stoichiometric composition of $Ca_{10}(PO_4)_6(OH)_2$ with a molar ratio of 1.67, biological hydroxyapatite (HA) is normally Ca- deficient as $Ca^{2+}$ can be substituted by $Mg^{2+}$ or $Na^+$, which results in a molar range of $1.2 - 1.5$ for biologically formed HA.[324–326] Additionally, diverse forms of calcium phosphates like tricalcium phosphate
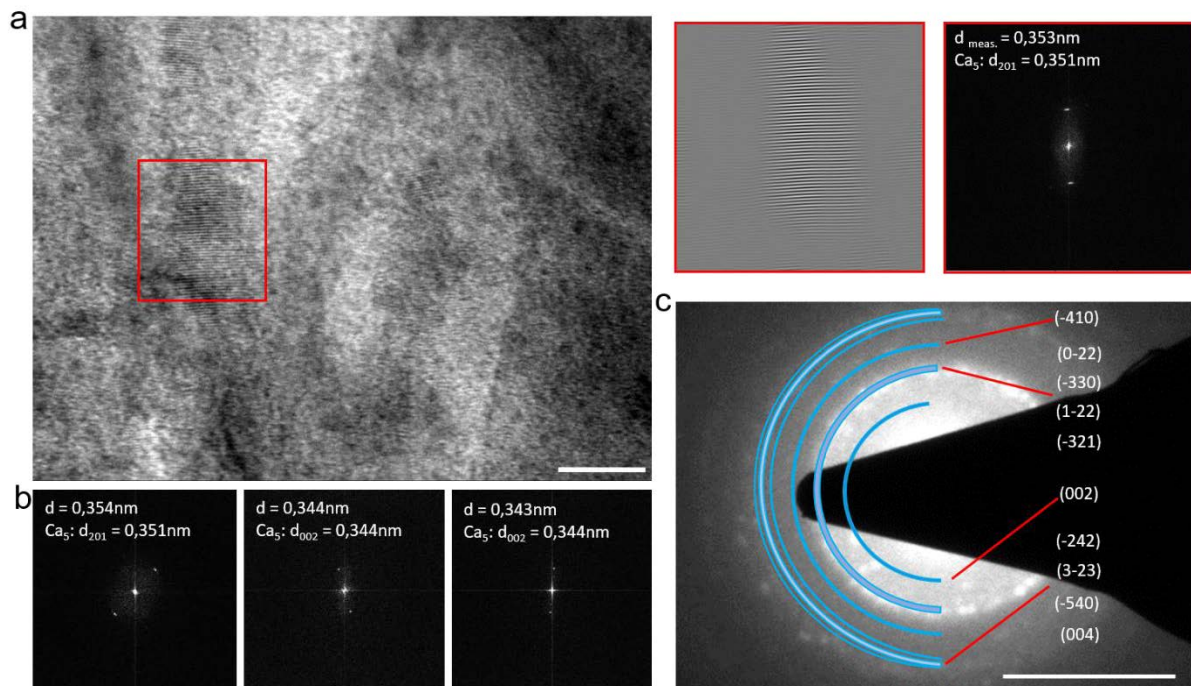


**Figure 4. 27:** Characterization of the mineralized material. a) Crystal planes and reflexed of a needle-like structure. b) The measured reflexes match the characteristic crystal lane distances of hydroxyapatite ($Ca_5(PO_4)_3OH$), which was confirmed with a circle plot (c). Scale bars: a: 10 nm; c: 5 nm. Figure modified from reference.[302]

and octacalcium phosphate are present during the biological mineralization process. They represent unstable pre-hydroxyapatite states present in the initial bone-forming phase and therefore possess higher contents of phosphates, which reduce the Ca/P molar ratio further.[327] Furthermore, as the cell culture experiments in this study were conducted for a maximum duration of 5 weeks, an incomplete bone formation has to be assumed as full bone growth normally takes up to several months. Therefore, the molar ratio might have to be compared to newly formed bone, which possesses a lower density than mature bone and a Ca/P molar ratio of 1.32 (cortical bone).[328]

Besides, high magnification STEM images of the needle-like structures were prepared (**Figure 27 a**) in order to confirm the existence of a crystallized state of hydroxyapatite (HA) and thereby exclude the possibility of a simple accumulation of CaP in the particular samples. Crystal lanes with the typical lattice plane distances of 0.353 nm ($Ca_5(PO_4)_3OH$: $d_{201}$ plane) for a hydroxyapatite crystal growth were observed (**Figure 4.27 a, b**, **Table 4.6**). Furthermore, crystal peaks obtained from a SAED measurement matched the characteristic ring pattern of $Ca_5(PO_4)_3OH$ (ELDISCA[329], **Figure 4.27 c**), which underlines the presence of HA inside the TS.

All in all, the single cell mineralization inside the TS was successfully characterized by the TEM analysis and confirms the presence of crystallized hydroxyapatite inside the TS, which is likely related to a gradual dead cell body mineralization over time.

**Table 4. 6: Crystal reflexed obtained from the mineralization site compared to hydroxyapatite**

| Position | Measured reflex [nm] | Hydroxyapatite literature [nm][329] |
|---|---|---|
| 1 | 0.353 | 0.351 |
| 2 | 0.354 | 0.351 |
| 3 | 0.344 | 0.344 |
| 4 | 0.343 | 0.344 |

## 4.5.5 Mineralization mechanisms inside confined spaces

Bone mineralization is commonly described as a complex multiple step process, which is primarily conducted by osteoblast. They initially secrete a mixture of organic components that mainly consist of collagen type I.[61] Matrix vesicles are then released from osteoblast into the surrounding environment and start to accumulate $P_i$ and $Ca^{2+}$ in their lumen until a critical mass is reached, which leads to the formation of initial apatite crystals.[62,330] These crystals subsequently bind to gap regions present in the collagen network, which ultimately causes a mineralization of the protein matrix.[62,63] However, recent studies suggest a second calcification pathway, which involves the mineralization of apoptotic cell bodies.[331] Kirsch et al. showed that the breakdown of the membrane phospholipid symmetry during apoptosis allows the accumulation of $Ca^{2+}$ and $P_i$ ions inside the outer cell membrane of apoptotic cell bodies. This process was independent of the alkaline phosphatase and ultimately led to the mineralization of apoptotic bodies.[331] A comparable study conducted by Fujita et al. demonstrated that necrosis and apoptosis are closely related to the calcification process.[332] By utilizing an osteogenic culture of human MSC, they showed that the calcification was significantly promoted by necrotic cells. Furthermore, dead cells were surrounded by calcium deposits, which indicated towards the possibility that apoptotic cells can serve as nucleation sites for a subsequent mineralization process.[332] A similar mineralization process was observed in this thesis, which also involved a mineralization of a dead cell body over time. By using a time-lapse analysis, it was demonstrated here, that the formation of different amounts of calcified tissue was preceded by an occurring cell dead inside the TS. Furthermore, since a gradually change of the material inside the TS from dark to light colored (day 21-35) was observed, it can be expected that the dead cell bodies initially served as crystal nucleation sites and subsequently mineralized over time. This assumption is furthermore supported by the verification of the dead cell body with a live/dead staining and by the presence of hydroxyapatite crystals inside the TS, which possessed Ca/P molar ratios characteristic for an early bone formation. The dead cell body calcification process depicted in this thesis therefore shades a new light on a possible mineralization of small implant pores, since it occurred inside the TS in absence of the formation of mature stress fiber, which are commonly associated with an increased cytoskeleton and the osteogenic differentiation of cells.[274,333] Furthermore, while viable cells were observe inside the TS, the nutrition and oxygen supply for the cells could still be limited inside the TS due to the high spatial constriction. Since these limitations are positive regulators for cell autophagy and recent studies demonstrated that mineral containing needle shaped structures were observed inside

autophagic-like vesicles in bone cells, autophagy might contribute to the mineralization process inside the TS.[334,335] Accordingly, a study conducted by Dang et al. showed that cell autophagy can trigger cell death dependent on the respective cytokine composition present in the microenvironment of the cell.[336] Cells in an autophagy state could subsequently form CaP inside their cell bodies, release CaP into their environment via microvesicles or by cell death and therefore contribute to a mineralization inside small pores. Yet, a study conducted by Lo et al. showed that pore diameters between 47 – 198 µm had no influence on the MSC cell viability during the first 5 days of cell culture, which would contradict a reduced nutrition suppy.[213] However, the here fabricated TS possess smaller diameters (10 – 42 µm) compared to the above-mentioned study. Consequently, a slow transition into an autophagy state could be triggered by a gradually reduction of nutrition and oxygen supply due to the spatial reduction of the TS, which could ultimately lead to cell death and induce a mineralization process. All in all, the results of this thesis demonstrated that a mineralization of pores smaller than 50 µm is possible and likely mediated by a dead cell body calcification, which is in stark contrast to former studies claiming that only larger diameter support the bone formation process.[337] However, since an additional influence of autophagy can't be excluded, more systematic studies are required in order to decipher the exact mechanisms triggering the mineralization processes in small pores.

# 5 Conclusion and Outlook

In summary, the results of this thesis demonstrate that tubular microscaffolds (TS) can be fabricated out of relevant implant materials and be subsequently used to influence individual bone cells. By mimicking small pores which exist inside porous implant scaffolds, this *in vitro* microplatform offers a simple way to observe single bone cell-implant interactions and early bone formation processes inside a confined 3D microenvironment. It was demonstrated that by using strain-engineering and various deposition approaches (sputtering, PLD) TS could be fabricated out of thin Ti-45Nb (wt%) layers. Reactive sputtering particularly simplified the production of large arrays of transparent TS structures on a single glass substrate and allowed a sample mass production by utilizing a wafer fabrication approach. The ability to fabricate a high number of complex samples in a simple way is a clear advantage of this approach and permits the conduction of extensive cell studies. Furthermore, by tuning the thickness of these transparent Ti-45Nb (wt%) oxide (TNO) layers, a broad diameter range (10-42 µm) was acquired, which is similar to the diameter of a single human Mesenchymal Stem Cell (MSC). In addition, arrays of $SiO/SiO_2/Al_2O_3$ (SOA) TS were fabricated in the same diameter range and functioned as control samples for cell experiments in order to verify the influence of different material compositions on the cell behavior. A subsequent material analysis conducted on TNO layers demonstrated that the elemental composition of the implant material ($Ti_{70}Nb_{30}$ (at%) was closely transferred to the thin layers ($Ti_{64}Nb_{36}$ (at%)) deposited with reactive sputtering. The acquired TNO layers were fully oxidized, amorphous and consisted of mixed Ti- and Nb-oxides (($Ti_xNb_{1-x}$)$O_2$ ,x range 0.65 to 0.5) and minor fractions of stoichiometric oxides. Moreover, surface characterizations showed that TNO layers possessed contact angles in between 40°-70°, which lies within the optimal range for protein adsorption processes. All in all, the results from the first part demonstrate that strain-engineering allows a rapid fabrication of a high number of biocompatible tubular microscaffolds, which possess adequate geometrical, chemical and physical properties for a detailed cell analysis.

In the second part of the thesis, these TS were utilized to assess the influence of microtopography provided by TS arrays and the material composition (TNO, SOA) onto the cell proliferation rate, cell adhesion behavior and the osteogenic differentiation potential of MSC. The results of this thesis verified an influence of the TS onto the cells, since an elevated proliferation rate was observed on TNO samples with TS arrays compared to planar samples with the same material type and SOA samples. Furthermore, geometric cues provided by the

TS directed the nodule formation and increased the cell layer viability during osteogenic differentiation, which was increased on samples with TS compared to planar samples of the same material type. The influence of the TS and the material composition on the osteogenic differentiation was confirmed with qPCR and protein assays (ELISA), which demonstrated higher expression levels of osteogenic factors (OPG/RANKL ratio) and enzyme activities (TNAP activity) on TS samples compared to their planar counterparts as well as on TNO and SOA samples compared to TCPS control samples. These results are comparable to cell studies conducted on modified surfaces (e.g. pillars, grooves) and therefore underline the importance of modifying implant surfaces with adequate microtopographies in order to guide cell layer growth. It also shows that TS arrays can serve as micropatterned environments, which can be used to steer and analyze the behavior of cell layers during their proliferation and differentiation phase.

Moreover, a long-term (> 5 weeks) single cell analysis was conducted in order to analyze how a spatial constriction affects the cell migration, their morphology and bone mineralization processes. The spatial confinement caused a switch in between amoeboid and mesenchymal migration modes, a morphology change from a wide-spread to an elongated cell shape, the formation of large dendritic cell extensions and the reduction of stress fibers. These results are comparable to similar studies using other cell types and point towards the usage of integrin-free cellular mechanisms by cells in constricted environments. They also emphasize the importance of providing cells with an adequate *in vitro* environment to obtain reliable cell responses. Subsequently, long-term (5 weeks) time-lapse analyses were conducted on living single cells, which were located inside TS during osteogenic differentiation, in order to analyze mineralization processes in small pores. This study revealed that dead cell bodies can lead to a partial mineralization of TS with diameters in between 10-40 µm. Moreover, different states of the mineralized material were observed over time and indicate towards a gradual calcification of the organic cell parts. The presence of calcified material was subsequently verified by staining procedures (Alizarin Red, Von Kossa), as well as TEM and SEM measurements, which confirmed the existence of hydroxyapatite crystals in the CaP formation. Moreover, an EDX analysis revealed an average CaP molar ratio of $1.26 \pm 0.14 - 1.29 \pm 0.04$, which is within the typical range of biological hydroxyapatite. The results of this thesis therefore show that a different type of mineralization mechanism can be used in small pores, which is initiated by single cells serving as nucleation sites for an early bone formation process. The here presented data therefore contradict previous studies, which assumed that a mineralization can only occur in pores larger than 50 µm.

In conclusion, TNO-TS are a powerful tool to monitor single bone-implant material interactions in detail. The here presented platform provides bone cells with a realistic 3D *in vitro* environment, can be fabricated in various diameters, easily modified with additional functional layers (electronics, biological functionalization) and used for long term cell studies. TNO-TS are furthermore compatible with sophisticated methods such as high-resolution optical microscopy and TEM/EDX analysis, with which detailed information about bone-implant mineralization processes can be obtained. Due to these factors, a TNO-TS platform can provide viable information about mineralization processes, which might be used to improve porous bulk implants in the future.

Highly complex 3D *in vitro* platforms have a great potential to provide patient-specific information about bone cell-implant interaction for the medical field. The great advantage of the strain-engineered $TiNbO_x$ TS microplatform lies within its versatile and easy to apply modification prospects, which could facilitate the study of single cells responses *in vitro*. However, the complexity of the existing platform should be improved for future applications in order to get closer to *in vivo* condition and to provoke additional cell responses. A more complex environment could be achieved by, for instance, biological functionalization (e.g. actin coating, collagen coating) of the inner TS surface combined with a surface modification with nano particles (e.g. gold nano particles). These modifications would provide cells with more geometrical cues and biological adhesion markers, which are known to steer the cell adhesion and migration behavior.

Furthermore, additional environmental factors such as electrical fields, mechanotransduction and fluid flow stimulation, which are present in the *in vivo* cell surroundings, could be integrated into the platform and used for cell stimulation. For instance, mechanical cell stimulation could be obtained by the integration of piezoelectric materials, which would allow a localized mechanical stimulation of single cells as well as by micropump systems, which would provide a flow inside the TS that could stimulate the cell mechanosensors.[192] A precise control over the exact flow strength and duration would be possible thanks to the constricted 3D geometry of the TS. This would facilitate finding which parameters are exactly needed to affect integrin-mediated mechanoreceptors. Besides, electrical stimulation of bone cells was shown to strongly affect cell processes related to bone healing such as proliferation, osteogenic differentiation and cell alignment. Thus, TS with integrated electrodes could be used to specifically target and stimulate single bone cells inside the constricted, controllable TS environment in order to gain deeper information about the effects of electrical field on the osteogenic differentiation. Simultaneously, these electrodes could be utilized to sense changes

in the bone cell electrical states due to the above-mentioned environmental factors, which can influence the cell transmembrane proteins, gap junctions and the plasma membrane. The electrodes could be further utilized as a guidance system to steer cell migration, cell alignment and cell adhesion processes.

Moreover, by the integration of drug-carrying particles into the TS inner surfaces, TS arrays could be utilized as drug screening systems. The TS platform would subsequently allow a direct monitoring of drug effects on cells with a high resolution optical microscopy system. In general, all the described modification settings can also be combined with systematic studies on constriction effects on cell behavior by utilizing TS with different diameters.

In summary, there are multiple available ways to modify the here presented platforms and therefore increase their capacity to unravel single cell-implant material interaction processes.

# 6 References

1.      Noskovicova, N., Hinz, B. & Pakshir, P. Implant Fibrosis and the Underappreciated Role of Myofibroblasts in the Foreign Body Reaction. *Cells* **10**, 1794 (2021).

2.      Chen, Q. & Thouas, G. A. Metallic implant biomaterials. *Materials Science and Engineering R: Reports* **87**, 1–57 (2015).

3.      Förster, Y. *et al.* Surface modification of implants in long bone. *Biomatter* **2**, 149–157 (2012).

4.      Hunt, J. A., McLaughlin, P. J. & Flanagan, B. F. Techniques to investigate cellular and molecular interactions in the host response to implanted biomaterials. *Biomaterials* **18**, 1449–1459 (1997).

5.      Donati, D., Zolezzi, C., Tomba, P. & Viganò, A. Bone grafting: Historical and conceptual review, starting with an old manuscript by Vittorio Putti. *Acta Orthopaedica* **78**, 19–25 (2007).

6.      Alvarez, K. & Nakajima, H. Metallic Scaffolds for Bone Regeneration. *Materials (Basel).* **2**, 790–832 (2009).

7.      Sato, Y., Kitagawa, N. & Isobe, A. Implant treatment in ultra-aged society. *Japanese Dental Science Review* **54**, 45–51 (2018).

8.      Wada, T., Nakashima, T., Hiroshi, N. & Penninger, J. M. RANKL–RANK signaling in osteoclastogenesis and bone disease. *Trends Mol. Med.* **12**, 17–25 (2006).

9.      Saini, M., Singh, Y., Arora, P., Arora, V. & Jain, K. Implant biomaterials: A comprehensive review. *World J. Clin. Cases  WJCC* **3**, 52 (2015).

10.     Trevisan, F. *et al.* Additive manufacturing of titanium alloys in the biomedical field: processes, properties and applications. *J. Appl. Biomater. Funct. Mater.* **16**, 57–67 (2018).

11.     Dehghanghadikolaei, A. & Fotovvati, B. Coating Techniques for Functional Enhancement of Metal Implants for Bone Replacement: A Review. *Materials (Basel).* **12**, 1795 (2019).

12.     Joshi, M. G., Advani, S. G., Miller, F. & Santare, M. H. Analysis of a femoral hip prosthesis designed to reduce stress shielding. *J. Biomech.* **33**, 1655–1662 (2000).

13.     Ikhwan, M. *et al.* Problem of Stress Shielding and Improvement to the Hip Implant Designs: A Review. *Artic. J. Med. Sci.* (2007). doi:10.3923/jms.2007.460.467

14.     Niinomi, M., Liu, Y., Nakai, M., Liu, H. & Li, H. Biomedical titanium alloys with Young's moduli close to that of cortical bone. *Regen. Biomater.* **3**, 173–185 (2016).

15.     Niinomi, M. & Nakai, M. Titanium-based biomaterials for preventing stress shielding between implant devices and bone. *International Journal of Biomaterials* (2011). doi:10.1155/2011/836587

16.     Yuan, L., Ding, S. & Wen, C. Additive manufacturing technology for porous metal implant applications

and triple minimal surface structures: A review. *Bioact. Mater.* **4**, 56–70 (2019).

17.    Zhuravleva, K. *et al.* Porous low modulus Ti40Nb compacts with electrodeposited hydroxyapatite coating for biomedical applications. *Mater. Sci. Eng. C* **33**, 2280–2287 (2013).

18.    Jones, J. R. & Hench, L. L. Regeneration of trabecular bone using porous ceramics. *Curr. Opin. Solid State Mater. Sci.* **7**, 301–307 (2003).

19.    Wang, X. *et al.* Topological design and additive manufacturing of porous metals for bone scaffolds and orthopaedic implants: A review. *Biomaterials* **83**, 127–141 (2016).

20.    Chin, R. & Lee, B. Y. *Principles and Practice of Clinical Trial Medicine. Principles and Practice of Clinical Trial Medicine* (Elsevier, 2008). doi:10.1016/b978-0-12-373695-6.x0001-4

21.    Mak, I. W. Y., Evaniew, N. & Ghert, M. Lost in translation: Animal models and clinical trials in cancer treatment. *American Journal of Translational Research* **6**, 114–118 (2014).

22.    Ma, C., Peng, Y., Li, H. & Chen, W. Organ-on-a-Chip: A New Paradigm for Drug Development. *Trends in Pharmacological Sciences* **42**, 119–133 (2021).

23.    Wang, Z. *et al.* Analysis of factors influencing bone ingrowth into three-dimensional printed porous metal scaffolds: A review. *J. Alloys Compd.* **717**, 271–285 (2017).

24.    Zhang, B., Korolj, A., Lai, B. F. L. & Radisic, M. Advances in organ-on-a-chip engineering. *Nature Reviews Materials* **3**, 257–278 (2018).

25.    Weiz, S. M., Medina-Sánchez, M. & Schmidt, O. G. Microsystems for Single-Cell Analysis. *Adv. Biosyst.* **2**, 1700193 (2018).

26.    Huang, G. & Mei, Y. Assembly and Self-Assembly of Nanomembrane Materials-From 2D to 3D. *Small* **14**, 1703665 (2018).

27.    Clarke, B. Normal Bone Anatomy and Physiology The Skeleton. *Clin J Am Soc Nephrol* **3**, 131–139 (2008).

28.    Young, M. F. Skeletal biology: Where matrix meets mineral. *Matrix Biol.* **52–54**, 1–6 (2016).

29.    Silva, A., Anderson, A. & Gatenby, R. A multiscale model of the bone marrow and hematopoiesis. in *Mathematical Biosciences and Engineering* **8**, 643–658 (NIH Public Access, 2011).

30.    Gentili, C. & Cancedda, R. Cartilage and Bone Extracellular Matrix. *Curr. Pharm. Des.* **15**, 1334–1348 (2009).

31.    Florencio-silva, R.; Sasso, G.; Sasso-cerri, E.; Simões, M. J. & Cerri, P. S. Biology of Bone Tissue: Structure, Function, and Factors That Influence Bone Cells. *Biomed Res. Int.* **2015**, 1–17 (2015).

32.    Su, N. *et al.* Bone function, dysfunction and its role in diseases including critical illness. *International Journal of Biological Sciences* **15**, 776–787 (2019).

33.    Shah, F. A., Thomsen, P. & Palmquist, A. Osseointegration and current interpretations of the bone-

implant interface. *Acta Biomater.* **84**, 1–15 (2019).

34.    Rho, J. Y., Kuhn-Spearing, L. & Zioupos, P. Mechanical properties and the hierarchical structure of bone. *Med. Eng. Phys.* **20**, 92–102 (1998).

35.    Reznikov, N., Shahar, R. & Weiner, S. Bone hierarchical structure in three dimensions q. (2014). doi:10.1016/j.actbio.2014.05.024

36.    Kim, D., Lee, B., Thomopoulos, S. & Jun, Y. S. The role of confined collagen geometry in decreasing nucleation energy barriers to intrafibrillar mineralization. *Nat. Commun.* **9**, 1–9 (2018).

37.    Kim, J. N. *et al.* Haversian system of compact bone and comparison between endosteal and periostealsides using three-dimensional reconstructionin rat. *Anat. Cell Biol.* **48**, 258–261 (2015).

38.    Bonewald, L. F. The amazing osteocyte. *J. Bone Miner. Res.* **26**, 229–238 (2011).

39.    Nicolella, D. P., Moravits, D. E., Gale, A. M., Bonewald, L. F. & Lankford, J. Osteocyte lacunae tissue strain in cortical bone. *J. Biomech.* **39**, 1735–1743 (2006).

40.    Osterhoff, G. *et al.* Bone mechanical properties and changes with osteoporosis. *Injury* **47**, S11–S20 (2016).

41.    Rutkovskiy, A., Stensløkken, K.-O. & Vaage, I. J. Osteoblast Differentiation at a Glance. *Med. Sci. Monit. Basic Res.* **22**, 95–106 (2016).

42.    Steens, J. & Klein, D. Current strategies to generate human mesenchymal stem cells in vitro. *Stem Cells Int.* **2018**, (2018).

43.    Sordi, V. *et al.* Mesenchymal cells appearing in pancreatic tissue culture are bone marrow-derived stem cells with the capacity to improve transplanted islet function. *Stem Cells* **28**, 140–151 (2010).

44.    Haasters, F. *et al.* Morphological and immunocytochemical characteristics indicate the yield of early progenitors and represent a quality control for human mesenchymal stem cell culturing. *J. Anat.* **214**, 759–767 (2009).

45.    Ge, J. *et al.* The Size of Mesenchymal Stem Cells is a Significant Cause of Vascular Obstructions and Stroke. *Stem Cell Rev. Reports* **10**, 295–303 (2014).

46.    Ng, C. P. *et al.* Enhanced exvivo expansion of adult mesenchymal stem cells by fetal mesenchymal stem cell ECM. *Biomaterials* **35**, 4046–4057 (2014).

47.    Wagner, W. *et al.* Aging and replicative senescence have related effects on human stem and progenitor cells. *PLoS One* **4**, 5846 (2009).

48.    Wagner, W., Ho, A. D. & Zenke, M. Different facets of aging in human mesenchymal stem cells. *Tissue Engineering - Part B: Reviews* **16**, 445–453 (2010).

49.    Uccelli, A., Moretta, L. & Pistoia, V. Mesenchymal stem cells in health and disease. *Nature Reviews Immunology* **8**, 726–736 (2008).

50. Garg, P. *et al.* Prospective Review of Mesenchymal Stem Cells Differentiation into Osteoblasts. *Orthop. Surg.* **9**, 13–19 (2017).

51. Tondreau, T. *et al.* Isolation of BM mesenchymal stem cells by plastic adhesion or negative selection: Phenotype, proliferation kinetics and differentiation potential. *Cytotherapy* **6**, 372–379 (2004).

52. Charbord, P. Bone marrow mesenchymal stem cells: Historical overview and concepts. *Human Gene Therapy* **21**, 1045–1056 (2010).

53. Samsonraj, R. M. *et al.* Concise Review: Multifaceted Characterization of Human Mesenchymal Stem Cells for Use in Regenerative Medicine. *Stem Cells Translational Medicine* **6**, 2173–2185 (2017).

54. Yang, Y. Q. *et al.* The role of vascular endothelial growth factor in ossification. *International Journal of Oral Science* **4**, 64–68 (2012).

55. Biezklan, J. P. *Principles of Bone Biology SECOND EDITION.*

56. Kohli, N. *et al.* Bone remodelling in vitro: Where are we headed?: -A review on the current understanding of physiological bone remodelling and inflammation and the strategies for testing biomaterials in vitro. *Bone* **110**, 38–46 (2018).

57. Dallas, S. L., Prideaux, M. & Bonewald, L. F. The osteocyte: An endocrine cell . . . and more. *Endocr. Rev.* **34**, 658–690 (2013).

58. Loi, F. *et al.* Inflammation, fracture and bone repair. *Bone* **86**, 119–130 (2016).

59. Eriksen, E. F. Cellular mechanisms of bone remodeling. *Rev. Endocr. Metab. Disord.* **11**, 219–227 (2010).

60. Owen, R. & Reilly, G. C. In vitro Models of Bone Remodelling and Associated Disorders. *Front. Bioeng. Biotechnol.* **6**, 134 (2018).

61. Blair, H. C. *et al.* Osteoblast differentiation and bone matrix formation in vivo and in vitro. *Tissue Engineering - Part B: Reviews* **23**, 268–280 (2017).

62. Cui, L., Houston, D. A., Farquharson, C. & Macrae, V. E. Characterisation of matrix vesicles in skeletal and soft tissue mineralisation. *Bone* **87**, 147–158 (2016).

63. Boonrungsiman, S. *et al.* The role of intracellular calcium phosphate in osteoblast-mediated bone apatite formation. doi:10.1073/pnas.1208916109

64. Sims, N. A. & Gooi, J. H. Bone remodeling: Multiple cellular interactions required for coupling of bone formation and resorption. *Seminars in Cell and Developmental Biology* **19**, 444–451 (2008).

65. Xiong, J. & O'Brien, C. A. Osteocyte RANKL: New insights into the control of bone remodeling. *J. Bone Miner. Res.* **27**, 499–505 (2012).

66. Sohni, A. & Verfaillie, C. M. Mesenchymal stem cells migration homing and tracking. *Stem Cells Int.* **2013**, (2013).

67.    Yoon, D. *et al.* Study on chemotaxis and chemokinesis of bone marrow-derived mesenchymal stem cells in hydrogel-based 3D microfluidic devices. *Biomater. Res.* **20**, (2016).

68.    Karp, J. M. & Leng Teo, G. S. Mesenchymal Stem Cell Homing: The Devil Is in the Details. *Cell Stem Cell* **4**, 206–216 (2009).

69.    Nitzsche, F. *et al.* Concise Review: MSC Adhesion Cascade-Insights into Homing and Transendothelial Migration. *Stem Cells* **35**, 1446–1460 (2017).

70.    Steingen, C. *et al.* Characterization of key mechanisms in transmigration and invasion of mesenchymal stem cells. *J. Mol. Cell. Cardiol.* **44**, 1072–1084 (2008).

71.    De Becker, A. *et al.* Migration of culture-expanded human mesenchymal stem cells through bone marrow endothelium is regulated by matrix metalloproteinase-2 and tissue inhibitor of metalloproteinase-3. *Haematologica* **92**, 440–449 (2007).

72.    Geiger, B., Spatz, J. P. & Bershadsky, A. D. Environmental sensing through focal adhesions. *Nat. Rev. Mol. Cell Biol.* **10**, 21–33 (2009).

73.    Biggs, M. J. P. *et al.* Adhesion formation of primary human osteoblasts and the functional response of mesenchymal stem cells to 330 nm deep microgrooves. *J. R. Soc. Interface* **5**, 1231–1242 (2008).

74.    Byron, A., Morgan, M. R. & Humphries, M. J. *Adhesion signalling complexes*. (2010). doi:10.1016/j.cub.2010.10.059

75.    King, S. J. *et al.* Lamellipodia are crucial for haptotactic sensing and response. *J. Cell Sci.* **129**, 2329–2342 (2016).

76.    Anderson, H. J., Sahoo, J. K., Ulijn, R. V. & Dalby, M. J. Mesenchymal Stem Cell Fate: Applying Biomaterials for Control of Stem Cell Behavior. *Front. Bioeng. Biotechnol.* **4**, 1–14 (2016).

77.    Wilkinson, A. *et al.* Biomimetic microtopography to enhance osteogenesis in vitro. *Acta Biomater.* **7**, 2919–2925 (2011).

78.    Mathieu, P. S. & Loboa, E. G. Cytoskeletal and focal adhesion influences on mesenchymal stem cell shape, mechanical properties, and differentiation down osteogenic, adipogenic, and chondrogenic pathways. *Tissue Eng. - Part B Rev.* **18**, 436–444 (2012).

79.    Pellegrin, S. & Mellor, H. Actin stress fibers. *J. Cell Sci.* **120**, 3491–3499 (2007).

80.    Sjöström, T., McNamara, L. E., Meek, R. M. D., Dalby, M. J. & Su, B. 2D and 3D Nanopatterning of Titanium for Enhancing Osteoinduction of Stem Cells at Implant Surfaces. *Adv. Healthc. Mater.* **2**, 1285–1293 (2013).

81.    McNamara, L. E. *et al.* Investigation of the limits of nanoscale filopodial interactions. *J. Tissue Eng.* **5**, 204173141453617 (2014).

82.    Yamada, K. M., Pankov, R. & Cukierman, E. Dimensions and dynamics in integrin function. *Brazilian J. Med. Biol. Res.* **36**, 959–966 (2003).

83. Krause, M. & Gautreau, A. Steering cell migration: Lamellipodium dynamics and the regulation of directional persistence. *Nature Reviews Molecular Cell Biology* **15**, 577–590 (2014).

84. Paluch, E. K., Aspalter, I. M. & Sixt, M. Focal Adhesion–Independent Cell Migration. *Annu. Rev. Cell Dev. Biol.* **32**, 469–490 (2016).

85. Petrie, R. J., Doyle, A. D. & Yamada, K. M. Random versus directionally persistent cell migration. *Nature Reviews Molecular Cell Biology* **10**, 538–549 (2009).

86. Friedl, P. & Wolf, K. Plasticity of cell migration: A multiscale tuning model. *Journal of Cell Biology* **188**, 11–19 (2010).

87. Su, P. *et al.* Mesenchymal stem cell migration during bone formation and bone diseases therapy. *International Journal of Molecular Sciences* **19**, 2343 (2018).

88. Talkenberger, K., Ada Cavalcanti-Adam, E., Voss-Böhme, A. & Deutsch, A. Amoeboid-mesenchymal migration plasticity promotes invasion only in complex heterogeneous microenvironments. *Sci. Rep.* **7**, 1–12 (2017).

89. Yip, A. K., Chiam, K. H. & Matsudaira, P. Traction stress analysis and modeling reveal that amoeboid migration in confined spaces is accompanied by expansive forces and requires the structural integrity of the membrane-cortex interactions. *Integr. Biol. (United Kingdom)* **7**, 1196–1211 (2015).

90. Kim, T., See, C. W., Li, X. & Zhu, D. Orthopedic implants and devices for bone fractures and defects: Past, present and perspective. *Eng. Regen.* **1**, 6–18 (2020).

91. Fousová, M., Kubásek, J., Machová, M., Vojtěch, D. & Dvorský, D. Preparation of composite material with continuous network of MgF2 by powder metallurgy View project 3D printing as an alternative to casting, forging and machining technologies? (2016). doi:10.21062/ujep/x.2015/a/1213-2489/MT/15/5/809

92. Wysocki, B. *et al.* Laser and Electron Beam Additive Manufacturing Methods of Fabricating Titanium Bone Implants. *Appl. Sci.* **7**, 657 (2017).

93. Bertol, L. S., Júnior, W. K., Silva, F. P. da & Aumund-Kopp, C. Medical design: Direct metal laser sintering of Ti-6Al-4V. *Mater. Des.* **31**, 3982–3988 (2010).

94. Dehghanghadikolaei, A. & Fotovvati, B. Coating techniques for functional enhancement of metal implants for bone replacement: A review. *Materials* **12**, 1795 (2019).

95. Chen, X., Zhang, B., Gong, Y., Zhou, P. & Li, H. Mechanical properties of nanodiamond-reinforced hydroxyapatite composite coatings deposited by suspension plasma spraying. *Appl. Surf. Sci.* **439**, 60–65 (2018).

96. Jones, J. R. *et al.* Bioactive glass scaffolds for bone regeneration and their hierarchical characterisation. in *Proceedings of the Institution of Mechanical Engineers, Part H: Journal of Engineering in Medicine* **224**, 1373–1387 (Proc Inst Mech Eng H, 2010).

97. Uchida, A., Nade, S. M. L., McCartney, E. R. & Ching, W. The use of ceramics for bone replacement. A

comparative study of three different porous ceramics. *J. Bone Jt. Surg. - Ser. B* **66**, 269–275 (1984).

98.  Purnomo, Hadi Setyarini, P. & Hidayati Mukaromah, A. The potential of silk fibroin as a polymer composite reinforcement for bone implant materials. *MATEC Web Conf.* **204**, 05017 (2018).

99.  Pandey, A., Awasthi, A. & Saxena, K. K. Metallic implants with properties and latest production techniques: a review. *Advances in Materials and Processing Technologies* **6**, 167–202 (2020).

100. Pacheco, K. A. Allergy to Surgical Implants. *Clinical Reviews in Allergy and Immunology* **56**, 72–85 (2019).

101. Davis, J. *Handbook of Materials for Medical Devices*. *ASM International* (2003).

102. Disegi, J. A., Kenned, R. L. & Pilliar, R. *Cobalt-Base Alloys for Biomedical Applications*. (1999).

103. Liao, Y. *et al.* CoCrMo metal-on-metal hip replacements. *Physical Chemistry Chemical Physics* **15**, 746–756 (2013).

104. Hanawa, T. Research and development of metals for medical devices based on clinical needs. *Sci. Technol. Adv. Mater.* **13**, 064102 (2012).

105. Pan, J., Leygraf, C., Thierry, D. & Ektessabi, A. M. Corrosion resistance for biomaterial applications of TiO2 films deposited on titanium and stainless steel by ion-beam-assisted sputtering. *J. Biomed. Mater. Res.* **35**, 309–318 (1997).

106. Elias, C. N., Lima, J. H. C., Valiev, R. & Meyers, M. A. Biomedical applications of titanium and its alloys. *JOM* **60**, 46–49 (2008).

107. Murr, L. E. *et al.* Microstructure and mechanical behavior of Ti-6Al-4V produced by rapid-layer manufacturing, for biomedical applications. *Journal of the Mechanical Behavior of Biomedical Materials* **2**, 20–32 (2009).

108. Boehlert, C. J., Cowen, C. J., Quast, J. P., Akahori, T. & Niinomi, M. Fatigue and wear evaluation of Ti-Al-Nb alloys for biomedical applications. *Mater. Sci. Eng. C* **28**, 323–330 (2008).

109. Klein, G. L. Aluminum toxicity to bone: A multisystem effect? *Osteoporos. Sarcopenia* **5**, 2–5 (2019).

110. Siemers, C., Bäker, M., Brunke, F., Wolter, D. & Sibum, H. Aluminum- and vanadium-free titanium alloys for application in medical engineering. in *Titanium in Medical and Dental Applications* 477–492 (Elsevier, 2018). doi:10.1016/B978-0-12-812456-7.00021-4

111. Kolli, R. P. & Devaraj, A. A review of metastable beta titanium alloys. *Metals* **8**, 506 (2018).

112. Li, Y. *et al.* New Developments of Ti-Based Alloys for Biomedical Applications. *Materials (Basel).* **7**, 1709–1800 (2014).

113. Ridzwan, M. I. Z., Shuib, S., Hassan, A. Y., Shokri, A. A. & Mohammad Ibrahim, M. N. Problem of stress shielding and improvement to the hip implant designs: A review. *Journal of Medical Sciences* **7**, 460–467 (2007).

114. Teichtahl, A. J. *et al.* Wolff's law in action: A mechanism for early knee osteoarthritis. *Arthritis Research and Therapy* **17**, (2015).

115. Pałka, K. & Pokrowiecki, R. Porous Titanium Implants: A Review. *Adv. Eng. Mater.* **20**, 1700648 (2018).

116. Song, Y. *et al.* Theoretical study of the effects of alloying elements on the strength and modulus of β-type bio-titanium alloys. *Mater. Sci. Eng. A* **260**, 269–274 (1999).

117. Cotton, J. D. *et al.* State of the Art in Beta Titanium Alloys for Airframe Applications. *JOM* **67**, 1281–1303 (2015).

118. İzmir, M. & Ercan, B. Anodization of titanium alloys for orthopedic applications. doi:10.1007/s11705-018-1759-y

119. Tomomichi Ozaki, Hiroaki Matsumoto, S. W. and S. H. Beta Ti Alloys with Low Young's Modulus. *Mater. Trans. Vol.45 No.08* **45**, pp.2776-2779 (2004).

120. Helth, A. *et al.* Effect of thermomechanical processing on the mechanical biofunctionality of a low modulus Ti-40Nb alloy. *J. Mech. Behav. Biomed. Mater.* **65**, 137–150 (2017).

121. Joshi, V. S., Lei, N. Y., Walthers, C. M., Wu, B. & Dunn, J. C. Y. Macroporosity enhances vascularization of electrospun scaffolds. *J. Surg. Res.* **183**, 18–26 (2013).

122. Abbasi, N., Hamlet, S., Love, R. M. & Nguyen, N. T. Porous scaffolds for bone regeneration. *Journal of Science: Advanced Materials and Devices* **5**, 1–9 (2020).

123. Zhuravleva, K. *et al.* Determination of the Young's modulus of porous ß-type Ti-40Nb by finite element analysis. *Mater. Des.* **64**, 1–8 (2014).

124. Chiu, Y. C. *et al.* The role of pore size on vascularization and tissue remodeling in PEG hydrogels. *Biomaterials* **32**, 6045–6051 (2011).

125. Taniguchi, N. *et al.* Effect of pore size on bone ingrowth into porous titanium implants fabricated by additive manufacturing: An in vivo experiment. *Mater. Sci. Eng. C* **59**, 690–701 (2016).

126. Sadat-Shojai, M., Khorasani, M. T., Dinpanah-Khoshdargi, E. & Jamshidi, A. Synthesis methods for nanosized hydroxyapatite with diverse structures. *Acta Biomater.* **9**, 7591–7621 (2013).

127. Bohner, M. *et al.* Characterization and distribution of mechanically competent mineralized tissue in micropores of β-tricalcium phosphate bone substitutes. *Mater. Today* **20**, 106–115 (2017).

128. Barfeie, A., Wilson, J. & Rees, J. Implant surface characteristics and their effect on osseointegration. *British Dental Journal* **218**, E9–E9 (2015).

129. Kyburz, K. A. & Anseth, K. S. Synthetic Mimics of the Extracellular Matrix: How Simple is Complex Enough? *Ann. Biomed. Eng.* **43**, 489–500 (2015).

130. Chouirfa, H., Bouloussa, H., Migonney, V. & Falentin-Daudré, C. Review of titanium surface modification techniques and coatings for antibacterial applications. *Acta Biomaterialia* **83**, 37–54 (2019).

131.    Stewart, C., Akhavan, B., Wise, S. G. & Bilek, M. M. M. A review of biomimetic surface functionalization for bone-integrating orthopedic implants: Mechanisms, current approaches, and future directions. *Progress in Materials Science* **106**, 100588 (2019).

132.    Liu, X., Chu, P. K. & Ding, C. Surface modification of titanium, titanium alloys, and related materials for biomedical applications. *Materials Science and Engineering R: Reports* **47**, 49–121 (2004).

133.    Wang, Y., Yu, H., Chen, C. & Zhao, Z. Review of the biocompatibility of micro-arc oxidation coated titanium alloys. *Mater. Des.* **85**, 640–652 (2015).

134.    Arango-Santander, S., Pelaez-Vargas, A., Freitas, S. C. & García, C. A novel approach to create an antibacterial surface using titanium dioxide and a combination of dip-pen nanolithography and soft lithography. *Sci. Rep.* **8**, 1–10 (2018).

135.    Wang, G. *et al.* Surface thermal oxidation on titanium implants to enhance osteogenic activity and in vivo osseointegration. *Sci. Rep.* **6**, 1–13 (2016).

136.    Gebert, A. *et al.* Oxidation treatments of beta-type Ti-40Nb for biomedical use. *Surf. Coatings Technol.* **302**, 88–99 (2016).

137.    Nagaoka, A., Yokoyama, K. & Sakai, J. Evaluation of hydrogen absorption behaviour during acid etching for surface modification of commercial pure Ti, Ti-6Al-4V and Ni-Ti superelastic alloys. *Corros. Sci.* **52**, 1130–1138 (2010).

138.    Lei, Z. *et al.* Antibacterial activities and biocompatibilities of Ti-Ag alloys prepared by spark plasma sintering and acid etching. *Mater. Sci. Eng. C* **92**, 121–131 (2018).

139.    Paredes, V., Salvagni, E., Rodríguez-Castellón, E. & Manero, J. M. Comparative Study of Surface Chemical Composition and Oxide Layer Modification upon Oxygen Plasma Cleaning and Piranha Etching on a Novel Low Elastic Modulus Ti25Nb21Hf Alloy. *Metall. Mater. Trans. A Phys. Metall. Mater. Sci.* **48**, 3770–3776 (2017).

140.    Hung, K. Y., Lin, Y. C. & Feng, H. P. The effects of acid etching on the nanomorphological surface characteristics and activation energy of titanium medical materials. *Materials (Basel).* **10**, (2017).

141.    Lavenus, S., Louarn, G. & Layrolle, P. Nanotechnology and Dental Implants. *Int. J. Biomater.* **2010**, 1–9 (2010).

142.    MacDonald, D. E. *et al.* Thermal and chemical modification of titanium-aluminum-vanadium implant materials: Effects on surface properties, glycoprotein adsorption, and MG63 cell attachment. *Biomaterials* **25**, 3135–3146 (2004).

143.    Zahran, R., Rosales Leal, J. I., Rodríguez Valverde, M. A. & Cabrerizo Vílchez, M. A. Effect of hydrofluoric acid etching time on titanium topography, chemistry, wettability, and cell adhesion. *PLoS One* **11**, (2016).

144.    Helth, A. *et al.* Chemical nanoroughening of Ti40Nb surfaces and its effect on human mesenchymal stromal cell response. *J. Biomed. Mater. Res. - Part B Appl. Biomater.* **102**, 31–41 (2014).

145. Jarosz, M. *et al.* Anodization of titanium alloys for biomedical applications. in *Nanostructured Anodic Metal Oxides* 211–275 (Elsevier, 2020). doi:10.1016/b978-0-12-816706-9.00007-8

146. Lohrengel, M. M. Formation of ionic space charge layers in oxide films on valve metals. *Electrochim. Acta* **39**, 1265–1271 (1994).

147. Zhang, S., Qin, J., Yang, C., Zhang, X. & Liu, R. Effect of Zr addition on the microstructure and tribological property of the anodization of Ti-6Al-4V alloy. *Surf. Coatings Technol.* **356**, 38–48 (2018).

148. Minagar, S., Berndt, C. C., Wang, J., Ivanova, E. & Wen, C. A review of the application of anodization for the fabrication of nanotubes on metal implant surfaces. *Acta Biomaterialia* **8**, 2875–2888 (2012).

149. Bauer, S., Kleber, S. & Schmuki, P. TiO2 nanotubes: Tailoring the geometry in H3PO4/HF electrolytes. *Electrochem. commun.* **8**, 1321–1325 (2006).

150. Alford, A. I., Kozloff, K. M. & Hankenson, K. D. Extracellular matrix networks in bone remodeling. *International Journal of Biochemistry and Cell Biology* **65**, 20–31 (2015).

151. Lin, X., Patil, S., Gao, Y. G. & Qian, A. The Bone Extracellular Matrix in Bone Formation and Regeneration. *Frontiers in Pharmacology* **11**, (2020).

152. Breme, J., Zhou, Y. & Groh, L. Development of a titanium alloy suitable for an optimized coating with hydroxyapatite. *Biomaterials* **16**, 239–244 (1995).

153. Sartori, M. *et al.* Collagen type I coating stimulates bone regeneration and osteointegration of titanium implants in the osteopenic rat. *Int. Orthop.* **39**, 2041–2052 (2015).

154. Elmengaard, B., Bechtold, J. E. & Søballe, K. In vivo study of the effect of RGD treatment on bone ongrowth on press-fit titanium alloy implants. *Biomaterials* **26**, 3521–3526 (2005).

155. Rammelt, S. *et al.* In vivo effects of coating loaded and unloaded Ti implants with collagen, chondroitin sulfate, and hydroxyapatite in the sheep tibia. *J. Orthop. Res.* **25**, 1052–1061 (2007).

156. Arcos, D. & Vallet-Regí, M. Substituted hydroxyapatite coatings of bone implants. *Journal of Materials Chemistry B* **8**, 1781–1800 (2020).

157. Hirota, M. *et al.* Hydroxyapatite coating for titanium fibre mesh scaffold enhances osteoblast activity and bone tissue formation. *Int. J. Oral Maxillofac. Surg.* **41**, 1304–1309 (2012).

158. Sverzut, A. T. *et al.* Effects of type I collagen coating on titanium osseointegration: Histomorphometric, cellular and molecular analyses. *Biomed. Mater.* **7**, 35007–35014 (2012).

159. Civantos, A. *et al.* Titanium Coatings and Surface Modifications: Toward Clinically Useful Bioactive Implants. *ACS Biomaterials Science and Engineering* **3**, 1245–1261 (2017).

160. Medda, R. *et al.* Investigation of early cell - Surface interactions of human mesenchymal stem cells on nanopatterned β-type titanium - Niobium alloy surfaces. *Interface Focus* **4**, (2014).

161. Tibbitt, M. W. & Anseth, K. S. Hydrogels as extracellular matrix mimics for 3D cell culture. *Biotechnol. Bioeng.* **103**, 655–663 (2009).

162.    Khan, M., Mao, S., Li, W. & Lin, J. Microfluidic Devices in the Fast-Growing Domain of Single-Cell Analysis. *Chem. – A Eur. J.* **24**, 15398–15420 (2018).

163.    Nikolova, M. P. & Chavali, M. S. Recent advances in biomaterials for 3D scaffolds: A review. *Bioact. Mater.* **4**, 271–292 (2019).

164.    Gough, J. E., Jones, J. R. & Hench, L. L. Nodule formation and mineralisation of human primary osteoblasts cultured on a porous bioactive glass scaffold. *Biomaterials* **25**, 2039–2046 (2004).

165.    Miyoshi, H. & Adachi, T. Topography design concept of a tissue engineering scaffold for controlling cell function and fate through actin cytoskeletal modulation. *Tissue Engineering - Part B: Reviews* **20**, 609–627 (2014).

166.    Jang, K., Sato, K., Igawa, K., Chung, U. Il & Kitamori, T. Development of an osteoblast-based 3D continuous-perfusion microfluidic system for drug screening. *Anal. Bioanal. Chem.* **390**, 825–832 (2008).

167.    Naskar, S., Kumaran, V. & Basu, B. Reprogramming the Stem Cell Behavior by Shear Stress and Electric Field Stimulation: Lab-on-a-Chip Based Biomicrofluidics in Regenerative Medicine. *Regen. Eng. Transl. Med.* 1–29 (2018). doi:10.1007/s40883-018-0071-1

168.    Saadatpour, A., Lai, S., Guo, G. & Yuan, G.-C. Single-cell analysis in cancer genomics. *Trends Genet.* **31**, 576 (2015).

169.    Jonathan Avesar, Ben Arye, T. & Shulamit Levenberg. Frontier microfluidic techniques for short and long-term single cell analysis. *Lab Chip* **14**, 2161–2167 (2014).

170.    Lindström, S. & Andersson-Svahn, H. Overview of single-cell analyses: Microdevices and applications. *Lab on a Chip* **10**, 3363–3372 (2010).

171.    Ting Zheng, X. & Ming Li, C. Single cell analysis at the nanoscale. *Chem. Soc. Rev.* **41**, 2061–2071 (2012).

172.    C, Y. *et al.* Cavity Carbon-Nanopipette Electrodes for Dopamine Detection. *Anal. Chem.* **91**, 4618–4624 (2019).

173.    Hochmuth, R. M. Micropipette aspiration of living cells. *J. Biomech.* **33**, 15–22 (2000).

174.    Stanley, J. & Pourmand, N. Nanopipettes—The past and the present. *APL Mater.* **8**, 100902 (2020).

175.    Devroey, P. & Van Steirteghem, A. A review of ten years experience of ICSI. *Hum. Reprod. Update* **10**, 19–28 (2004).

176.    Y, C. *et al.* Nondestructive nanostraw intracellular sampling for longitudinal cell monitoring. *Proc. Natl. Acad. Sci. U. S. A.* **114**, E1866–E1874 (2017).

177.    Actis, P. *et al.* Compartmental Genomics in Living Cells Revealed by Single-Cell Nanobiopsy. *ACS Nano* **8**, 546 (2014).

178.    Loh, O. *et al.* Nanofountain-probe-based high-resolution patterning and single-cell injection of

functionalized nanodiamonds. *Small* **5**, 1667–1674 (2009).

179. JP, S., MK, G., V, S. & T, V.-D. SERS-based plasmonic nanobiosensing in single living cells. *Anal. Bioanal. Chem.* **393**, 1135–1141 (2008).

180. Gao, R., Cui, L.-F., Ruan, L.-Q., Ying, Y.-L. & Long, Y.-T. A Closed-Type Wireless Nanopore Electrode for Analyzing Single Nanoparticles. *JoVE (Journal Vis. Exp.* e59003 (2019). doi:10.3791/59003

181. Yang, D. *et al.* The fabrication of a gold nanoelectrode–nanopore nanopipette for dopamine enrichment and multimode detection. *Analyst* **145**, 1047–1055 (2020).

182. Nebel, M., Grützke, S., Diab, N., Schulte, A. & Schuhmann, W. Microelectrochemical visualization of oxygen consumption of single living cells. *Faraday Discuss.* **164**, 19–32 (2013).

183. M, B. Advances in patch clamp technique: towards higher quality and quantity. *Gen. Physiol. Biophys.* **31**, 131–140 (2012).

184. Suk, H. J., Boyden, E. S. & van Welie, I. Advances in the automation of whole-cell patch clamp technology. *J. Neurosci. Methods* **326**, 108357 (2019).

185. Ye, B. & Ye, B. Ca 2+ Oscillations and Its Transporters in Mesenchymal Stem Cells. *Physiol. Res* **59**, 323–329 (2010).

186. Sun, J. *et al.* Fluid shear stress induces calcium transients in osteoblasts through depolarization of osteoblastic membrane. *J. Biomech.* **47**, 3903–3908 (2014).

187. Barradas, A. M. C. *et al.* A calcium-induced signaling cascade leading to osteogenic differentiation of human bone marrow-derived mesenchymal stromal cells. *Biomaterials* **33**, 3205–3215 (2012).

188. Wen, L. *et al.* L-type calcium channels play a crucial role in the proliferation and osteogenic differentiation of bone marrow mesenchymal stem cells. *Biochem. Biophys. Res. Commun.* **424**, 439–445 (2012).

189. Ma, Z., Liao, J., Zhao, C. & Cai, D. Effects of the 1, 4-dihydropyridine L-type calcium channel blocker benidipine on bone marrow stromal cells. *Cell Tissue Res. 2015 3612* **361**, 467–476 (2015).

190. Petecchia, L. *et al.* Electro-magnetic field promotes osteogenic differentiation of BM-hMSCs through a selective action on Ca2+-related mechanisms. *Sci. Reports 2015 51* **5**, 1–13 (2015).

191. Bloise, N. *et al.* The effect of pulsed electromagnetic field exposure on osteoinduction of human mesenchymal stem cells cultured on nano-TiO2 surfaces. *PLoS One* **13**, e0199046 (2018).

192. Vaughan, T. J., Mullen, C. A., Verbruggen, S. W. & McNamara, L. M. Bone cell mechanosensation of fluid flow stimulation: a fluid–structure interaction model characterising the role integrin attachments and primary cilia. *Biomech. Model. Mechanobiol.* **14**, 703–718 (2015).

193. Bancroft, G. N. *et al.* Fluid flow increases mineralized matrix deposition in 3D perfusion culture of marrow stromal osteoblasts in a dose-dependent manner. *Proc. Natl. Acad. Sci. U. S. A.* **99**, 12600–

12605 (2002).

194. Chen, G., Dong, C., Yang, L. & Lv, Y. 3D Scaffolds with Different Stiffness but the Same Microstructure for Bone Tissue Engineering. *ACS Appl. Mater. Interfaces* **7**, 15790–15802 (2015).

195. Nikkhah, M., Edalat, F., Manoucheri, S. & Khademhosseini, A. Engineering microscale topographies to control the cell-substrate interface. *Biomaterials* **33**, 5230–5246 (2012).

196. Gui, N. *et al.* Biomaterials Science REVIEW The effect of ordered and partially ordered surface topography on bone cell responses: a review. *Biomater. Sci* **6**, 250–264 (2018).

197. D, D. C., LY, W. & LP, L. Dynamic single cell culture array. *Lab Chip* **6**, 1445–1449 (2006).

198. Ruiz, S. A. & Chen, C. S. Microcontact printing: A tool to pattern. *Soft Matter* **3**, 168–177 (2007).

199. Röttgermann, P. J. F., Alberola, A. P. & Rädler, J. O. Cellular self-organization on micro-structured surfaces. *Soft Matter* **10**, 2397–2404 (2014).

200. Azeem, A. *et al.* The influence of anisotropic nano- to micro-topography on in vitro and in vivo osteogenesis. *Nanomedicine* **10**, 693–711 (2015).

201. Matschegewski, C. *et al.* Cell architecture–cell function dependencies on titanium arrays with regular geometry. *Biomaterials* **31**, 5729–5740 (2010).

202. Watari, S. *et al.* Modulation of osteogenic differentiation in hMSCs cells by submicron topographically-patterned ridges and grooves. *Biomaterials* **33**, 128–136 (2012).

203. Ahn, E. H. *et al.* Spatial control of adult stem cell fate using nanotopographic cues. *Biomaterials* **35**, 2401–2410 (2014).

204. Sjöström, T. *et al.* Fabrication of pillar-like titania nanostructures on titanium and their interactions with human skeletal stem cells. *Acta Biomater.* **5**, 1433–1441 (2009).

205. Pina, S., Oliveira, J. M. & Reis, R. L. Natural-Based Nanocomposites for Bone Tissue Engineering and Regenerative Medicine: A Review. *Adv. Mater.* **27**, 1143–1169 (2015).

206. Yue, S., He, H., Li, B. & Hou, T. Hydrogel as a Biomaterial for Bone Tissue Engineering: A Review. *Nanomaterials* **10**, 1511 (2020).

207. Castiaux, A. D., Spence, D. M. & Martin, R. S. Review of 3D cell culture with analysis in microfluidic systems. *Analytical Methods* **11**, 4220–4232 (2019).

208. Bodenberger, N. *et al.* Evaluation of methods for pore generation and their influence on physio-chemical properties of a protein based hydrogel. *Biotechnol. Reports* **12**, 6–12 (2016).

209. Tozzi, G., De Mori, A., Oliveira, A. & Roldo, M. Composite hydrogels for bone regeneration. *Materials* **9**, 267 (2016).

210. H, H. Modified fibrin hydrogel matrices: both, 3D-scaffolds and local and controlled release systems to stimulate angiogenesis. *Curr. Pharm. Des.* **13**, 3597–3607 (2007).

211. Distler, T. & Boccaccini, A. R. 3D printing of electrically conductive hydrogels for tissue engineering and biosensors – A review. *Acta Biomater.* **101**, 1–13 (2020).

212. Wang, X. *et al.* Role of integrin α2β1 in mediating osteoblastic differentiation on three-dimensional titanium scaffolds with submicron-scale texture. *J. Biomed. Mater. Res. - Part A* **103**, 1907–1918 (2015).

213. Lo, Y. P. *et al.* Three-dimensional spherical spatial boundary conditions differentially regulate osteogenic differentiation of mesenchymal stromal cells. *Sci. Rep.* **6**, 1–14 (2016).

214. Bongio, M., Lopa, S., Gilardi, M., Bersini, S. & Moretti, M. A 3D vascularized bone remodeling model combining osteoblasts and osteoclasts in a CaP nanoparticle-enriched matrix. *Nanomedicine* **11**, 1073–1091 (2016).

215. Marino, A., Filippeschi, C., Mattoli, V., Mazzolai, B. & Ciofani, G. Biomimicry at the nanoscale: current research and perspectives of two-photon polymerization. *Nanoscale* **7**, 2841–2850 (2015).

216. Marino, A. *et al.* The Osteoprint: A bioinspired two-photon polymerized 3-D structure for the enhancement of bone-like cell differentiation. *Acta Biomater.* **10**, 4304–4313 (2014).

217. Nune, K. C., Misra, R. D. K., Li, S. J., Hao, Y. L. & Yang, R. Cellular response of osteoblasts to low modulus Ti-24Nb-4Zr-8Sn alloy mesh structure. *J. Biomed. Mater. Res. Part A* **105**, 859–870 (2017).

218. Nune, K., Misra, R., Gai, X., Li, S. & Hao, Y. Surface nanotopography-induced favorable modulation of bioactivity and osteoconductive potential of anodized 3D printed Ti-6Al-4V alloy mesh structure: *https://doi.org/10.1177/0885328217748860* **32**, 1032–1048 (2017).

219. Chang, B. *et al.* Influence of pore size of porous titanium fabricated by vacuum diffusion bonding of titanium meshes on cell penetration and bone ingrowth. *Acta Biomater.* **33**, 311–321 (2016).

220. Mushtaq, F. *et al.* Magnetoelectric 3D scaffolds for enhanced bone cell proliferation. *Appl. Mater. Today* **16**, 290–300 (2019).

221. Murphy, T. W., Zhang, Q., Naler, L. B., Ma, S. & Lu, C. Recent advances in the use of microfluidic technologies for single cell analysis. *Analyst* **143**, 60–80 (2018).

222. Wyatt Shields Iv, C., Reyes, C. D. & López, G. P. Microfluidic cell sorting: A review of the advances in the separation of cells from debulking to rare cell isolation. *Lab Chip* **15**, 1230–1249 (2015).

223. Shen, Y., Yalikun, Y. & Tanaka, Y. Recent advances in microfluidic cell sorting systems. *Sensors and Actuators, B: Chemical* **282**, 268–281 (2019).

224. Yeo, L. Y., Chang, H.-C., Chan, P. P. Y. & Friend, J. R. Microfluidic Devices for Bioapplications. *Small* **7**, 12–48 (2011).

225. Whitesides, G. M., Ostuni, E., Takayama, S., Jiang, X. & Ingber, D. E. Soft Lithography in Biology and Biochemistry. *Annu. Rev. Biomed. Eng.* **3**, 335–373 (2003).

226. Karimi, A., Yazdi, S. & Ardekani, A. M. Hydrodynamic mechanisms of cell and particle trapping in microfluidics. *Biomicrofluidics* **7**, 021501 (2013).

227. Narayanamurthy, V., Nagarajan, S., Khan, A. Y. F., Samsuri, F. & Sridhar, T. M. Microfluidic hydrodynamic trapping for single cell analysis: mechanisms, methods and applications. *Anal. Methods* **9**, 3751–3772 (2017).

228. Nicholas M. Toriello, †, Erik S. Douglas, † and & Mathies*, R. A. Microfluidic Device for Electric Field-Driven Single-Cell Capture and Activation. *Anal. Chem.* **77**, 6935–6941 (2005).

229. Pethig, R. Review Article—Dielectrophoresis: Status of the theory, technology, and applications. *Biomicrofluidics* **4**, 022811 (2010).

230. Shafiee, H., Caldwell, J. L., Sano, M. B. & Davalos, R. V. Contactless dielectrophoresis: a new technique for cell manipulation. *Biomed. Microdevices 2009 115* **11**, 997–1006 (2009).

231. Jaeger, M. S., Uhlig, K., Schnelle, T. & Mueller, T. Contact-free single-cell cultivation by negative dielectrophoresis. *J. Phys. D. Appl. Phys.* **41**, 175502 (2008).

232. Carey, T. R., Cotner, K. L., Li, B. & Sohn, L. L. Developments in label-free microfluidic methods for single-cell analysis and sorting. *Wiley Interdiscip. Rev. Nanomedicine Nanobiotechnology* **11**, e1529 (2019).

233. Mansoorifar, A., Gordon, R., Bergan, R. C. & Bertassoni, L. E. Bone-on-a-Chip: Microfluidic Technologies and Microphysiologic Models of Bone Tissue. *Adv. Funct. Mater.* **31**, 2006796 (2021).

234. Leppik, L., Oliveira, K. M. C., Bhavsar, M. B. & Barker, J. H. Electrical stimulation in bone tissue engineering treatments. *European Journal of Trauma and Emergency Surgery* **46**, 231–244 (2020).

235. Bischel, L. L. *et al.* A combined microfluidic coculture and multiphoton FAD analysis assay enables insight into the influence of the bone microenvironment on prostate cancer cells. *Integr. Biol. (Camb).* **6**, 627 (2014).

236. Song, H. *et al.* Identification of mesenchymal stem cell differentiation state using dual-micropore microfluidic impedance flow cytometry. *Anal. Methods* **8**, 7437–7444 (2016).

237. Hildebrandt, C., Büth, H., Cho, S., Impidjati & Thielecke, H. Detection of the osteogenic differentiation of mesenchymal stem cells in 2D and 3D cultures by electrochemical impedance spectroscopy. *J. Biotechnol.* **148**, 83–90 (2010).

238. Middleton, K., Al-Dujaili, S., Mei, X., Günther, A. & You, L. Microfluidic co-culture platform for investigating osteocyte-osteoclast signalling during fluid shear stress mechanostimulation. *J. Biomech.* (2017). doi:10.1016/j.jbiomech.2017.05.012

239. Naskar, S., Panda, A. K., Kumaran, V., Mehta, B. & Basu, B. Controlled shear flow directs osteogenesis on uhmwpe-based hybrid nanobiocomposites in a custom-designed PMMA microfluidic device. *ACS Appl. Bio Mater.* **1**, 414–435 (2018).

240. An, S., Han, S. Y. & Cho, S. W. Hydrogel-integrated Microfluidic Systems for Advanced Stem Cell Engineering. *Biochip Journal* **13**, 306–322 (2019).

241. Bersini, S. *et al.* A microfluidic 3D invitro model for specificity of breast cancer metastasis to bone.

*Biomaterials* **35**, 2454–2461 (2014).

242. Perestrelo, A. R., Águas, A. C. P., Rainer, A. & Forte, G. Microfluidic organ/body-on-a-chip devices at the convergence of biology and microengineering. *Sensors (Switzerland)* **15**, 31142–31170 (2015).

243. Pimpin, A. & Srituravanich, W. Reviews on micro- and nanolithography techniques and their applications. *Engineering Journal* **16**, 37–55 (2012).

244. Schmidt, O. G., Schmarje, N., Deneke, C., Müller, C. & Jin-Phillipp, N. -Y. Three-Dimensional Nano-objects Evolving from a Two-Dimensional Layer Technology. *Adv. Mater.* **13**, 756–759 (2001).

245. Harazim, S. M., Xi, W., Schmidt, C. K., Sanchez, S. & Schmidt, O. G. Fabrication and applications of large arrays of multifunctional rolled-up SiO/SiO 2 microtubes. *J. Mater. Chem.* **22**, 2878–2884 (2012).

246. Zakharchenko, S., Puretskiy, N., Stoychev, G., Stamm, M. & Ionov, L. Temperature controlled encapsulation and release using partially biodegradable thermo-magneto-sensitive self-rolling tubes. *Soft Matter* **6**, 2633–2636 (2010).

247. Medina-Sánchez, M. *et al.* High-performance three-dimensional tubular nanomembrane sensor for DNA detection. *Nano Lett.* **16**, 4288–4296 (2016).

248. Mönch, I. *et al.* Rolled-up magnetic sensor: Nanomembrane architecture for in-flow detection of magnetic objects. *ACS Nano* **5**, 7436–7442 (2011).

249. Zakharchenko, S., Sperling, E. & Ionov, L. Fully biodegradable self-rolled polymer tubes: A candidate for tissue engineering scaffolds. *Biomacromolecules* **12**, 2211–2215 (2011).

250. Xi, W. *et al.* Rolled-up functionalized nanomembranes as three-dimensional cavities for single cell studies. *Nano Lett.* **14**, 4197–4204 (2014).

251. Yin, Y. *et al.* Graphene-Activated Optoplasmonic Nanomembrane Cavities for Photodegradation Detection. *ACS Appl. Mater. Interfaces* **11**, 15891–15897 (2019).

252. Madani, A. *et al.* Optical microtube cavities monolithically integrated on photonic chips for optofluidic sensing. *Opt. Lett.* **42**, 486 (2017).

253. Tang, H. *et al.* Stress-Actuated Spiral Microelectrode for High-Performance Lithium-Ion Microbatteries. *Small* **16**, 2002410 (2020).

254. Koch, B. *et al.* Dimensionality of Rolled-up Nanomembranes Controls Neural Stem Cell Migration Mechanism. *Nano Lett.* **15**, 5530–5538 (2015).

255. Huang, G., Mei, Y., Thurmer, D. J., Coric, E. & Schmidt, O. G. Rolled-up transparent microtubes as two-dimensionally confined culture scaffolds of individual yeast cells. *Lab Chip* **9**, 263–268 (2009).

256. Schulze, S. *et al.* Morphological Differentiation of Neurons on Microtopographic Substrates Fabricated by Rolled-Up Nanotechnology. *Adv. Eng. Mater.* **12**, B558–B564 (2010).

257. Smith, E. J. *et al.* Lab-in-a-tube: Ultracompact components for on-chip capture and detection of individual micro-/nanoorganisms. in *Lab on a Chip* **12**, 1917–1931 (Royal Society of Chemistry, 2012).

258. Koch, B. *et al.* Confinement and Deformation of Single Cells and Their Nuclei Inside Size-Adapted Microtubes. *Adv. Healthc. Mater.* **3**, 1753–1758 (2014).

259. Xi, W. *et al.* Rolled-up functionalized nanomembranes as three-dimensional cavities for single cell studies. *Nano Lett.* **14**, 4197–4204 (2014).

260. Callens, S. J. P., Uyttendaele, R. J. C., Fratila-Apachitei, L. E. & Zadpoor, A. A. Substrate curvature as a cue to guide spatiotemporal cell and tissue organization. *Biomaterials* **232**, 119739 (2020).

261. Gupta, D., Grant, D. M., Zakir Hossain, K. M., Ahmed, I. & Sottile, V. Role of geometrical cues in bone marrow-derived mesenchymal stem cell survival, growth and osteogenic differentiation. *J. Biomater. Appl.* **32**, 906–919 (2018).

262. Lämmermann, T. *et al.* Rapid leukocyte migration by integrin-independent flowing and squeezing. *Nature* **453**, 51–55 (2008).

263. Lämmermann, T. *et al.* Neutrophil swarms require LTB4 and integrins at sites of cell death in vivo. *Nature* **498**, 371–375 (2013).

264. Liu, Y. J. *et al.* Confinement and low adhesion induce fast amoeboid migration of slow mesenchymal cells. *Cell* **160**, 659–672 (2015).

265. Ruprecht, V. *et al.* Cortical contractility triggers a stochastic switch to fast amoeboid cell motility. *Cell* **160**, 673–685 (2015).

266. Mary T. Doolin1, K. M. S. Physical confinement alters cytoskeletal contributions towards human mesenchymal stem cell migration Mary. *Cytoskeleton (Hoboken).* 1–19 (2018). doi:10.1002/cm.

267. Holle, A. W. *et al.* Cancer Cells Invade Confined Microchannels via a Self-Directed Mesenchymal-to-Amoeboid Transition. *Nano Lett.* **19**, 2280–2290 (2019).

268. Mandeville, J. T. H., Lawson, M. A. & Maxfield, F. R. Dynamic imaging of neutrophil migration in three dimensions: Mechanical interactions between cells and matrix. *J. Leukoc. Biol.* **61**, 188–200 (1997).

269. Tozluoğlu, M. *et al.* Matrix geometry determines optimal cancer cell migration strategy and modulates response to interventions. *Nat. Cell Biol.* **15**, 751–762 (2013).

270. Cattin, A. L. *et al.* Macrophage-Induced Blood Vessels Guide Schwann Cell-Mediated Regeneration of Peripheral Nerves. *Cell* **162**, 1127–1139 (2015).

271. Malawista, S. E., De Chevance, A. B. & Boxer, L. A. Random locomotion and chemotaxis of human blood polymorphonuclear leukocytes from a patient with Leukocyte Adhesion Deficiency-1: Normal displacement in close quarters via chimneying. *Cell Motil. Cytoskeleton* **46**, 183–189 (2000).

272. Hawkins, R. J. *et al.* Pushing off the walls: A mechanism of cell motility in confinement. *Phys. Rev. Lett.* **102**, 058103 (2009).

273. Yumura, S., Mori, H. & Fukui, Y. Localization of actin and myosin for the study of ameboid movement

in Dictyostelium using improved immunofluorescence. *J. Cell Biol.* **99**, 894–899 (1984).

274. Kilian, K. A., Bugarija, B., Lahn, B. T. & Mrksich, M. Geometric cues for directing the differentiation of mesenchymal stem cells. *Proc. Natl. Acad. Sci. U. S. A.* **107**, 4872–4877 (2010).

275. Engler, A. J., Sen, S., Sweeney, H. L. & Discher, D. E. Matrix Elasticity Directs Stem Cell Lineage Specification. *Cell* **126**, 677–689 (2006).

276. Werner, M. *et al.* Surface Curvature Differentially Regulates Stem Cell Migration and Differentiation via Altered Attachment Morphology and Nuclear Deformation. *Adv. Sci.* **4**, 1600347 (2017).

277. Werner, M., Petersen, A., Kurniawan, N. A. & Bouten, C. V. C. Cell-Perceived Substrate Curvature Dynamically Coordinates the Direction, Speed, and Persistence of Stromal Cell Migration. *Adv. Biosyst.* **3**, 1900080 (2019).

278. Malheiro, V., Lehner, F., Dinca, V., Hoffmann, P. & Maniura-Weber, K. Convex and concave micro-structured silicone controls the shape, but not the polarization state of human macrophages. *Biomater. Sci.* **4**, 1562–1573 (2016).

279. Foolen, J., Yamashita, T. & Kollmannsberger, P. Shaping tissues by balancing active forces and geometric constraints. *J. Phys. D. Appl. Phys.* **49**, 053001 (2015).

280. Bidan, C. M. *et al.* How linear tension converts to curvature: Geometric control of bone tissue growth. *PLoS One* **7**, 36336 (2012).

281. Bade, N. D., Kamien, R. D., Assoian, R. K. & Stebe, K. J. Curvature and Rho activation differentially control the alignment of cells and stress fibers. *Sci. Adv.* **3**, e1700150 (2017).

282. Ehrig, S. *et al.* Surface tension determines tissue shape and growth kinetics. *Sci. Adv.* **5**, 9394–9405 (2019).

283. Medina-Sánchez, M. *et al.* High-performance three-dimensional tubular nanomembrane sensor for DNA detection. *Nano Lett.* **16**, 4288–4296 (2016).

284. Berridge, M. V., Herst, P. M. & Tan, A. S. Tetrazolium dyes as tools in cell biology: New insights into their cellular reduction. *Biotechnol. Annu. Rev.* **11**, 127–152 (2005).

285. Markossian, S. *et al.* Assay Guidance Manual. *Assay Guid. Man.* (2004).

286. Hempel, U. *et al.* Human Bone Marrow Stromal Cells: A Reliable, Challenging Tool for in Vitro Osteogenesis and Bone Tissue Engineering Approaches. *Stem Cells Int.* **2016**, (2016).

287. Hempel, U. *et al.* Sulfated hyaluronan/collagen I matrices enhance the osteogenic differentiation of human mesenchymal stromal cells in vitro even in the absence of dexamethasone. *Acta Biomater.* **8**, 4064–4072 (2012).

288. Hempel, U. *et al.* Artificial extracellular matrices composed of collagen i and sulfated hyaluronan with adsorbed transforming growth factor β1 promote collagen synthesis of human mesenchymal stromal cells. *Acta Biomater.* **8**, 659–666 (2012).

289.    Porter, J. R., Ruckh, T. T. & Popat, K. C. Bone tissue engineering: A review in bone biomimetics and drug delivery strategies. *Biotechnol. Prog.* **25**, NA-NA (2009).

290.    Jirka, I. *et al.* On the role of Nb-related sites of an oxidized β-TiNb alloy surface in its interaction with osteoblast-like MG-63 cells. *Mater. Sci. Eng. C* **33**, 1636–1645 (2013).

291.    Pilz, S. *et al.* Metal release and cell biological compatibility of beta-type Ti-40Nb containing indium. *J. Biomed. Mater. Res. - Part B Appl. Biomater.* **106**, 1686–1697 (2018).

292.    Abegunde, O. O. *et al.* Overview of thin film deposition techniques. *AIMS Mater. Sci. 2019 2174* **6**, 174–199 (2019).

293.    Greene, J. E. Review Article: Tracing the recorded history of thin-film sputter deposition:        From the 1800s to 2017. *J. Vac. Sci. Technol. A Vacuum, Surfaces,        Film.* **35**, 05C204 (2017).

294.    Morintale, E., Constantinescu, C. & Dinescu, M. Thin films development by pulsed laser-assisted deposition.

295.    Lowndes, D. H., Geohegan, D. B., Puretzky, A. A., Norton, D. P. & Rouleau, C. M. Synthesis of novel thin-film materials by pulsed laser deposition. *Science (80-. ).* **273**, 898–903 (1996).

296.    M, M. S., G, V., MS, K., Sridhara, B. K. & Shridhar, T. N. Studies on Nanostructure Aluminium Thin Film Coatings Deposited using DC magnetron Sputtering Process. *IOP Conf. Ser. Mater. Sci. Eng.* **149**, 012071 (2016).

297.    Ashfold, M. N. R., Claeyssens, F., Fuge, G. M. & Henley, S. J. Pulsed laser ablation and deposition of thin films. *Chem. Soc. Rev.* **33**, 23–31 (2004).

298.    Fusi, M., Russo, V., Casari, C. S., Bassi, A. L. & Bottani, C. E. Titanium oxide nanostructured films by reactive pulsed laser deposition. *Appl. Surf. Sci.* **255**, 5334–5337 (2009).

299.    Hussain, S. N. *et al.* A Review on Wear and Corrosion Behavior of Thermal Oxidation on Titanium-based Alloy for Biomedical Application. *J. Adv. Res. Fluid Mech. Therm. Sci.* **58**, 153–160 (2019).

300.    Zorn, G., Lesman, A. & Gotman, I. Oxide formation on low modulus Ti45Nb alloy by anodic versus thermal oxidation. *Surf. Coatings Technol.* **201**, 612–618 (2006).

301.    Wen, M., Wen, C., Hodgson, P. & Li, Y. Thermal oxidation behaviour of bulk titanium with nanocrystalline surface layer. *Corros. Sci.* **59**, 352–359 (2012).

302.    Herzer, R. *et al.* Rolled-Up Metal Oxide Microscaffolds to Study Early Bone Formation at Single Cell Resolution. *Small* **17**, 2005527 (2021).

303.    Seah, M. P. A review of the analysis of surfaces and thin films by AES and XPS. *Vacuum* **34**, 463–478 (1984).

304.    Desimoni, E. & Brunetti, B. X-Ray Photoelectron Spectroscopic Characterization of Chemically Modified Electrodes Used as Chemical Sensors and Biosensors: A Review. *Chemosens. 2015, Vol. 3, Pages 70-117* **3**, 70–117 (2015).

305.     Bagus, P. S. *et al.* The interpretation of XPS spectra: Insights into materials properties. *SurSR* **68**, 273–304 (2013).

306.     Armenise, M. N. *et al.* Characterization of TiO2, LiNb3O8, and (Ti0.65Nb0.35)O2 compound growth observed during Ti:LiNbO3 optical waveguide fabrication. *J. Appl. Phys.* **54**, 6223 (1983).

307.     Helth, A. *et al.* Chemical nanoroughening of Ti40Nb surfaces and its effect on human mesenchymal stromal cell response. *J. Biomed. Mater. Res. - Part B Appl. Biomater.* **102**, 31–41 (2014).

308.     Oswald, S. *et al.* XPS and AES sputter-depth profiling at surfaces of biocompatible passivated Ti-based alloys: concentration quantification considering chemical effects. *Surf. Interface Anal.* **46**, 683–688 (2014).

309.     Elschner, C. *et al.* In vitro Response of Human Mesenchymal Stromal Cells to Titanium Coated Peek Films and Their Suitability for Magnetic Resonance Imaging. *J. Mater. Sci. Technol.* **31**, 427–436 (2015).

310.     Pieuchot, L. *et al.* Curvotaxis directs cell migration through cell-scale curvature landscapes. *Nat. Commun.* **9**, 3995 (2018).

311.     Alami, S. M., Gangloff, S. C., Laurent-Maquin, D., Wang, Y. & Kerdjoudj, H. Concise Review: In Vitro Formation of Bone-Like Nodules Sheds Light on the Application of Stem Cells for Bone Regeneration. *Stem Cells Transl. Med.* **5**, 1587 (2016).

312.     Coppola, V., Ventre, M., Natale, C. F., Rescigno, F. & Netti, P. A. On the influence of surface patterning on tissue self-assembly and mechanics. *J. Tissue Eng. Regen. Med.* **12**, 1621–1633 (2018).

313.     Baptista, D., Teixeira, L., van Blitterswijk, C., Giselbrecht, S. & Truckenmüller, R. Overlooked? Underestimated? Effects of Substrate Curvature on Cell Behavior. *Trends in Biotechnology* **37**, 838–854 (2019).

314.     Jaiswal, R. K. *et al.* Adult Human Mesenchymal Stem Cell Differentiation to the Osteogenic or Adipogenic Lineage Is Regulated by Mitogen-activated Protein Kinase. *J. Cell. Physiol.* **227**, 1680–1687 (2000).

315.     Capulli, M., Paone, R. & Rucci, N. Osteoblast and osteocyte: Games without frontiers. *Arch. Biochem. Biophys.* **561**, 3–12 (2014).

316.     Siggelkow, H. *et al.* Prolonged culture of HOS 58 human osteosarcoma cells with 1,25-(OH)2-D3, TGF-beta, and dexamethasone reveals physiological regulation of alkaline phosphatase, dissociated osteocalcin gene expression, and protein synthesis and lack of mineralization. *J. Cell. Biochem.* **85**, 279–294 (2002).

317.     Boyce, B. F. & Xing, L. Biology of RANK, RANKL, and osteoprotegerin. *Arthritis Research and Therapy* **9**, S1 (2007).

318.     Pérez-Sayáns, M., Somoza-Martín, J. M., Barros-Angueira, F., Rey, J. M. G. & García-García, A. RANK/RANKL/OPG role in distraction osteogenesis. *Oral Surgery, Oral Medicine, Oral Pathology,*

*Oral Radiology and Endodontology* **109**, 679–686 (2010).

319. Atkins, G. J. *et al.* RANKL Expression Is Related to the Differentiation State of Human Osteoblasts. *J. Bone Miner. Res.* **18**, 1088–1098 (2003).

320. Gori, F. *et al.* The expression of osteoprotegerin and RANK ligand and the support of osteoclast formation by stromal-osteoblast lineage cells is developmentally regulated. *Endocrinology* **141**, 4768–4776 (2000).

321. Zhu, M. *et al.* The effect of age on osteogenic, adipogenic and proliferative potential of female adipose-derived stem cells. *J. Tissue Eng. Regen. Med.* **3**, 290–301 (2009).

322. Hanna, H., Mir, L. M. & Andre, F. M. In vitro osteoblastic differentiation of mesenchymal stem cells generates cell layers with distinct properties. *Stem Cell Res. Ther.* **9**, 1–11 (2018).

323. Wei, D.-X., Dao, J.-W. & Chen, G.-Q. A Micro-Ark for Cells: Highly Open Porous Polyhydroxyalkanoate Microspheres as Injectable Scaffolds for Tissue Regeneration. *Adv. Mater.* **30**, 1802273 (2018).

324. Uskoković, V. The role of hydroxyl channel in defining selected physicochemical peculiarities exhibited by hydroxyapatite. *RSC Adv.* **5**, 36614–36633 (2015).

325. Von Euw, S. *et al.* Bone mineral: new insights into its chemical composition. *Sci. Rep.* **9**, 1–11 (2019).

326. Uskoković, V. & Uskoković, D. P. Nanosized hydroxyapatite and other calcium phosphates: Chemistry of formation and application as drug and gene delivery agents. *Journal of Biomedical Materials Research - Part B Applied Biomaterials* **96 B**, 152–191 (2011).

327. Jeong, J., Kim, J. H., Shim, J. H., Hwang, N. S. & Heo, C. Y. Bioactive calcium phosphate materials and applications in bone regeneration. *Biomater. Res.* **23**, 4 (2019).

328. Nygren, H., Bigdeli, N., Ilver, L. & Malmberg, P. Mg-corrosion, hydroxyapatite, and bone healing. *Biointerphases* **12**, 02C407 (2017).

329. Thomas, J. & Gemming, T. ELDISCA C# — a new version of the program for identifying electron diffraction patterns. in *EMC 2008 14th European Microscopy Congress 1–5 September 2008, Aachen, Germany* 231–232 (Springer Berlin Heidelberg, 2009). doi:10.1007/978-3-540-85156-1_116

330. Hasegawa, T. *et al.* Ultrastructural and biochemical aspects of matrix vesicle-mediated mineralization. *Jpn. Dent. Sci. Rev.* **53**, 34–45 (2017).

331. Kirsch, T., Wang, W. & Pfander, D. Functional Differences Between Growth Plate Apoptotic Bodies and Matrix Vesicles. *J. Bone Miner. Res.* **18**, 1872–1881 (2003).

332. Fujita, H. *et al.* Necrotic and apoptotic cells serve as nuclei for calcification on osteoblastic differentiation of human mesenchymal stem cells *in vitro*. *Cell Biochem. Funct.* **32**, 77–86 (2014).

333. Schiller, H. B. *et al.* β 1 - And α v -class integrins cooperate to regulate myosin II during rigidity sensing of fibronectin-based microenvironments. *Nat. Cell Biol.* **15**, 625–636 (2013).

334. Weiss, D. J. *et al.* The necrobiology of mesenchymal stromal cells affects therapeutic efficacy. *Frontiers in Immunology* **10**, 1228 (2019).

335. Nollet, M. *et al.* Autophagy in osteoblasts is involved in mineralization and bone homeostasis. *Autophagy* **10**, 1965–1977 (2014).

336. Dang, S. *et al.* Autophagy promotes apoptosis of mesenchymal stem cells under inflammatory microenvironment. *Stem Cell Res. Ther.* **6**, (2015).

337. Itälä, A. I., Ylänen, H. O., Ekholm, C., Karlsson, K. H. & Aro, H. T. Pore diameter of more than 100 μm is not requisite for bone ingrowth in rabbits. *J. Biomed. Mater. Res.* **58**, 679–683 (2001).

# 7 List of Figures and Tables

# 8 Abbreviations

| | |
|---|---|
| AFM | Atomic Force Microscope |
| ALD | Atomic Layer Deposition |
| BCA | Bicinchoninic Acid |
| BSA | Bovine Serum Albumin |
| CaP | Calcium Phosphate |
| DAPI | 4′,6-diamidino-2-phenylindole |
| DI | Deionized water |
| DM | Differentiation Medium |
| DMEM | Dulbecco's Modified Eagle's Medium |
| DMSO | Dimethyl sulfoxide |
| ECM | Extra-Cellular Matrix |
| EDX | Energy-Dispersive X-ray spectroscopy |
| ELISA | Enzyme-Linked Immunosorbent Assay |
| FA | Focal Adhesion |
| FCS | Fetal Calf Serum |
| FDA | Fluorescein Diacetate |
| FIB | Focused Ion Beam |
| GAG | Glycosaminoglycans |
| HA | Hydroxyapatite |
| hCol | human Collagen |
| MSC | Mesenchymal Bone Cell |
| MTS | 3-(4,5-dimethylthiazol-2-yl)-5-(3carboxymethoxyphenyl)-2-(4-sulfophenyl)-2H-tetrazolium |
| MV | Matrix Vesicle |
| OPG | Osteoprotegerin |
| OPN | Osteopontin |
| PBS | Phosphate-Buffered Saline |
| PCB | Printed Circuit Board |

| | |
|---|---|
| PEG | Polyethylene Glycol |
| PI | Propidium Iodide |
| PLD | Pulsed Laser Deposition |
| pNPP | p-Nitrophenylphosphate |
| RANK | Receptor Activator of Nuclear Factor κ B |
| RANKL | Receptor Activator of Nuclear Factor κ B Ligand |
| RGD | Arg-Gly-Asp |
| RMS | Root Mean Square |
| qPCR | quantitative real-time Polymerase Chain Reaction |
| SAED | Selected Area Electron Diffraction |
| SEM | Scanning Electron Microscope |
| SM | Standard Medium |
| SOA | $SiO/SiO_2/Al_2O_3$ |
| STEM | Scanning Transmission Electron Microscope |
| TCPS | Tissue Culture Polystyrene |
| TEM | Transmission Electron Microscopy |
| TN | Ti-45Nb (wt%) |
| TNAP | Tissue Nonspecific Alkaline Phosphatase |
| TNO | Ti-45Nb-oxide (wt%) |
| TS | Tubular microscaffold |
| XPS | X-Ray Photoelectron Spectroscopy |
| XRD | X-Ray Diffraction |

# 9 Acknowledgements

uncertainty, but helped me in many ways, encouraged me to keep on and was always there for me.

It was a demanding, but amazing time that we all shared together. I wish you all the best and hope to find such great support again in my upcoming endeavors.